ICQNM 2014

The Eighth International Conference on Quantum, Nano/Bio, and Micro Technologies

ISBN: 978-1-61208-380-3

November 16 - 20, 2014

Lisbon, Portugal

ICQNM 2014 Editors

Victor Ovchinnikov, Aalto University, Finland

Vladimir Privman, Clarkson University - Potsdam, USA

ICQNM 2014

Foreword

The Eighth International Conference on Quantum, Nano and Micro Technologies (ICQNM 2014), held between November 16-20, 2014 in Lisbon, Portugal, continued a series of events covering particularly promising theories and technologies. The conference covered fundamentals on designing, implementing, testing, validating and maintaining various kinds of materials, systems, techniques and mechanisms related to quantum-, nano- and micro-technologies.

Quantum technologies and nano technologies have a great potential to transform communications telecommunications infrastructure and communication protocols, and computers and networking devices. Nanotechnologies and micro-technologies already made their mark on smart materials, nano-medicine, nano-devices, molecular manufacturing, biotechnology, metrology, airspace.

The advancements in material science and computer science have allowed the building, launching and deploying of space exploration systems that continually do more and more as they become smaller and lighter. As an example, carbon nano-tubes have been created that are 250 times stronger than steel, 10 times lighter, and transparent. Similar advances are occurring in glass, plastics and concrete. Spacecraft are being launched, with hulls that are composed of carbon fibers, a light weight high strength material.

Electronic devices, medicine, environment, metrology, aerospace programs, clothes and materials, telecommunications, cryptography, semiconductors, manufacturing, and other domains are impacted by the progress on the areas mentioned above. Particularly, micro imaging, nano-medicine: (drug delivery; nano-particles i.e. viruses; proteins.), bio-nanostructures: (nano-tubes, nano-particles), microsystems, micro fluidics: (including nano-fluidics, modeling; fabrication and application), micro instrumentation / implantable microdevices (miniaturized bio-electronic systems, etc.) and micro sensors benefits from the progress on quantum, nano and micro technologies.

Developing nanoscale-manufactured robots presents fabrication and control challenges. The evolution of mechatronics system and robotic system requires advanced functions for control. Special methods and technologies have been developed to design, analyze, build, controls, and apply micro/nano-robotic systems for biotechnology, medical, information technology, materials, etc. A particular application of nano-robots would be in carrying out projects in hostile environments, utilizing local materials and local energy. Ultra-miniature robotic systems and nano-mechanical devices will be the biomolecular electro-mechanical hardware of future manufacturing and biomedical industry.

Nowadays, there are tremendous attempts to develop new bio-molecular machines, components that can be assembled in nano-devices. Bio-robotics entities are able to manipulate the nano-world components, convey information from the nano/nano to the nano/macro world and navigate at the nano-environment level. Additionally, they are able to self replicate, leading to the bio-robot factory. Protein-based nano-motors and nano-robots, as well as biomolecular components interfaces.

Quantum cryptography uses the uncertainty principle of quantum physics to provide a safe but public means for transmitting vital, secret information. A quantum public key distribution system depends on the uncertainty principle to ensure secrecy. Special protocols correlations and composability algorithms ensure similar functionality as in non-quantum systems. The security related tracks cover a series of events focusing on quantum security aspects. On the quantum protocol side, automated proofs of security and probabilistic model-checking methods have been suggested. Research teams focus on quantum key distribution and aspects related to key composability and correlations. Limitations are mainly related to physical devices and polarization control.

We take here the opportunity to warmly thank all the members of the ICQNM 2014 Technical Program Committee, as well as the numerous reviewers. The creation of such a high quality conference program would not have been possible without their involvement. We also kindly thank all the authors who dedicated much of their time and efforts to contribute to ICQNM 2014. We truly believe that, thanks to all these efforts, the final conference program consisted of top quality contributions.

Also, this event could not have been a reality without the support of many individuals, organizations, and sponsors. We are grateful to the members of the ICQNM 2014 organizing committee for their help in handling the logistics and for their work to make this professional meeting a success.

We hope that ICQNM 2014 was a successful international forum for the exchange of ideas and results between academia and industry and for the promotion of progress in quantum, nano and micro technologies.

We are convinced that the participants found the event useful and communications very open. We hope Lisbon provided a pleasant environment during the conference and everyone saved some time for exploring this beautiful city.

ICQNM 2014 Chairs:

ICQNM Advisory Chairs
Vladimir Privman, Clarkson University - Potsdam, USA
Christian Kollmitzer, AIT Austrian Institute of Technology GmbH, Austria
Wen-Ran Zhang, Georgia Southern University, USA
Victor Ovchinnikov, Aalto University, Finland

ICQNM 2014 Research/Industry Chairs
Marco Genovese, Italian Metrological Institute (INRIM) -Torino, Italy
Keiji Matsumoto, National Institute of Informatics, Japan

ICQNM 2014 Special Area Chairs
QSEC
Masahito Hayashi, Nagoya University, Japan
Fluidics
Alireza Azarbadegan, University College London (UCL), UK

Quantum algorithms and quantum complexity
Francois Le Gall, The University of Tokyo, Japan
Quatum control
Daoyi Dong, University of New South Wales, Australia

ICQNM 2014

Committee

ICQNM Advisory Chairs

Vladimir Privman, Clarkson University - Potsdam, USA
Christian Kollmitzer, AIT Austrian Institute of Technology GmbH, Austria
Wen-Ran Zhang, Georgia Southern University, USA
Victor Ovchinnikov, Aalto University, Finland

ICQNM 2014 Research/Industry Chairs

Marco Genovese, Italian Metrological Institute (INRIM) -Torino, Italy
Keiji Matsumoto, National Institute of Informatics, Japan

ICQNM 2014 Special Area Chairs

QSEC
Masahito Hayashi, Nagoya University, Japan

Fluidics
Alireza Azarbadegan, University College London (UCL), UK

Quantum algorithms and quantum complexity
Francois Le Gall, The University of Tokyo, Japan

Quatum control
Daoyi Dong, University of New South Wales, Australia

ICQNM 2014 Technical Program Committee

Andrew Adamatzky, University of the West of England - Bristol, U.K.
Gerardo Adesso, Quantum Theory Group/Università di Salerno, Italy
Irina Buyanova, Linkoping University, Sweden
Weimin M. Chen, Linköping University, Sweden
Taksu Cheon, Kochi University of Technology - Tosa Yamada, Japan
Sang H. Choi, NASA Langley Research Center, USA
Mihaela Corneanu, Banat's University of Agricultural Sciences and Veterinary Medicine, Romania
Sorin Cotofana, TU Delft, The Netherlands
Brahim Dennai, ENERGARID Laboratory, France
Sao-Ming Fei, Capital Normal University - Beijing, China
Akihiko Fujiwara, Japan Synchrotron Radiation Research Institute - Hyogo, Japan
Juan Carlos García-Escartín, Universidad de Valladolid, Spain
Yuval Gefen, The Weizmann Institute of Science, Israel
Marco Genovese, Italian Metrological Institute (INRIM) -Torino, Italy
Bonnie Gray, Simon Fraser University, Canada

Copyright Information

For your reference, this is the text governing the copyright release for material published by IARIA.

The copyright release is a transfer of publication rights, which allows IARIA and its partners to drive the dissemination of the published material. This allows IARIA to give articles increased visibility via distribution, inclusion in libraries, and arrangements for submission to indexes.

I, the undersigned, declare that the article is original, and that I represent the authors of this article in the copyright release matters. If this work has been done as work-for-hire, I have obtained all necessary clearances to execute a copyright release. I hereby irrevocably transfer exclusive copyright for this material to IARIA. I give IARIA permission or reproduce the work in any media format such as, but not limited to, print, digital, or electronic. I give IARIA permission to distribute the materials without restriction to any institutions or individuals. I give IARIA permission to submit the work for inclusion in article repositories as IARIA sees fit.

I, the undersigned, declare that to the best of my knowledge, the article is does not contain libelous or otherwise unlawful contents or invading the right of privacy or infringing on a proprietary right.

Following the copyright release, any circulated version of the article must bear the copyright notice and any header and footer information that IARIA applies to the published article.

IARIA grants royalty-free permission to the authors to disseminate the work, under the above provisions, for any academic, commercial, or industrial use. IARIA grants royalty-free permission to any individuals or institutions to make the article available electronically, online, or in print.

IARIA acknowledges that rights to any algorithm, process, procedure, apparatus, or articles of manufacture remain with the authors and their employers.

I, the undersigned, understand that IARIA will not be liable, in contract, tort (including, without limitation, negligence), pre-contract or other representations (other than fraudulent misrepresentations) or otherwise in connection with the publication of my work.

Exception to the above is made for work-for-hire performed while employed by the government. In that case, copyright to the material remains with the said government. The rightful owners (authors and government entity) grant unlimited and unrestricted permission to IARIA, IARIA's contractors, and IARIA's partners to further distribute the work.

Table of Contents

Self-Adaption of Quantum Key Distribution Devices to Changing Working Conditions

Sandra König
Safety & Security Department
Austrian Institute of Technology, Klagenfurt, Austria
Sandra.Koenig@ait.ac.at

Stefan Rass
Department of Applied Informatics, System Security Group
Universität Klagenfurt, Universitätsstrasse 65-67
9020 Klagenfurt, Austria
stefan.rass@uni-klu.ac.at

***Abstract*—Quantum key distribution (QKD) draws security from the ability to detect eavesdroppers upon the incident of "unnaturally high" quantum bit error rates (QBER) during the protocol. This presumes that a working QKD device implementation needs to be calibrated with its own individual and characteristic channel noise that is observed in any case, especially when there is no eavesdropper. This natural noise level influences the idle QBER, and is in turn dependent on the device's working conditions. This work describes a statistical approach to construct a model that can be used to continuously compute the normal QBER, based on current (and changing) working conditions. The model is thus meant as a tool to refine the theoretical QBER threshold specific to the given QKD protocol, based on empirical data obtained under the given environmental conditions. More importantly, it allows the QKD-device to self-recalibrate under changing working conditions.**

Keywords–copula; estimation; quantum network; quantum devices; statistics

I. INTRODUCTION

The unique feature of quantum key distribution (QKD) is its ability to detect passive eavesdropping. This remarkable ability rests on a fundamental result of quantum physics that rules out the possibility of creating a perfect copy of a single photon [1]. Consequently, passive eavesdropping attempts will unavoidably introduce errors on a quantum channel that would otherwise deliver quantum bits (qubits, photons) under some specific and characteristic channel noise and error frequency.

Recent experimental findings on the quantum key distribution network demonstrated as the result of the EU project SECOQC (summarized in [2]) raised the question of how much environmental influences affect the "natural" quantum bit (qubit) error rate (QBER) observed on a quantum line that is not under eavesdropping attacks. A measurement sample reported in [3] was used to gain first insights in the problem, but the deeper mechanisms of dependency between QBER and the device's working conditions have not been modeled comprehensively up to now.

The desire of having a model that explains how the QBER depends on environmental parameters like temperature, humidity, radiation, etc. is motivated by the problem of finding a good calibration of QKD devices, so that the channel performance is maximized. Unfortunately, with the QBER being known to depend on non-cryptographic parameters, it is difficult to give reasonable threshold figures that distinguish the natural error level from that induced by a passive eavesdropping. We spare the technical details on how a QBER threshold is determined for a given QKD protocol here (that procedure is specific for each known QKD protocol and implementation), and focus our attention on a statistical approach to obtain a model of interplay between the qubit error rate and various environmental parameters.

To this end, we utilize a general tool of probability theory, a *copula function*, to separate the parameter model (probability distribution of a single environment parameter) from the interdependency model (which is the copula function). In that regard, we use Section II to refresh the reader's memory on copula theory to the extent required here to get to the point where we can give effective methods to infer an expected qubit error rate upon known external influence parameters.

More precisely, our work addresses the following problem: *given the current working conditions of a QKD device, what would the natural qubit error rate be, whose transgression would indicate the presence of an eavesdropper?* The basic intention behind this research is aiding practical implementations of QKD-enhanced networks, where our models provide a statistically grounded help to react on changing environmental conditions. The remainder of this work is structured as follows: after theoretical groundwork in Section II, we move on by showing how to use empirical data (measurements) drawn from a given device to construct an interdependency model that explains how the QBER and other variables mutually depend on one another. Section IV then describes how to single out the QBER from this overall dependency structure towards computing the expected error rate from the remaining variables. The concluding Section V summarizes the procedure and provides final remarks.

Related Work

Surprisingly, there seem to be only few publications paying attention to statistical dependencies of cryptographic parameters and the working conditions of a real device, such as [3], [4]. While most experimental implementations of QKD, such as [2], [5]–[8] give quite a number of details on device parameters, optimizations of these are mostly out of focus. An interesting direction of research is towards becoming "device-independent" [9], [10], which to some extent may relieve issues of hacking detection facilities, yet leaves the problem of optimal device configuration nevertheless open. The idea of self-adaptation is not new and has already seen applications in the quantum world [11]–[13] including the concept of copulas, applications of the latter to the end of self-adaption remain a seemingly new field of research. Copulas have been successfully applied to various problems of explaining and exploiting dependencies among various risk factors (related to general system security [14], [15]), and the goal of this work is taking first steps in a study of their applicability in the yet unexplored area of self-configuring quantum devices.

 ISBN: 978-1-61208-380-3

II. Preliminaries and Notation

We denote random variables by uppercase Latin letters $(X, Z, \ldots)$, and let matrices be uppercase Greek or bold-printed Latin letters $(\Sigma, \mathbf{D}, \ldots)$. The symbol $X \sim F(x)$ denotes the fact that the random variable X has the distribution function F. For each such distribution, we let the corresponding lower-case letter denote its density function, i.e., f in the example case.

For self-containment of our presentation, we give a short overview of the most essential facts about copulas that we are going to use, as for a more detailed introduction we refer to [16].

Definition II.1. *A* copula *is a (n-dimensional) distribution function $C : [0,1]^n \to [0,1]$ with uniform marginal distributions.*

Especially, a copula satisfies the following properties:

Lemma II.1. 1) *For every $u_1, \ldots, u_n \in [0,1]$, $C(u_1, \ldots, u_n) = 0$ if at least one of the arguments is zero and*
2) *$C(u_1, \ldots, u_n) = u_i$ if $u_j = 1$ for all $j \neq i$.*

A family of copulas that leads to handy models in higher dimensions is known as the family of Archimedean copulas, of which many extensions exist.

Definition II.2. *An* Archimedean copula *is determined by the so called* generator function $\phi(x)$ *via*

$$C(u_1, \ldots, u_n) = \phi^{-1}(\phi(u_1) + \ldots + \phi(u_n)). \qquad (1)$$

The generator function $\phi : [0,1] \to [0,\infty]$ has to satisfy $\phi(1) = 0$ and $\phi(\infty) = 0$, furthermore, ϕ has to be n-monotone*, i.e., to be differentiable up to order $n-2$ with $(-1)^{n-2}\phi^{(n-2)}(t)$ being nondecreasing and convex and*

$$(-1)^i \phi^{(i)}(t) \geq 0 \text{ for } 0 \leq i \leq n-2$$

for all $t \in [0, \infty)$.

As one of the cornerstones in copula theory, *Sklårs theorem* connects these functions to the relationship between n univariate distribution functions and their joint (multivariate) distribution:

Proposition II.2. *Let the random variables $X_1, \ldots, X_n$ have distribution functions $F_1, \ldots, F_n$ respectively and let H be their joint distribution function. Then there exists a copula C such that*

$$H(x_1, \ldots, x_n) = C(F_1(x_1), \ldots, F_n(x_n))$$

for all $x_i, \ldots, x_n \in \mathbb{R}$.
If all the F_is are continuous, then the copula C is unique.

The usefulness of this result lies in the fact that the joint distribution function of $X_1, \ldots, X_n$ can be decomposed into n univariate functions $F_1, \ldots, F_n$ that describe the behaviour of the individual variables and another component (namely the function C) that describes the dependence structure, which allows to model them independently.

Turning things around it is also possible to extract the dependence structure from the marginal distributions F_i and the joint distribution H via

$$C(u_1, \ldots, u_n) = H(F_1^{-1}(u_1), \ldots, F_n^{-1}(u_n)) \qquad (2)$$

where $F_i^{-1}(u)$ denotes the pseudo-inverse of $F_i(x)$, which is given by $F_i^{-1}(u) = \sup\{x | F_i(x) \leq u\}$. A special case of this connection between Copula and random variables leads an alternative characterization of independence, which is usually written as $H(x_1, \ldots, x_n) = F_1(x_1) \cdot \ldots \cdot F_n(x_n)$.

Example II.3. *If the (unique) copula from (2) turns out to be the product copula $C(u_1, \ldots, u_n) = u_1 \cdot \ldots \cdot u_n$, then the random variables $X_1, \ldots, X_n$ are independent.*

III. A Copula Model of the QKD network

A. Summary of the Data

A summary of the results obtained from an implemented QKD network in Vienna [2] can be found in [4]. The following quantities were measured and are used here (abbreviation in brackets): qubit error rate in percentage terms (QBER), air temperature (TEMP), relative humidity (HUM), sunshine duration in seconds (DUR), global radiation in watt/m^2(RAD).

Since we are here focusing on the relationship between QBER and environmental quantities, we only use data that were measured on the same device to avoid getting biased results. The quantiles of our sample of size $n = 276$ are displayed in Table I.

TABLE I. Quantiles of measured quantities

	min	$q_{0.25}$	median	$q_{0.75}$	max
QBER	98.00	132.75	147.00	163.00	212.00
TEMP	117.00	134.75	148.00	163.00	184.00
HUM	71.00	80.00	84.00	91.00	93.00
DUR	0.00	0.00	0.00	0.00	600.00
RAD	0.00	0.00	0.00	146.00	539.00

Throughout the rest of the paper, let $\mathbf{D}$ denote the data matrix that comprises the entirety of samples as a table whose headings correspond to the row labels in Table I. Thus, the matrix $\mathbf{D}$ is of shape $(n \times 5)$ for our $n = 276$ samples, and has entries $(X_1, \ldots, X_5)$ modeling the measurements of (QBER, TEMP, HUM, DUR, RAD) as random variables.

B. Building up a Model

Mainly interested in the dependence structure, we do not make explicit assumptions about the distributions of each quantity but rather use their empirical distribution to transform them into pseudo-observations $U_1, \ldots, U_n$ that are uniform $(0,1)$-distributed. A basic first choice is to consider a multidimensional copula C that models the joint distribution H of all the quantities via $H(x_1, \ldots, x_n) = C(U_1, \ldots, U_n)$. Fitting a copula is usually done by maximizing the log-likelihood function

$$\ell(x_1, \ldots, x_n) = \log\left[c\left(u_1, \ldots, u_n\right)\right],$$

with c denoting the density of the copula C. In a general setting, this can easily become infeasible in our five-dimensional case, so we first choose a parametric family C_θ of copulas and then seek the parameter θ that maximizes the one-dimensional function

$$\ell(\theta) = \log\left[c_\theta\left(u_1, \ldots, u_n\right)\right].$$

 ISBN: 978-1-61208-380-3

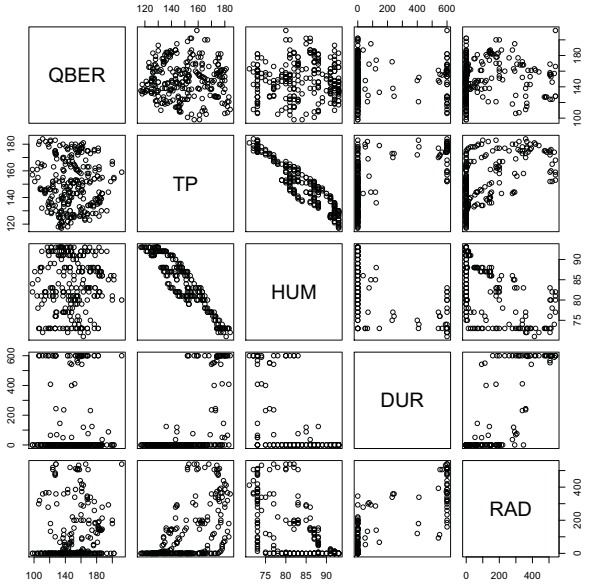

Figure 1. Pairwise correlations among variables

As for the parametric family, we first choose the *Gumbel copula*, which is generated by $\phi(t) = (-\ln(t))^\theta$, yielding

$$C(u_1, \ldots, u_n) = \exp\left\{-[(-\ln(u_1))^\theta + \ldots + (-\ln(u_n))^\theta]^{1/\theta}\right\}.$$

A p-value of zero clearly shows that this model is not describing the data properly.

The above model is simple to construct and to use but it also has its weaknesses: firstly it describes the behaviour of five random variables with just one number and secondly its components are all exchangeable. Taking a closer look at the pairwise correlations of the considered quantities (see Figure 1) shows that this exchangeability is not fulfilled in our case.

To take care of possibly different correlations among the occurring variables, we consider a more flexible model called *nested* copulas (sometimes also called hierarchical copulas) which is often used in finance, see for example [14]. The basic idea of a nested copula model is to use several copulas at different levels to describe the relation between the variables.

For clarity of such a hierarchically constructed probability distribution, we use a graphical tree-notation like shown in Figure 2 to "depict" the (otherwise complicated) distribution function. To formally specify the latter, we introduce some notational conventions: at each level $\ell \in 1, \ldots, L$ (counting bottom-up in the hierarchy tree) we have n_ℓ copulas, where $C_{\ell,j}$, $j \in 1, \ldots, n_\ell$, is the $j-$th copula at level ℓ. Further, every copula $C_{\ell,j}$ has dimension $d_{\ell,j}$ that gives the number of arguments u_i that directly or indirectly enter this copula.

Two special cases are shown in Figure 2 for the four-dimensional case: the fully nested copula which adds one dimension at each step (left side) and a partially nested copula where the number of copula decreases at each level (right side). Formally, a fully nested copula is defined by

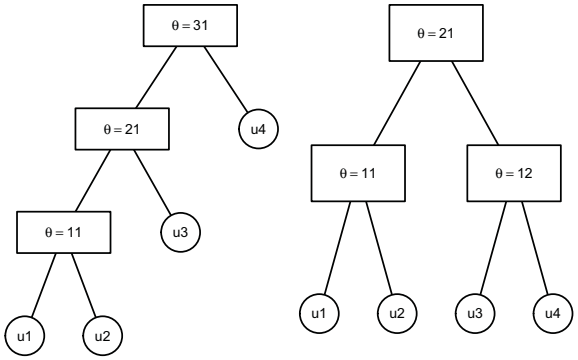

Figure 2. Fully nested vs. partially nested copula

$$\begin{aligned} &C(u_1, \ldots, u_n) = \\ &\phi_{n-1}^{-1}[\phi_{n-1}(\ldots[\phi_2(\phi_1^{-1}[\phi_1(u_1) + \phi_1(u_2)] + \phi_2(u_3)] \\ &+ \ldots + \phi_{n-2}(u_{n-1})) + \phi_{n-1}(u_n))], \end{aligned} \quad (3)$$

where the occurring generator functions $\phi_1, \ldots, \phi_{n-1}$ may come from different families of Archimedean copulas.

All in all, the dependence structure is determined by $n-1$ parameters (instead of just one as in the model above) and there are $\frac{n(n-1)}{2}$ different bivariate margins.

The partially nested copula may be defined similarly, for reasons of clarity and comprehensibility we here give the expression for $n = 4$, corresponding to the case shown in the right side of Figure 2:

$$\begin{aligned} C(u_1, u_2, u_3, u_4) =& \phi_{21}^{-1}[\phi_{21}(\phi_{11}^{-1}[\phi_{11}(u_1) + \phi_{11}(u_2)] \\ &+ \phi_{21}(\phi_{12}^{-1}[\phi_{12}(u_3) + \phi_{12}(u_4)])], \end{aligned} \quad (4)$$

where the generator ϕ_{ij} is from the jth copula on the ith level, usually denoted by C_{ij}.

Finding a suitable nested copula model may quickly become laborious since one might have to check all possible subsets of variables and compare the goodness of fit of the corresponding estimated copula. Handling this problem in `R`, one may use the package `HAC`, introduced in [17]. In our case, we find that a suitable model consists of four two-dimensional Gumbel copulas, which are defined as follows:

Definition III.1. *A* Gumbel copula *is an Archimedean copula that is generated by*

$$\phi(t) = (-\ln(t))^\theta$$

for $\theta \geq 1$.
In the two-dimensional case, the copula is explicitly given by

$$C(u, v) = \exp\left[-\left((-\ln(u))^\theta + (-\ln(v))^\theta\right)^{\frac{1}{\theta}}\right] \quad (5)$$

for $u, v \in [0, 1]$.

The dependence structure between the considered quantities is shown in Figure 3.

It is known that in a nested copula model with a Gumbel generator the parameters have to decrease with the level (see [14] for fully nested copulas and [18] for the general case).

 ISBN: 978-1-61208-380-3

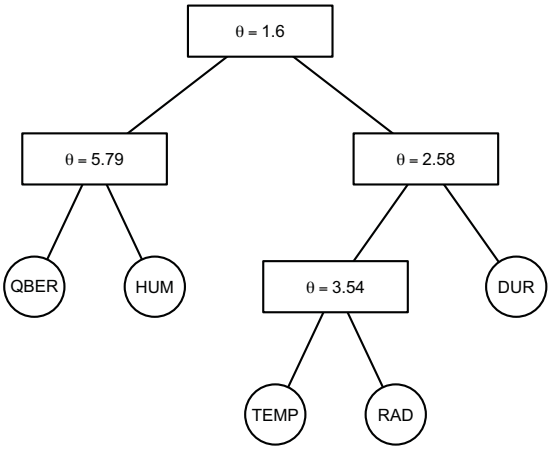

Figure 3. Dependence structure for HAC model

Since in our case the parameters on the upper levels are rather close, we consider a modification of this model by allowing to aggregate Copulas whose parameters do not differ too much. A justification for this approach is the close relation between the parameter θ of the generator and Kendall's tau τ, which is connected to copulas via

$$\tau = 4 \int_{[0,1]^2} C(u,v) dC(u,v) - 1. \quad (6)$$

For Archimedean copulas with generator function $\phi(t)$, it was shown in [16] that (6) simplifies to

$$\tau = 1 + 4 \int_0^1 \frac{\phi(t)}{\phi'(t)} dt, \quad (7)$$

which for the Gumbel copula leads to

$$\begin{aligned} \tau &= 1 - 4 \int_0^1 \frac{(-\log(t))^\theta \cdot t}{\theta(-\log(t))^{\theta-1}} dt \\ &= 1 - \frac{1}{\theta}. \end{aligned}$$

Hence if the parameters of two subsequent copulas are close, so is their dependence when characterized through Kendall's τ and it might be beneficial to model the affected variables with only one copula.

In order to get an impression on how suitable each of the above models is, we adapted the bootstrapping goodness of fit test [19] that was used in the case of a one-parametric copula to the estimation of nested copulas.

In our first 200 trial tests, each of which with a sample size of $N = 1000$ and a confidence level of 0.95, we never got a positive p-value if the tolerance is set to zero. When copulas are allowed to be aggregated, a p-value of 0.014 was found once, which still leads to rejection of the null hypothesis that the data at hand are drawn from a distribution given through this copula. This indicates that some preconditioning of the data matrix might be necessary to get a good fit. One solution for such a preprocessing is described in the next Section.

C. Preconditioning Towards Better Fits

As indicated by our quantum network data, it may occasionally be the case that none of the tried copula-models models the data satisfactorily. More precisely, existing software packages for copula fitting (such as `HAC` in `R`) assume *positive correlations* between all variables of interest. Unfortunately, our experimental QKD prototype supplied data exhibiting *negative* correlations amongst some of the observed variables.

In order to fix this, we can apply a linear transformation $\mathbf{M}$ to the data matrix $\mathbf{D}$ in order to make all pairwise correlations in the transformed data matrix $\mathbf{M} \cdot \mathbf{D}$ strictly positive. To this end, consider the Cholesky-decomposition of the covariance matrix Σ of the data $\mathbf{D}$, given as $\Sigma = \mathbf{L}^T \cdot \mathbf{L} = \mathbf{L}^T \cdot \mathbf{I} \cdot \mathbf{L}$. By the linearity properties of covariance, it is easy to check that the covariance matrix of $\mathbf{D} \cdot \mathbf{L}^{-1}$ is the identity matrix, having zero-correlations among all pairwise distinct variables. It is then a simple matter of multiplication with another invertible matrix (with low condition number to avoid numerical round-off-errors in the inverse transform) with all strictly positive entries to artificially introduce positive correlations, as required in the copula fitting process. Given such a matrix $\mathbf{A}$, the final linear transformation takes the form $\mathbf{D}' := \mathbf{D} \cdot (\mathbf{L}^{-1} \cdot \mathbf{A})$, thus our pre-conditioning transformation matrix is $\mathbf{M} := \mathbf{L}^{-1} \cdot \mathbf{A}$, where $\mathbf{L}$ comes out of the Cholesky decomposition of the original covariance matrix Σ, and $\mathbf{A}$ can be chosen freely, subject to only positive entries and good condition number (for numerically stable invertibility).

In our experiments, we used a bootstrap fitting with tolerance $\varepsilon = 0.4$. We constructed $\mathbf{A}$ as a 5×5-matrix having Gamma-distributed entries (with shape-parameter 5 and scale-parameter $1/2$). In 5 out of 200 trials, the p-value after pre-conditioning with $\mathbf{M} = \mathbf{L}^{-1}\mathbf{A}$ was larger than 0.05. The best fit giving $p = 0.613$ was obtained under the transformation coefficients (rounded to three decimals after the comma)

$$\mathbf{M} = \begin{pmatrix} 0.122 & 4.444 & 0.378 & 1.634 & 4.384 \\ 0.650 & 0.870 & 1.321 & 0.941 & 2.293 \\ 0.606 & 3.326 & 0.763 & 2.172 & 2.102 \\ 2.534 & 0.415 & 2.055 & 1.969 & 1.659 \\ 2.668 & 2.031 & 3.590 & 2.241 & 1.015 \end{pmatrix},$$

whose condition number is $\|\mathbf{M}\|_2 \cdot \|\mathbf{M}^{-1}\|_2 \approx 24.4945$, and determinant given as $\det(\mathbf{M}) \approx 29$, thus indicating good numerical stability for the inverse transformation.

In a second run of 200 experiments, we lowered the tolerance $\varepsilon = 0$, and did the preconditioning as before. This time, we got 20 out of 200 trials with a positive p-value, although only in three cases, our fit was accepted at $p > 0.05$. The best fit was obtained at $p = 0.536$, showing that the preconditioning works equally well with more complex hierarchical structures due to lower tolerance levels.

This transformation is applied *before* the copula fit, and must be carried through the derivation of predictive densities when obtaining a fit. We omit the simple and obvious changes to the upcoming formulas for simplicity, bearing in mind that actually a linearly transformed version of the data is under investigation, calling for the linear transformation to be inverted for predictions.

As an open issue, however, it remains interesting to find better ways than simple try-and-error to find a preconditioning matrix $\mathbf{A}$ that gives better fits than the plain data would do. Moreover, we believe that this trick may be of independent interest and use in other applications of copula theory, not limited to statistical descriptions of quantum key distribution devices.

 ISBN: 978-1-61208-380-3

IV. PREDICTION OF QBER RATES

Based on a model that describes the relationship between QBER and the environmental quantities, we look for a prediction of the QBER when all the other quantities are known. Having an idea of what values are to be expected, one might suspect an adversary to be present if these values are clearly exceeded. An essential ingredient to find a prediction is the conditional density, as it shows which values are likely in a given situation, that is, we seek the density of QBER conditional on all the other environmental parameters, i.e., the function

$$f(\text{QBER}|\text{TEMP}, \text{HUM}, \text{DUR}, \text{RAD}).$$

Section IV-A describes the general technique to compute the sought density, taking QBER as the n-th variable x_n in the upcoming descriptions. We stress that, however, the method is equivalently applicable to predict any other variable than QBER, too.

A. Computing Conditional Densities via Copulas

In the case where all the marginals and the copula are continuous, it holds for the transformed variables $u_i = F_i^{-1}(x_i)$ by the independence of copula and margins that

$$f(x_1, \ldots, x_n) = f_1(x_1) \cdot \ldots \cdot f_n(x_n) \cdot c_n(u_1, \ldots, u_n),$$

where $c_n(u_1, \ldots, u_n)$ denotes the density of the n-dimensional copula $C_n(u_1, \ldots, u_n)$ and f_i denotes the density of the marginal distribution F_i.

Example IV.1. *In the case of independent random variables, the above formula yields $c_n(u_1, \ldots, u_n) = 1$, which is the derivative of the independence copula $C_n(u_1, \ldots, u_n) = u_1 \cdots u_n$ from Example II.3.*

With this decomposition, the conditional density comes to

$$f(x_n|x_1, \ldots, x_{n-1}) = f_n(x_n) \frac{c_n(u_1, \ldots, u_n)}{c_{n-1}(u_1, \ldots, u_{n-1})} \quad (8)$$

for $u_i = F_i(x_i)$. Using (8) to compute the conditional density requires the lower-dimensional copula density $c_{n-1}(u_1, \ldots, u_{n-1})$, excluding the variable u_n (corresponding to the variable x_n of interest). So, computing the conditional density (8) from our full n-dimensional copula model proceeds as follows: let the variable x_i range within $[\underline{x}_i, \overline{x}_i]$, then the $(n-1)$-dimensional marginal density is

$$\begin{aligned} f(x_1, \ldots, x_{n-1}) &= \int_{\underline{x}_n}^{\overline{x}_n} f(x_1, \ldots, x_n) dx_n \\ &= \int_{\underline{x}_n}^{\overline{x}_n} \prod_{j=1}^{n} f_j(x_j) c_n(F_1(x_1), \ldots, F_n(x_n)) dx_n \\ &= [\Delta(\overline{x}_n) - \Delta(\underline{x}_n)] \cdot \prod_{j=1}^{n-1} f_j(x_j) \end{aligned}$$

with

$$\Delta(x) := \frac{\partial^{n-1}}{\partial x_1 \cdots \partial x_{n-1}} C_n(F_1(x_1), \ldots, F_{n-1}(x_{n-1}), F_n(x))$$

From this, the sought conditional distribution is immediately found as

$$f(x_n|x_1, \ldots, x_{n-1}) = f_n(x_n) \frac{c_n(F_1(x_1), \ldots, F_n(x_n))}{\Delta(\overline{x}_n) - \Delta(\underline{x}_n)} \quad (9)$$

Note that the density f_n of the variable of interest can be estimated both parametrical or non-parametrical (e.g., via kernel estimators) while in practice the distribution functions are estimated empirically to avoid additional assumptions.

In a general setting, we first compute the copula density (if the copula at hand is differentiable), whose tedious technicalities may conveniently be handled by a computer algebra system like MATHEMATICA or MAPLE. Again, this procedure simplifies within a smaller family of copulas.

For a n-dimensional Archimedean copula, the density turns out to be

$$c(u_1, \ldots, u_n) = (\phi^{-1})^{(n)}(\phi(u_1) + \ldots + \phi(u_n)) \prod_{i=1}^{n} \phi'(u_i)$$

where $(\phi^{-1})^{(n)}(t)$ denotes the n-th derivative of the inverse function $\phi^{-1}(t)$. This can be computed for Gumbel, Frank and Ali-Mikhael-Haq copulas, as for example done in [20], but becomes infeasible for the Gaussian copula considered at the beginning.

In the case of a nested copula, there is no simple closed expression available. One has to compute the derivative of the top level copula that describes the behaviour of all variables together which invokes the chain rule. While this may get complex in the general case, it is still practicable in our case.

In models that involve more levels of sub-copulas than the one considered here, one might use the derivative of $C_{L,1}(C_{L-1,1}, \ldots, C_{L-1,n_{L-1}})$ that evaluates to

$$\begin{aligned} \frac{\partial^d C_{L,1}}{\partial u_1 \cdots \partial u_d} = \sum_{i=0}^{d-n_{L-1}} \sum_{k_1, \ldots, k_{n_{L-1}}} \Bigg\{ & \frac{\partial^{d-i} C_{L,1}}{\partial C_{L-1,1}^{k_1} \cdots \partial C_{L-1,n_{L-1}}^{k_{n_{L-1}}}} \\ & \times \prod_{r=1}^{n_{L-1}} \sum_{v_1, \ldots, v_{k_r}} \frac{\partial^{|v_1|} C_{L-1,r}}{\partial v_1} \cdots \frac{\partial^{|v_{k_r}|} C_{L-1,r}}{\partial v_{k_r}} \Bigg\} \end{aligned}$$

where the outer sum is taken over all integers $k_1, \ldots, k_{n_{L-1}}$ that sum up to $d - i$ and satisfy $k_j \leq d_{L-1,j}$ while the inner sum is over partitions $v_1, \ldots, v_{k_r}$ of those u_i showing up in the r-th copula at level $L-1$. For more details about this specific case, see [18].

B. Self-Adaptation to Environmental Conditions

For a general description, we relabel the variables and let X_n be the device or performance parameter that we wish to predict based on the known environmental conditions $x_1, \ldots, x_{n-1}$. Section IV-C illustrates this for $X_n = \text{QBER}$ and $(X_1, X_2, X_3, X_4) = (\text{DUR}, \text{RAD}, \text{TEMP}, \text{HUM})$.

A prediction of X_n, e.g., the QBER rate given the current environmental conditions, is then given by the conditional expectation or, alternatively, by any value x_n that maximizes expression (9) for $f(x_n|x_1, \ldots, x_{n-1})$ for the given values $x_1, \ldots, x_{n-1}$. This maximization can be done using standard numerical techniques, whose details are outside our scope here.

Since the indication of an adversary's presence hinges on known performance characteristics, most importantly the QBER rate, it is easy to adapt the respective thresholds to the expected values under the current environmental conditions. Adapting to different conditions then amounts to doing the optimization again under the new configuration.

 ISBN: 978-1-61208-380-3

C. A Worked Example

The density $c(u_1, \ldots, u_5)$ of the top level copula $C_{L,1}$ can be calculated by applying the chin rule. To avoid errors in potentially messy calculations like the following, a computer algebra system may become handy.

The copula C describing our network was found to be

$$\exp\left\{-\left[\begin{array}{l}\left((-\ln u_1)^{\theta_2}+(-\ln u_2)^{\theta_2}\right)^{\frac{\theta_1}{\theta_2}}+ \\ \left[\begin{array}{l}\left((-\ln u_3)^{\theta_4}+(-\ln u_4)^{\theta_4}\right)^{\frac{\theta_3}{\theta_4}}+ \\ (-\ln u_5)^{\theta_3}\end{array}\right]^{\frac{\theta_1}{\theta_3}}\end{array}\right]^{1/\theta_1}\right\} \tag{10}$$

Generally, it holds

$$\frac{\partial^5 C_{3,1}}{\partial u_1 \cdots \partial u_5} = \frac{\partial^5 C_{3,1}}{\partial^2 C_{2,1} \partial^3 C_{2,2}} \cdot \frac{\partial^2 C_{2,1}}{\partial u_1 \partial u_2} \cdot \frac{\partial^3 C_{2,2}}{\partial^2 C_{1,1} \partial u_5} \cdot \frac{\partial^2 C_{1,1}}{\partial u_3 \partial u_4},$$

where the two most inner derivatives compute as

$$\begin{aligned}\frac{\partial^2 C}{\partial u_1 \partial u_2} &= \frac{1}{u_1 \cdot u_2}(\log(u_1)\cdot\log(u_2))^{\theta-1} \\ &\cdot \exp\left[-\left((-\log(u_1))^{\theta}+(-\log(u_2))^{\theta}\right)^{\frac{1}{\theta}}\right] \\ &\cdot \left((-\log(u_1))^{\theta}+(-\log(u_2))^{\theta}\right)^{\frac{1}{\theta}-2} \\ &\cdot \left(\left((-\log(u_1))^{\theta}+(-\log(u_2))^{\theta}\right)^{\frac{1}{\theta}}+\theta-1\right)\end{aligned} \tag{11}$$

for any two-dimensional Gumbel copula C. Alternatively to this straightforward calculation, the two-dimensional density (11) can be computed directly from the generator function using the chain rule

$$\begin{aligned}c(u_1,u_2) &= \frac{\partial^2}{\partial u_1 \partial u_2}\phi^{-1}(\phi(u_1)+\phi(u_2)) \\ &= -\frac{\phi''(C(u_1,u_2))\phi'(u_1)\phi'(u_2)}{[\phi'(C(u_1,u_2))]^3}\end{aligned} \tag{12}$$

if both derivatives exist (see also [16]).

To find the expression for $\Delta(x)$ we analogously compute

$$\frac{\partial^4 C_{3,1}}{\partial^1 C_{2,1} \partial^3 C_{2,2}} \cdot \frac{\partial^1 C_{2,1}}{\partial u_2} \cdot \frac{\partial^3 C_{2,2}}{\partial^2 C_{1,1} \partial u_5} \cdot \frac{\partial^2 C_{1,1}}{\partial u_3 \partial u_4} \tag{13}$$

with the third order derivative of a Gumbel copula

$$\begin{aligned}\frac{\partial^3 C}{\partial u_1 \partial u_2 \partial u_3} &= \frac{(-\log(u_1)\cdot\log(u_2)\cdot\log(u_3))^{\theta-1}}{u_1 \cdot u_2 \cdot u_3} \cdot \exp\left[-z^{\frac{1}{\theta}}\right] \\ &\cdot \left(z^{3/\theta-3}+3(\theta-1)\cdot z^{2/\theta-3}+(\theta-1)(2\theta-1)z^{1/\theta-3}\right)\end{aligned} \tag{14}$$

where $z = (-\log(u_1))^{\theta}+(-\log(u_2))^{\theta}+(-\log(u_3))^{\theta}$. Again, this density can be computed from the generator function directly if all necessary derivatives exist, yielding

$$\begin{aligned}&\frac{\partial^3}{\partial u_1 \partial u_2 \partial u_3}\phi^{-1}\left(\phi(u_1)+\phi(u_2)+\phi(u_3)\right) \\ &= \phi'(u_1)\phi'(u_2)\phi'(u_3)\frac{3[\phi''(C)]^2-\phi'''(C)\cdot\phi'(C)}{[\phi'(C)]^5}\end{aligned} \tag{15}$$

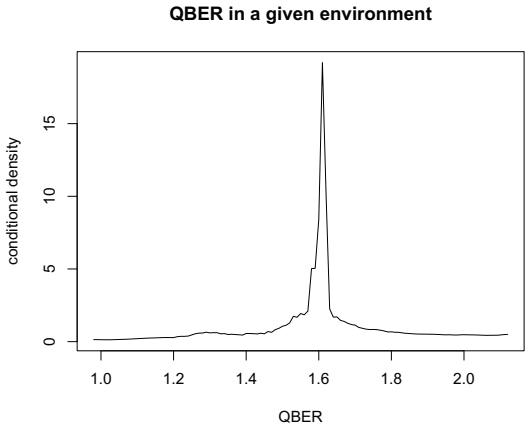

Figure 4. Density of QBER in a known environment

with the abbreviation $\phi(C) = \phi(C(u_1, u_2, u_3))$.

For the quantum network considered here, the conditional density of the QBER displayed in Figure 4 displays a unique maximum of the conditional density around QBER $= 1.61\%$, given typical environmental conditions that represent the current situation: sunshine duration DUR $= 0$s, global radiation RAD $= 0$W/m^2, relative humidity HUM $= 88\%$, and air temperature TEMP $= 14.4°$C. This means that QBER-values lower than 1.14% or higher then 2.07% are unlikely (i.e., these regions have a probability mass of 5% together) and probably arising from the presence of an eavesdropper.
Our analysis has been performed for typical values of the environmental variables, i.e., we set the variable DUR to zero as the sun did typically not shine during the measurement process. Variation of these values does not fundamentally affect out findings as the shape ot the conditional density does not change signifficantly.

V. Conclusion

Now, we come back to the initial problem that motivated this entire study. Recall that in a QKD setting, an unnaturally high qubit error rate indicates the presence of an adversary. Conversely, we need an idea about the "natural" rate of qubit errors. Given the conditional density (8) and according to the previous remarks, we can thus obtain a threshold for the qubit error rate that is tailored to the implementation, environment and device, and which can be adapted to changing environmental conditions. The steps are the following:

1) We run the device in a setting where there is no eavesdropper on the line to draw a series of measurements under clean conditions. In particular, we elicit all environmental variables of interest, especially the qubit error rate.
2) We fit a copula model to the so-obtained data $\mathbf{D}$, possibly doing a pre-conditioning (as described in Section III-C) for a statistically and numerically good fit. The fitting can be done using standard statistical software like `R`, using copula-specific libraries like `HAC` [17]. The derivation of the conditional distribution is easy by virtue of computer algebra systems like MATHEMATICA.

3) Having the copula-model, we obtain the conditional distribution (9) of the QBER under all environmental influences. Its maximization gives the currently valid threshold under the present environmental conditions. Speaking differently, this process tells us which values of the QBER are *not* likely enough to occur for a given value of the keyrate.

The respective details of each step have been described in previous Sections, giving examples along the way to illustrate the particular tasks. Nevertheless, the above process remains of generic nature and calls for appropriate instantiation (e.g., different environmental influences such as noisy source and detectors or turbulence structure of the air could be considered).

Once the probability density of the QBER conditional on current working conditions is obtained, it is a simple matter to equip a QKD device with sensory to keep the expected natural QBER rate continuously updated. We stress that this updating is unaffected by the presence of an attacker, unless the intruder manages to steer the environmental conditions in a way s/he likes. Assuming the absence of such an ability, the copula dependency model and its implied predictive distributions are an effective mean to let the devices re-calibrate themselves under the changing working conditions. Next steps in this research direction comprise practical experiments under variable lab conditions to test the quality of QBER adaption in terms of a performance gain over statically configured devices. As an important side-effect, this would also reveal possibilities to attack a QKD line by changing environmental factors. Such an attack has seemingly not been considered in the literature so far.

REFERENCES

[1] W. K. Wootters and W. H. Zurek, "A single quantum cannot be cloned," Nature, vol. 299, no. 802, 1982, pp. 802–803.

[2] Peev et al., "The SECOQC quantum key distribution network in Vienna," New Journal of Physics, vol. 11, no. 7, 2009, p. 075001.

[3] K. Lessiak, C. Kollmitzer, S. Schauer, J. Pilz, and S. Rass, "Statistical analysis of QKD networks in real-life environments," in Proceedings of the Third International Conference on Quantum, Nano and Micro Technologies. IEEE Computer Society, February 2009, pp. 109–114.

[4] K. Lessiak, "Application of generalized linear (mixed) models and nonparametric regression models for the analysis of QKD networks," Master's thesis, Universität Klagenfurt, 2010.

[5] T. Schmitt-Manderbach, "Long distance free-space quantum key distribution," Ph.D. dissertation, Ludwig–Maximilians–University Munich, Faculty of Physics, 2007.

[6] H. Xu, L. Ma, A. Mink, B. Hershman, and X. Tang, "1310-nm quantum key distribution system with up-conversion pump wavelength at 1550 nm," Optics Express, vol. 15, Jun. 2007, pp. 7247–7260.

[7] M. Li et al., "Measurement-device-independent quantum key distribution with modified coherent state," Opt. Lett., vol. 39, no. 4, Feb 2014, pp. 880–883.

[8] P. Jouguet, S. Kunz-Jacques, A. Leverrier, P. Grangier, and E. Diamanti, "Experimental demonstration of long-distance continuous-variable quantum key distribution," Nature Photonics, no. 5, 2013, pp. 378–381. [Online]. Available: http://www.nature.com/nphoton/journal/v7/n5/full/nphoton.2013.63.html [retrieved: September, 2014]

[9] A. Acín, N. Brunner, N. Gisin, S. Massar, S. Pironio, and V. Scarani, "Device-independent security of quantum cryptography against collective attacks," Physical Review Letters, vol. PRL 98, 230501, no. 1–4, 2007.

[10] Y. Liu et al., "Experimental measurement-device-independent quantum key distribution," Phys. Rev. Lett., vol. 111, no. 13, 2013, p. 130502. [Online]. Available: http://www.biomedsearch.com/nih/Experimental-Measurement-Device-Independent-Quantum/24116758.html [retrieved: September 2014]

[11] C. Ruican, M. Udrescu, L. Prodan, and M. Vladutiu, "Adaptive vs. self-adaptive parameters for evolving quantum circuits," in Evolvable Systems: From Biology to Hardware, ser. Lecture Notes in Computer Science, G. Tempesti, A. Tyrrell, and J. Miller, Eds. Springer Berlin Heidelberg, 2010, vol. 6274, pp. 348–359.

[12] C.-J. Lin, C.-H. Chen, and C.-Y. Lee, "A self-adaptive quantum radial basis function network for classification applications," in Proc. of International Joint Conference on Neural Networks, Vol. 4. IEEE, July 2004, pp. 3263–3268.

[13] A. M. Al-Adilee and O. Nánásiová, "Copula and s-map on a quantum logic." Inf. Sci., vol. 179, no. 24, 2009, pp. 4199–4207.

[14] P. Embrechts, F. Lindskog, and A. McNeil, Modelling Dependence with Copulas and Applications to Risk Management, Handbook of Heavy Tailed Distributions in Finance, Elsevier, 2001.

[15] D. Kelly, "Using copulas to model dependence in simulation risk assessment," in Proc. of 2007 ASME International Mechanical Engineering Congress and Exposition. American Society of Mechanical Engineers, 2007, pp. 81–89.

[16] R. Nelsen, An Introuction to Copulas. Springer, 2006.

[17] O. Okhrin and A. Ristig, "Hierarchical archimedean copulae: The HAC package," Journal of Statistical Software, vol. 58, no. 4, 2014, pp. 1–20. [Online]. Available: http://sfb649.wiwi.hu-berlin.de/papers/pdf/SFB649DP2012-036.pdf [retrieved: September, 2014]

[18] C. Savu and M. Trede, "Hierarchies of Archimedean copulas," Quantitative Finance, vol. 10, no. 3, February 2010, pp. 295–304.

[19] C. Genest and B. Rémillard, "Validity of the parametric bootstrap for goodness-of-fit testing in semiparametric models," Annales de l'institut Henri Poincaré (B) Probabilités et Statistiques, vol. 44, no. 6, 2008, pp. 1096–1127. [Online]. Available: http://eudml.org/doc/78005 [retrieved: September, 2014]

[20] C. Savu and M. Trede, "Goodness-of-fit tests parametric families of Archimedean copulas," Quantitative Finance, vol. 8, no. 2, March 2008, pp. 109–116.

 ISBN: 978-1-61208-380-3

Optimal Choice of Basis Transformations for Entanglement Swapping Based QKD Protocols

Stefan Schauer and Martin Suda

Safety and Security Department
AIT Austrian Institute of Technology GmbH
Vienna, Austria
Email: stefan.schauer@ait.ac.at, martin.suda.fl@ait.ac.at

***Abstract*—In this article, we discuss the optimality of basis transformations as a security measure for quantum key distribution protocols based on entanglement swapping. To estimate the security, we focus on the information an adversary obtains on the raw key bits from a generic version of a collective attack strategy. In the scenario described in this article, the application of general basis transformations serving as a counter measure by one or both legitimate parties is analyzed. In this context, we show that the angles, which describe these basis transformations, can be optimized compared to the application of a Hadamard operation, which is the standard basis transformation recurrently found in literature. As a main result, we show that the adversary's information can be reduced to an amount of $I_{AE} \simeq 0.20752$ when using a single basis transformation and to an amount of $I_{AE} \simeq 0.0548$ when combining two different basis transformations. This is less than half the information compared to other protocols using a Hadamard operation and thus represents an advantage regarding the security of entanglement swapping based protocols.**

Keywords–quantum key distribution; optimal basis transformations; security analysis; entanglement swapping

I. INTRODUCTION

One of the major applications of quantum mechanics is quantum key distribution (QKD). In the last three decades, QKD protocols have been studied at length in theory and in practical implementations [1]–[8]. Most of these protocols focus on prepare and measure schemes, where single qubits are in transit between the communication parties Alice and Bob. The security of these protocols has been discussed in depth and security proofs have been given for example in [9]–[11]. In addition to these prepare and measure protocols, several protocols based on the phenomenon of entanglement swapping have been introduced [12]–[17]. Entanglement swapping has been introduced by Bennett et al. [18], Zukowski et al. [19] as well as Yurke and Stolen [20], respectively. It provides the unique possibility to generate entanglement from particles that never interacted in the past. In the aforementioned protocols, entanglement swapping is used to obtain correlated measurement results between the legitimate communication parties, Alice and Bob. In other words, each party performs a Bell state measurement and due to entanglement swapping their results are correlated and further on used to establish a secret key.

A basic technique to secure a QKD protocol is to use a basis transformation, usually a Hadamard operation, to make it easier to detect an adversary. This is implemented, for example, in the prepare and measure schemes described in [1] and [3] but also in QKD schemes based on entanglement swapping (e.g., [13] [16] [21]). In this article, we analyze the application of a general basis transformation T_x, defined by the angles θ and ϕ (cf. (2)), to secure entanglement swapping based QKD protocols (cf. Figure 1). In the course of that, we are going to identify which values for θ and ϕ are optimal such that an adversary has only a minimum amount of information on the secret raw key.

Although basis transformations have been used as means of improving the security of QKD protocols based on entanglement swapping, this security measure has just been discussed on the surface so far. It has only been shown that these protocols are secure against intercept-resend attacks and basic collective attacks (cf. for example [12] [13] [16]). Therefore, we will analyze the *simulation attack*, a general version of a collective attack, which is based on the following idea [22]: the adversary Eve tries to find a multi-qubit state, which preserves the correlation between the two legitimate parties. Further, she introduces additional qubits to distinguish between Alice's and Bob's respective measurement results (cf. also Figure 2). If she is able to find such a state, Eve stays undetected during her intervention and is able to obtain a certain amount of information about the key. Such a multi-qubit state would be

$$|\delta\rangle = \frac{1}{2}\Big(|\Phi^+\rangle|\Phi^+\rangle|\varphi_1\rangle + |\Phi^-\rangle|\Phi^-\rangle|\varphi_2\rangle \\ |\Psi^+\rangle|\Psi^+\rangle|\varphi_3\rangle + |\Psi^-\rangle|\Psi^-\rangle|\varphi_4\rangle\Big)_{PRQSTU} \tag{1}$$

where the $|\varphi_i\rangle$ are the additional systems introduced by Eve. To perfectly distinguish between Alice's and Bob's results, these state $|\varphi_i\rangle$ have to be pairwise orthogonal. Thus, she is able to eavesdrop Alice's and Bob's measurement results and obtains full information about the classical raw key generated out of them. A detailed discussion of this attack strategy can be found in [22].

In the next section, we look in detail at the general definition of basis transformations and their effect onto Bell states and entanglement swapping. Using these definitions, we discuss in the following sections the effects on the security of entanglement swapping based QKD protocols. Therefore, we look at the application of a general basis transformation by one communication party in Section III and at the application of two different basis transformations by each of the communication parties in Section IV. In the end, we sum up the implications of the results on the security of entanglement based QKD protocols.

 ISBN: 978-1-61208-380-3

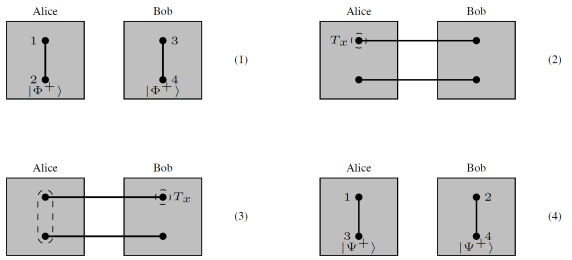

Figure 1. Sketch of a standard setup for an entanglement swapping based QKD protocol. Qubits 2 and 3 are exchanged (cf. picture (2)) and a basis transformation T_x is applied on qubit 1 and inverted by using T_x qubit 2.

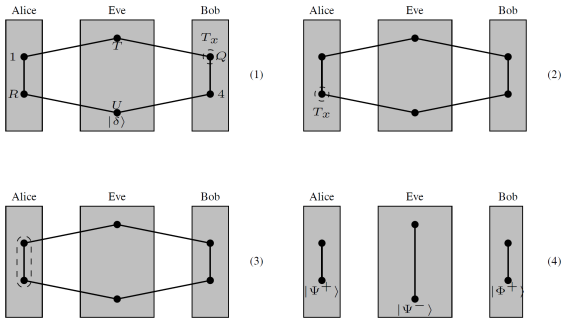

Figure 2. Illustration of the simulation attack on a standard setup for an entanglement swapping based QKD protocol. Due to the basis transformation T_x Eve will destroy the correlation between Alice and Bob.

II. Basis Transformations

In QKD, the most common way to detect the presence of an adversary is to use a random application of a basis transformation by one of the legitimate communication parties. This method can be found in prepare and measure protocols (e.g., in [1] or [3]) as well as entanglement swapping based protocols (e.g., in [13] [16] or the improved version of the protocol in [17]). The idea is to randomly alter the initial state to make it impossible for an adversary to eavesdrop the information transmitted without introducing a certain error rate, i.e., without being detected. The operation most commonly used in these protocols is the Hadamard operation, which is a transformation from the Z- into the X-basis. In general, a transformation T_x from the Z basis into the X-basis can be described as a rotation about the X-axis by some angle θ combined with two rotations about the Z-axis by some angle ϕ, i.e.,

$$T_x\big(\theta,\phi\big) = e^{i\phi} R_z\big(\phi\big) R_x\big(\theta\big) R_z\big(\phi\big). \tag{2}$$

The rotations about the X- or Z-axis are described in the most general way by the operators (cf. for example [23] for further details on rotation operators)

$$\begin{aligned} \mathrm{R}_x\big(\theta\big) &= \begin{pmatrix} \cos\frac{\theta}{2} & -i\sin\frac{\theta}{2} \\ -i\sin\frac{\theta}{2} & \cos\frac{\theta}{2} \end{pmatrix} \\ \mathrm{R}_z\big(\theta\big) &= \begin{pmatrix} e^{-i\theta/2} & 0 \\ 0 & e^{i\theta/2} \end{pmatrix}. \end{aligned} \tag{3}$$

Based on these operators, we directly obtain the effect of $T_x(\theta,\phi)$ on the computational basis

$$\begin{aligned} T_x\big(\theta,\phi\big)|0\rangle &= \cos\frac{\theta}{2}|0\rangle - i\, e^{i\phi}\sin\frac{\theta}{2}|1\rangle \\ T_x\big(\theta,\phi\big)|1\rangle &= -i\, e^{i\phi}\sin\frac{\theta}{2}|0\rangle + e^{2i\phi}\cos\frac{\theta}{2}|1\rangle. \end{aligned} \tag{4}$$

From these two equations above we immediately see that the Hadamard operation is just the special case where $\theta = \phi = \pi/2$.

In QKD protocols based on entanglement swapping, the basis transformation is usually applied onto one qubit of a Bell state. Taking the general transformation $T_x(\theta,\phi)$ from (2) into account, the Bell state $|\Phi^+\rangle$ changes into

$$\begin{aligned} T_x^{(1)}\big(\theta,\phi\big)|\Phi^+\rangle_{12} = \cos\frac{\theta}{2}\,\frac{1}{\sqrt{2}}\Big(|00\rangle + e^{2i\phi}|11\rangle\Big) \\ -i\, e^{i\phi}\sin\frac{\theta}{2}\,\frac{1}{\sqrt{2}}\Big(|01\rangle + |10\rangle\Big) \end{aligned} \tag{5}$$

and accordingly for the other Bell states. The superscript "(1)" in (5) indicates that the transformation $T_x\big(\theta,\phi\big)$ is applied on qubit 1. As a consequence, the application of $T_x(\theta,\phi)$ before the entanglement swapping is performed changes the results based on the angles θ and ϕ. In detail, we have the state

$$\begin{aligned} T_x^{(1)}\big(\theta,\phi\big)|\Phi^+\rangle_{12}|\Phi^+\rangle_{34} = \\ \frac{1}{2}\Big(&|\Phi^+\rangle_{13} T_x^{(2)}\big(\theta,\phi\big)|\Phi^+\rangle_{24} \\ &+|\Phi^-\rangle_{13} T_x^{(2)}\big(\theta,\phi\big)|\Phi^-\rangle_{24} \\ &+|\Psi^+\rangle_{13} T_x^{(2)}\big(\theta,\phi\big)|\Psi^+\rangle_{24} \\ &+|\Psi^-\rangle_{13} T_x^{(2)}\big(\theta,\phi\big)|\Psi^-\rangle_{24}\Big) \end{aligned} \tag{6}$$

upon which Alice performs her Bell state measurement on qubits 1 and 3 (cf. Figure 1). Here, the superscripts "(1)" and "(2)" in (6) indicate that after Alice's Bell state measurement on qubits 1 and 3 the transformation $T_x\big(\theta,\phi\big)$ swaps from qubit 1 onto qubit 2. When Bob performs his Bell state measurement on qubits 2 and 4, he obtains a result correlated to Alice's measurement outcome only with probability (cf. (5) and (6) above)

$$P_{corr} = \cos^2\frac{\theta}{2}\,\cos^2(\phi). \tag{7}$$

Otherwise, he obtains an uncorrelated result, which becomes a problem because Bob is no longer able to compute Alice's state based on his result and vice versa.

Fortunately, Bob can resolve this problem by transforming the state back into its original form. Following (6), where Alice performs $T_x\big(\theta,\phi\big)$ on qubit 1, he achieves that by applying the inverse $T_x^{-1}\big(\theta,\phi\big)$ on qubit 2 of his state. As we will see in the following section, if an adversary interferes with the communication, the effects of Alice's basis transformation can not be represented as in (6) any longer. Thus, even if Bob applies the inverse transformation, Alice's and Bob's results are uncorrelated to a certain amount. This amount is reflected in an error rate detected by Alice and Bob during post processing.

III. Single Application of General Basis Transformations

Previous works ([24] [25]) already deal with the scenarios where Alice or Bob or both parties randomly apply a simplified version of basis transformations. Therein, the simplification

addresses the angle ϕ, i.e., the rotation about the Z-axis. In the security discussions in [24], the angle ϕ is fixed at $\pi/2$ for reasons of simplicity. That means, the rotation about the Z-axis is constant at an angle of $\pi/2$ such that only the angle θ can be chosen freely.

In this section and the next one, we want to extend the results from [24] [25] by applying general basis transformations, which means Alice and Bob are able to choose both angles θ and ϕ in (2) freely. We are at first looking only on one party performing a basis transformation on the respective qubits and in the next section on two different basis transformations performed by each of the parties. For each scenario we will show, which values for θ and ϕ are optimal to give an adversary the least information about the raw key bits. In the course of the two scenarios, we will denote Alice's operation as $T_x\big(\theta_A, \phi_A\big)$ and, accordingly, Bob's operation as $T_x\big(\theta_B, \phi_B\big)$.

As already pointed out above, the application of the basis transformation occurs at random and Eve is able to obtain full information about Alice's and Bob's secret due to the structure of the state $|\delta\rangle$, if the two parties do not apply any basis transformation at all [24] [25]. Therefore, we look at first at the effects of a basis transformation at Alice's side. Her initial application of the general basis transformation $T_x\big(\theta_A, \phi_A\big)$ does alter the state $|\delta\rangle_{1QR4TU}$ introduced by Eve such that it is changed to

$$|\delta'\rangle_{1QR4TU} = T_x^{(1)}\big(\theta_A, \phi_A\big)|\delta\rangle_{1QR4TU} \tag{8}$$

After a little algebra, we see that Alice obtains all four Bell states with equal probability and after her measurement the state of the remaining qubits is

$$\begin{aligned} & e^{i\phi_A}\cos\frac{\theta_A}{2}\cos\phi_A\ |\Phi^+\rangle_{Q4}|\varphi_1\rangle_{TU} \\ -ie^{i\phi_A}\cos\frac{\theta_A}{2}\sin\phi_A\ & |\Phi^-\rangle_{Q4}|\varphi_2\rangle_{TU} \\ & -ie^{i\phi_A}\sin\frac{\theta_A}{2}\ |\Psi^+\rangle_{Q4}|\varphi_3\rangle_{TU} \end{aligned} \tag{9}$$

assuming Alice obtained $|\Phi^+\rangle_{1R}$. We are presenting just the state for this particular result in detail because it would be simply too complex to present the representation of the whole state for all possible outcomes here. Nevertheless, for the other three possible results the remaining qubits end up in a similar state, where only Bob's Bell states of the qubits Q and 4 as well as Eve's auxiliary states of the qubits T and U change accordingly to Alice's measurement result.

Before Bob performs his Bell state measurement, he has to reverse Alice's basis transformation. This can be achieved by applying $T_x^{-1}\big(\theta_A, \phi_A\big)$ on qubit Q in his possession. Whereas this would reverse the effect of Alice's basis transformation if no adversary is present, the structure of Eve's state $|\delta\rangle$ makes this reversion impossible, as already pointed out in the previous section. Therefore, Bob obtains the correlated state $|\Phi^+\rangle_{Q4}$ only with probability

$$P_{\Phi^+} = \frac{1}{4}\Big(3 + \cos\big(4\phi_A\big)\Big)\cos^4\frac{\theta_A}{2} + \sin^4\frac{\theta_A}{2} \tag{10}$$

Hence, due to Eve's intervention Bob obtains a result uncorrelated to Alice's outcome with probability

$$P_e = \frac{1}{2}\Big(\sin^2\theta_A + \cos^4\frac{\theta_A}{2}\sin^2\big(2\phi_A\big)\Big). \tag{11}$$

Assuming that Bob obtains $|\Phi^+\rangle_{Q4}$, i.e., the expected result based on Alice's measurement outcome, Eve obtains either $|\varphi_1\rangle$, $|\varphi_2\rangle$ or $|\varphi_3\rangle$ from her measurement on qubits T and U with the respective probabilities

$$\begin{aligned} P_{\varphi_1} &= \frac{\cos^4\frac{\theta_A}{2}\cos^4\phi_A}{\frac{1}{4}(3+\cos 4\phi_A)\cos^4\frac{\theta_A}{2} + \sin^4\frac{\theta_A}{2}} \\ P_{\varphi_2} &= \frac{\cos^4\frac{\theta_A}{2}\sin^4\phi_A}{\frac{1}{4}(3+\cos 4\phi_A)\cos^4\frac{\theta_A}{2} + \sin^4\frac{\theta_A}{2}} \\ P_{\varphi_3} &= \frac{-\sin^2\frac{\theta_A}{2}}{(3+\cos 4\phi_A)\cos^4\frac{\theta_A}{2} + 4\sin^4\frac{\theta_A}{2}} \end{aligned} \tag{12}$$

Furthermore, in case Bob measures an uncorrelated result, Eve obtains two out of the four auxiliary states $|\varphi_i\rangle$ at random. Hence, due to the basis transformation $T_x\big(\theta_A, \phi_A\big)$, Eve's auxiliary systems are less correlated to Bob's result compared to the application of a simple basis transformation as described in [24] [25]. In other words, Eve's information on Alice's and Bob's result is further reduced compared to the scenarios described therein.

Since Alice applies the basis transformation at random, i.e., with probability 1/2, the average error probability $\langle P_e\rangle$ can be directly computed using (11) and its variations based on Alice's measurement result as

$$\langle P_e\rangle = \frac{1}{4}\left[\sin^2\theta_A + \cos^4\frac{\theta_A}{2}\sin^2\Big(2\phi_A\Big)\right]. \tag{13}$$

Keeping in mind that Eve does not introduce any error when Alice does not use the basis transformation $T_x\big(\theta_A, \phi_A\big)$, the average collision probability $\langle P_c\rangle$ can be computed as (cf. also (12))

$$\begin{aligned} \langle P_c\rangle = \frac{1}{64}\Big(53 - 4\cos\theta_A + 7\cos\big(2\theta_A\big) \\ + 8\cos^4\frac{\theta_A}{2}\cos\big(4\phi_A\big)\Big). \end{aligned} \tag{14}$$

In further consequence this leads to the Shannon entropy H of the raw key, i.e.,

$$H = \frac{1}{2}\left[h\Big(\cos^2\frac{\theta_A}{2}\Big) + \cos^2\frac{\theta_A}{2}\ h\Big(\cos^2\phi_A\Big)\right]. \tag{15}$$

As we can directly see from Figure 3, the average error probability $\langle P_e\rangle$ has its maximum at 1/3 with $\theta_A \simeq 0.39183\pi$ and $\phi_A = \pi/4$ or $\phi_A = 3\pi/4$. For this choice of θ_A and ϕ_A we see from Figure 4 that the Shannon entropy is also maximal with $H \simeq 0.79248$. Hence, the adversary Eve is left with a mutual information of

$$I_{AE} = 1 - H = 0.20752 \tag{16}$$

This value for the mutual information is less than half of Eve's information on the raw key compared to the application of a Hadamard operation (cf. [1] [3] [21] [13]) or the application of a simplified basis transformation (cf. [24] [25]).

Unfortunately, the angle for $\theta_A \simeq 0.39183\pi$ to reach the maximum value is rather odd and difficult to realize in a practical implementation. In contrast, an angle $\theta_A = 3\pi/8$ is more convenient and much easier to realize. For this scenario we can compute from (13) an average error rate of $\langle P_e\rangle \simeq 0.33288$ and from (15) the respective Shannon entropy $H \simeq 0.79148$ (cf. also Figure 3 and Figure 4), which are both just insignificantly lower than their maximum values.

 ISBN: 978-1-61208-380-3

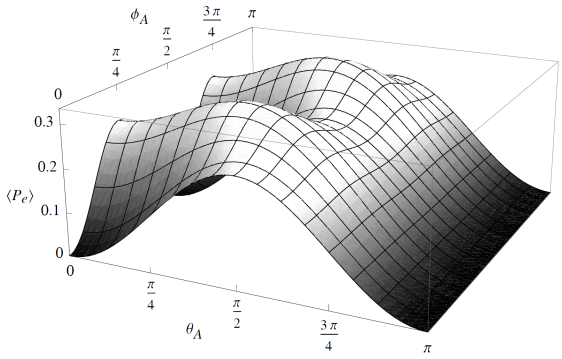

Figure 3. Error probability $\langle P_e \rangle$ depending on θ_A and ϕ_A

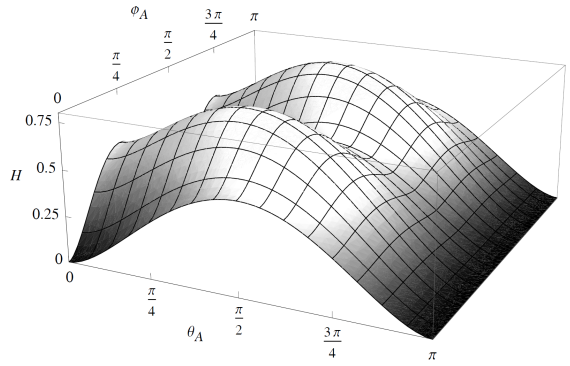

Figure 4. Shannon entropy H of the raw key depending on θ_A and ϕ_A

Accordingly, Eve's mutual information on the raw key is slightly above 20%, i.e., $I_{AE} \simeq 0.20852$. Hence, the security of the protocol is drastically increased using a general basis transformation compared to the application of a Hadamard operation.

IV. Combined Application of General Basis Transformations

In the previous section, we discussed the application of one general basis transformation $T_x\big(\theta_A, \phi_A\big)$ on Alice's side. It is easy to see that the results for the average error probability $\langle P_e \rangle$ in (13) as well as the Shannon entropy H in (15) are the same if only Bob randomly applies the basis transformation $T_x\big(\theta_B, \phi_B\big)$ on his side.

Hence, a more interesting scenario is the combined random application of two different basis transformations, i.e., $T_x\big(\theta_A, \phi_A\big)$ on Alice's side and $T_x\big(\theta_B, \phi_B\big)$ on Bob's side. The application of these two different basis transformations alters the state introduced by Eve accordingly to

$$|\delta'\rangle_{1QR4TU} = T_x^{(1)}\big(\theta_A, \phi_A\big)\; T_x^{(4)}\big(\theta_B, \phi_B\big)\; |\delta\rangle_{1QR4TU} \quad (17)$$

where again the superscripts "(1)" and "(4)" indicate that $T_x\big(\theta_A, \phi_A\big)$ is applied on qubit 1 and $T_x\big(\theta_B, \phi_B\big)$ on qubit 4, respectively. Following the protocol, Alice has to undo Bob's transformation using $T_x^{-1}\big(\theta_B, \phi_B\big)$ before she can perform her Bell state measurement. Similar to the application of one basis transformation described above, Alice obtains all four Bell states with equal probability from her measurement. The state of the remaining qubits changes in a way analogous to (9) above and Bob has to reverse Alice's transformation using $T_x^{-1}\big(\theta_A, \phi_A\big)$. Hence, when Bob performs his measurement on qubits Q and 4, he does not only obtain a result correlated to Alice's outcome, but all four possible Bell states with different probabilities such that an error is introduced in the protocol. As already discussed in the previous section, the results from Eve's measurement on qubits T and U are not fully correlated to Alice's and Bob's results and therefore Eve's information on the raw key bits is further reduced compared to the application of only one transformation.

Due to the fact that Alice as well as Bob choose at random whether they apply their respective basis transformation, the average error probability is calculated over all scenarios, i.e., no transformation is applied, either Alice or Bob applies $T_x\big(\theta_A, \phi_A\big)$ or $T_x\big(\theta_B, \phi_B\big)$, respectively, or both transformations are applied. Therefore, using the results from (13) above, the overall error probability can be computed as

$$\begin{aligned}
\langle P_e \rangle = {} & \frac{1}{8}\left[\sin^2\theta_A + \cos^4\frac{\theta_A}{2}\sin^2\Big(2\phi_A\Big)\right] \\
& + \frac{1}{8}\left[\sin^2\theta_B + \cos^4\frac{\theta_B}{2}\sin^2\Big(2\phi_B\Big)\right] \\
& + \frac{1}{16}\left[\sin^2\Big(\theta_A + \theta_B\Big)\right. \\
& \qquad \left. + \cos^4\frac{\theta_A + \theta_B}{2}\sin^2\Big(2\big(\phi_A + \phi_B\big)\Big)\right] \\
& + \frac{1}{16}\left[\sin^2\Big(\theta_A - \theta_B\Big)\right. \\
& \qquad \left. + \cos^4\frac{\theta_A - \theta_B}{2}\sin^2\Big(2\big(\phi_A - \phi_B\big)\Big)\right]
\end{aligned} \quad (18)$$

having its maximum at $\langle P_e \rangle \simeq 0.41071$. One possibility to reach the maximum is to choose the angles

$$\begin{aligned}
\theta_A &= 0 & \theta_B &\simeq 0.45437\pi \\
\phi_A &= \frac{\pi}{4} & \phi_B &= \frac{\pi}{4}.
\end{aligned} \quad (19)$$

In fact, as long as $\phi_A = \pi/4$ or $\phi_A = 3\pi/4$ the value of ϕ_B can be chosen freely to reach the maximum. Hence, the average error probability is plotted in Figure 5 taking $\phi_A = \phi_B = \pi/4$.

Following the same argumentation and using (15) from above, the Shannon entropy can be calculated as

$$\begin{aligned}
H = {} & \frac{1}{4}\left[h\Big(\cos^2\frac{\theta_A}{2}\Big) + \cos^2\frac{\theta_A}{2}\; h\Big(\cos^2\phi_A\Big)\right] \\
& + \frac{1}{4}\left[h\Big(\cos^2\frac{\theta_B}{2}\Big) + \cos^2\frac{\theta_B}{2}\; h\Big(\cos^2\phi_B\Big)\right] \\
& + \frac{1}{8}\left[h\Big(\cos^2\frac{\theta_A + \theta_B}{2}\Big)\right. \\
& \qquad \left. + \cos^2\frac{\theta_A + \theta_B}{2}\; h\Big(\cos^2\big(\phi_A + \phi_B\big)\Big)\right] \\
& + \frac{1}{8}\left[h\Big(\cos^2\frac{\theta_A - \theta_B}{2}\Big)\right. \\
& \qquad \left. + \cos^2\frac{\theta_A - \theta_B}{2}\; h\Big(\cos^2\big(\phi_A - \phi_B\big)\Big)\right]
\end{aligned} \quad (20)$$

having its maximum at $H \simeq 0.9452$ (cf. Figure 6 for a plot of (20) taking $\phi_A = \phi_B = \pi/4$). This maximum is reached, for

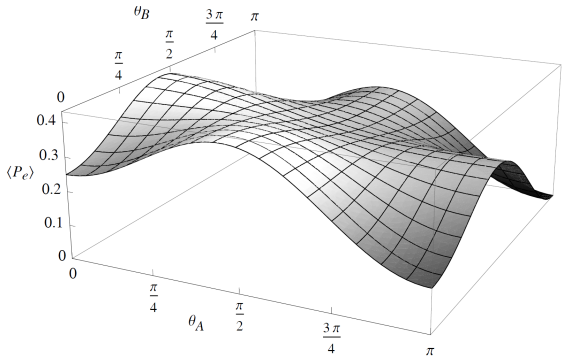

Figure 5. Error probability $\langle P_e \rangle$ depending on θ_A and θ_B. The remaining parameters ϕ_A and ϕ_B are fixed at $\pi/4$.

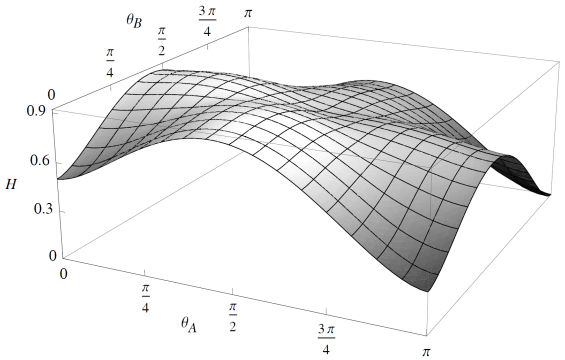

Figure 6. Shannon entropy H of the raw key depending on θ_A and θ_B. The remaining parameters ϕ_A and ϕ_B are fixed at $\pi/4$.

example, using

$$\begin{aligned} \theta_A &\simeq -0.18865\pi \qquad \theta_B \simeq 0.42765\pi \\ \phi_A &\simeq -0.22405\pi \qquad \phi_B \simeq 0.36218\pi. \end{aligned} \tag{21}$$

The maximal Shannon entropy can also be reached using other values but they are not as nicely distributed as in the case of the average error probability.

Looking again at set of values for $\theta_{\{A,B\}}$ and $\phi_{\{A,B\}}$, which are more suitable for a physical implementation than the values mentioned above, one possibility for Alice and Bob is to choose

$$\begin{aligned} \theta_A &= -\frac{3\pi}{16} \qquad \theta_B = \frac{7\pi}{16} \\ \phi_A &= -\frac{\pi}{4} \qquad \phi_B = \frac{3\pi}{8} \end{aligned} \tag{22}$$

leading to an almost optimal Shannon entropy $H \simeq 0.9399$ and a average respective error probability $\langle P_e \rangle \simeq 0.39288$. In this context, more suitable for a physical implementation means that a transformation about an angle of $\pi/4$ or $3\pi/8$ is easier to realize in a laboratory than an angle of 0.42765π. Keeping ϕ_A and ϕ_B fixed – as already discussed in the previous section – such that

$$\begin{aligned} \theta_A &= \frac{3\pi}{16} \qquad \theta_B = \frac{7\pi}{16} \\ \phi_A &= \frac{\pi}{4} \qquad \phi_B = \frac{\pi}{4} \end{aligned} \tag{23}$$

the same average error probability $\langle P_e \rangle \simeq 0.39288$ and a slightly smaller Shannon entropy $H \simeq 0.91223$ compared to the previous values are achieved. Hence, we see that using a set of parameters more suitable for a physical implementation still results in a high error rate and leaves Eve's mutual information I_{AE} below 10%.

V. Results and Implications

The results presented in the previous sections have direct implications on the security of QKD protocols based on entanglement swapping. Where in some QKD protocols [13] [16] [17] a random application of a Hadamard operation is used to detect an eavesdropper and secure the protocol, the above results indicate that the Hadamard operation is not the optimal choice. Using the Hadamard operation leaves an adversary with a mutual information $I_{AE} = 0.5$ and an expected error probability $\langle P_e \rangle = 0.25$ (cf. Table I), which is comparable to standard prepare and measure protocols [1]–[3].

Giving Alice an increased degree of freedom, i.e., choosing both θ_A and ϕ_A freely, she is able to further decrease the adversary's information about the raw key bits. By shifting ϕ_A from $\pi/2$ to $\pi/4$ and θ_A from $\pi/2$ or $\pi/4$ to $3\pi/8$, the adversary's information is reduced to $I_{AE} \simeq 0.208$ (cf. (15)). This is a reduction by almost 60% compared to QKD schemes described in [1]–[3] [13] [17] and more than 50% compared to the combined application of two different basis transformations (cf. also [24] [25]). At the same time, the expected error probability is increased by one third to $\langle P_e \rangle \simeq 0.333$ (cf. (13)). Hence, an adversary does not only obtain fewer information about the raw key bits but also introduces more errors and therefore is easier to detect.

Following these arguments, the best strategy for Alice and Bob is to apply different basis transformations at random to reduce the adversary's information to a minimum. As already pointed out above, this minimum of $I_{AE} \simeq 0.0548$ is reached with a rather odd configuration for $\theta_{\{A,B\}}$ and $\phi_{\{A,B\}}$ as described in the previous section. Hence, it is important to look at configurations more suitable for physical implementations, i.e., configurations of $\theta_{\{A,B\}}$ and $\phi_{\{A,B\}}$ described by simpler fractions of π as given in (22) and (23). In this case, we showed that $\phi_{\{A,B\}}$ can be fixed at $\phi_A = \phi_B = \pi/4$ and with $\theta_A = 3\pi/16$ and $\theta_B = 7\pi/16$ almost maximal values can be achieved resulting in $I_{AE} \simeq 0.088$ and $\langle P_e \rangle \simeq 0.393$ (cf. (23) and also Table I).

Regarding physical implementations, another – even simpler – configuration can be found, involving only $\pi/2$ and $\pi/4$ rotations (cf. Table I). In this case, $\theta_A = 0$, $\phi_A = \pi/4$ and $\theta_B = \phi_B = \pi/2$, which leaves the expected error probability at $\langle P_e \rangle \simeq 0.334$. The adversary's information is nowhere near the minimum but still rather low at $I_{AE} = 0.125$.

In terms of security, these results represent a huge advantage over QKD protocols based on entanglement swapping [13], [16], [17] or standard prepare and measure protocols [1]–[3]. As pointed out, such protocols usually have an expected error probability of $\langle P_e \rangle = 0.25$ and a mutual information $I_{AE} = 0.5$. Due to the four degrees of freedom, the error rate is between one third ($\langle P_e \rangle \simeq 0.334$) and more than one half ($\langle P_e \rangle = 0.411$) higher in the scenarios described here than in the standard protocols, which makes it easier to detect an adversary.

 ISBN: 978-1-61208-380-3

TABLE I. OVERVIEW OF THE ERROR RATE $\langle P_E \rangle$ AND EVE'S INFORMATION I_{AE} ON THE RAW KEY BITS FOR DIFFERENT VALUES OF $\theta_{A,B}$ AND $\phi_{A,B}$.

	$\phi_A = 0$	$\phi_A = \frac{\pi}{2}$	$\phi_A = \frac{\pi}{4}$
$\phi_B = 0$	$\theta_A = 0, \theta_B = 0$ $\langle P_e \rangle = 0$ $I_{AE} = 1$	$\theta_A = \frac{\pi}{2}, \theta_B = 0$ $\langle P_e \rangle = 0.25$ $I_{AE} = 0.5$	$\theta_A = \frac{3\pi}{8}, \theta_B = 0$ $\langle P_e \rangle \simeq 0.333$ $I_{AE} \simeq 0.208$
$\phi_B = \frac{\pi}{2}$		$\theta_A = \frac{\pi}{2}, \theta_B = \frac{\pi}{4}$ $\langle P_e \rangle = 0.25$ $I_{AE} \simeq 0.45$	$\theta_A = 0, \theta_B = \frac{\pi}{2}$ $\langle P_e \rangle \simeq 0.40625$ $I_{AE} = 0.125$
$\phi_B = \frac{\pi}{4}$			$\theta_A = \frac{3\pi}{16}, \theta_B = \frac{7\pi}{16}$ $\langle P_e \rangle = 0.393$ $I_{AE} = 0.088$

VI. CONCLUSION

In this article, we discussed the effects of basis transformations on the security of quantum key distribution protocols based on entanglement swapping. We showed that the Hadamard operation, a transformation from the Z- into the X-basis often used in prepare and measure protocols, is not optimal in connection with entanglement swapping based protocols. Starting from a general basis transformation described by two angles θ and ϕ, we inspected the effects on the security when the adversary follows a collective attack strategy. We showed that the application of a basis transformation by one of the communication parties decreases the adversary's information to about $I_{AE} \simeq 0.2075$, which is less than half of the information compared to an application of the Hadamard operation. At the same time, the average error probability introduced by the presence of the adversary increases to $\langle P_e \rangle = 1/3$. Hence, the application of one general basis transformation is more effective, i.e., reveals even less information to the adversary, than the application of a simplified basis transformation as given in [24] [25]. A combined application of two different basis transformations further reduces the adversary's information to about $I_{AE} \simeq 0.0548$ at an average error probability of slightly more than 0.41.

Since the configuration of the angles θ and ϕ to reach these maximal values is not very suitable for a physical implementation, we also showed that these maximal values are almost reached with more convenient values for θ and ϕ. In this case, the adversary's information is still $I_{AE} < 0.1$ with an average error rate $\langle P_e \rangle \simeq 0.393$ for a combined application of two basis transformations.

These results have a direct impact on the security of such protocols. Due to the reduced information of an adversary and the high error probability introduced during the attack strategy, Alice and Bob are able to accept higher error thresholds compared to standard entanglement-based QKD protocols.

REFERENCES

[1] C. H. Bennett and G. Brassard, "Public Key Distribution and Coin Tossing," in Proceedings of the IEEE International Conference on Computers, Systems, and Signal Processing. IEEE Press, 1984, pp. 175–179.

[2] A. Ekert, "Quantum Cryptography Based on Bell's Theorem," Phys. Rev. Lett., vol. 67, no. 6, 1991, pp. 661–663.

[3] C. H. Bennett, G. Brassard, and N. D. Mermin, "Quantum Cryptography without Bell's Theorem," Phys. Rev. Lett., vol. 68, no. 5, 1992, pp. 557–559.

[4] D. Bruss, "Optimal Eavesdropping in Quantum Cryptography with Six States," Phys. Rev. Lett, vol. 81, no. 14, 1998, pp. 3018–3021.

[5] A. Muller, H. Zbinden, and N. Gisin, "Quantum Cryptography over 23 km in Installed Under-Lake Telecom Fibre," Europhys. Lett., vol. 33, no. 5, 1996, pp. 335–339.

[6] A. Poppe et al., "Practical Quantum Key Distribution with Polarization Entangled Photons," Optics Express, vol. 12, no. 16, 2004, pp. 3865–3871.

[7] A. Poppe, M. Peev, and O. Maurhart, "Outline of the SECOQC Quantum-Key-Distribution Network in Vienna," Int. J. of Quant. Inf., vol. 6, no. 2, 2008, pp. 209–218.

[8] M. Peev et al., "The SECOQC Quantum Key Distribution Network in Vienna," New Journal of Physics, vol. 11, no. 7, 2009, p. 075001.

[9] N. Lütkenhaus, "Security Against Eavesdropping Attacks in Quantum Cryptography," Phys. Rev. A, vol. 54, no. 1, 1996, pp. 97–111.

[10] ——, "Security Against Individual Attacks for Realistic Quantum Key Distribution," Phys. Rev. A, vol. 61, no. 5, 2000, p. 052304.

[11] P. Shor and J. Preskill, "Simple Proof of Security of the BB84 Quantum Key Distribution Protocol," Phys. Rev. Lett., vol. 85, no. 2, 2000, pp. 441–444.

[12] A. Cabello, "Quantum Key Distribution without Alternative Measurements," Phys. Rev. A, vol. 61, no. 5, 2000, p. 052312.

[13] ——, "Reply to "Comment on "Quantum Key Distribution without Alternative Measurements"","," Phys. Rev. A, vol. 63, no. 3, 2001, p. 036302.

[14] ——, "Multiparty Key Distribution and Secret Sharing Based on Entanglement Swapping," quant-ph/0009025 v1, 2000.

[15] F.-G. Deng, G. L. Long, and X.-S. Liu, "Two-step quantum direct communication protocol using the Einstein-Podolsky-Rosen pair block," Phys. Rev. A, vol. 68, no. 4, 2003, p. 042317.

[16] D. Song, "Secure Key Distribution by Swapping Quantum Entanglement," Phys. Rev. A, vol. 69, no. 3, 2004, p. 034301.

[17] C. Li, Z. Wang, C.-F. Wu, H.-S. Song, and L. Zhou, "Certain Quantum Key Distribution achieved by using Bell States," International Journal of Quantum Information, vol. 4, no. 6, 2006, pp. 899–906.

[18] C. H. Bennett et al., "Teleporting an Unknown Quantum State via Dual Classical and EPR Channels," Phys. Rev. Lett., vol. 70, no. 13, 1993, pp. 1895–1899.

[19] M. Zukowski, A. Zeilinger, M. A. Horne, and A. K. Ekert, ""Event-Ready-Detectors" Bell State Measurement via Entanglement Swapping," Phys. Rev. Lett., vol. 71, no. 26, 1993, pp. 4287–4290.

[20] B. Yurke and D. Stolen, "Einstein-Podolsky-Rosen Effects from Independent Particle Sources," Phys. Rev. Lett., vol. 68, no. 9, 1992, pp. 1251–1254.

[21] Y.-S. Zhang, C.-F. Li, and G.-C. Guo, "Comment on "Quantum Key Distribution without Alternative Measurements"," Phys. Rev. A, vol. 63, no. 3, 2001, p. 036301.

[22] S. Schauer and M. Suda, "A Novel Attack Strategy on Entanglement Swapping QKD Protocols," Int. J. of Quant. Inf., vol. 6, no. 4, 2008, pp. 841–858.

[23] M. A. Nielsen and I. L. Chuang, Quantum Computation and Quantum Information. Cambridge University Press, 2000.

[24] S. Schauer and M. Suda, "Security of Entanglement Swapping QKD Protocols against Collective Attacks," in ICQNM 2012 , The Sixth International Conference on Quantum, Nano and Micro Technologies. IARIA, 2012, pp. 60–64.

[25] ——, "Application of the Simulation Attack on Entanglement Swapping Based QKD and QSS Protocols," International Journal on Advances in Systems and Measurements, vol. 6, no. 1&2, 2013, pp. 137–148.

 ISBN: 978-1-61208-380-3

Reconstitution of Ryanodine Receptor/Ca^{2+} Release Channels in S-layer Supported Lipid Membranes

Vanessa-Dominique Larisch, Angelika Schrems,
Uwe B. Sleytr, Bernhard Schuster
Department of NanoBiotechnology
University of Natural Resources and Life Sciences, Vienna
Vienna, Austria
{bernhard.schuster; uwe.sleytr}@boku.ac.at

Martin Hohenegger
Institute of Pharmacology
Medical University Vienna
Vienna, Austria
martin.hohenegger@meduniwien.ac.at

***Abstract*—A great challenge nowadays is the systematic study on medicinal relevant functional (trans)membrane proteins reconstituted in tunable biomimetic model lipid membranes. Ryanodine receptor/Ca^{2+} release channels (RyRs), integral membrane proteins present in various mammalian tissues, are of great importance for muscle contraction. For the present study, the RyR isoform 1 (RyR1) was isolated from the skeletal muscle of rabbits. Here, we show the reconstitution of RyR1 into an artificial model lipid system, the so-called S-layer supported lipid membrane (SsLM). Bacterial crystalline surface layer (S-layer) proteins render the possibility to generate solid supported membranes of high longevity on various supports in order to enable investigations by a great variety of surface-sensitive techniques. According to preliminary results, RyR1 was successfully reconstituted into the SsLM as proven by quartz crystal microbalance with dissipation monitoring. Moreover, control experiments revealed that RyR1 did not stick to an S-layer lattice without an attached lipid membrane. Hence, evidence is provided that the SsLM as multifunctional interface might constitute a pharmaceutically interesting platform to investigate, e.g., the effect of a broad range of drugs on reconstituted RyR1 or other membrane proteins in general.**

Keywords-biomimetics; supported lipid membrane; S-layer protein; functional reconstitution; ryanodine receptor/Ca^{2+} release channel.

I. INTRODUCTION

Membrane proteins are essential for life and offer various functions by serving as key components in inter- and intracellular communication. Therefore, they represent very attractive drug targets, but at the same time, studying membrane proteins and their pharmacological applications is a highly challenging task [1]. In an effort to develop synthetic membrane mimics of the natural cell membrane in both, structure and function, fabrication of a supported lipid bilayer on a solid substrate is receiving growing attention [2]. Solid supported lipid membranes are a well-known class of model membranes, extremely useful for studying biophysical and biochemical properties of biological membranes, their constituted lipids and in particular (trans)membrane proteins [2]-[4]. In order to design a synthetic lipid membrane that overcomes the challenges facing membrane-spanning protein reconstitution, a strategy based on surface (S-) layer proteins acting as biocompatible cushions separating the lipid bilayer from the solid support has been developed (Figure 1) [3][4]. The result of this approach based on the building principle of archaeal cell envelope structures are the so-called S-layer supported lipid membranes (SsLMs). The latter provide many advantages, e.g. reduces the non-specific binding of proteins to solid substrate, increase lipid membrane stability and longevity, provides a lubricant layer allowing the lipid bilayers to remain mobile, allows insertion of bulky transmembrane proteins into the lipid bilayer, and may assist self-healing of local defects in lipid bilayers deposited on large supports [3][4].

S-layer lattices are two-dimensional arrays of proteinaceous subunits which constitute the common surface structure of almost all archaea and most bacteria [3][5]. Bacterial S-layers have the unique property that, following disruption by chemical agents from cells, monomers of the protein can reassemble to their original lattice structure in suspension, on solid surfaces, at air–water interfaces, and on phospholipid mono- and bilayers. Most bacterial S-layer lattices are composed of a single protein or glycoprotein species having a center-to-center spacing of approximately 5–30 nm, are 5 to 10 nm thick and show a smooth outer and a more corrugated inner surface (Figure 1). The lattices with a surface porosity ranging between 30–70% are composed of identical pores with a diameter of 2 to 8 nm [3]-[5].

One of the major advantages of planar supported lipid bilayer models is the wide range of surface-sensitive techniques, which can be applied to study the overall membrane characteristics and its constituents [2]. Quartz crystal microbalance with dissipation monitoring (QCM-D)

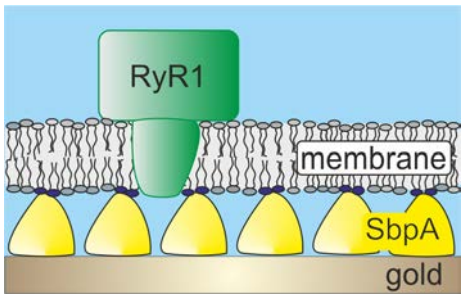

Figure 1. Schematic drawing of a ryanodine receptor/Ca2+ release channel (RyR1) incorporated in an S-layer (SbpA) supported lipid membrane.

 ISBN: 978-1-61208-380-3

is one of these techniques, which allow real time quantitative measurements of the shift in frequency, which corresponds directly to the mass of bound material on the sensor surface including the associated liquid medium. Moreover, also the energy loss (dissipation) gives information related to changes of the viscoelastic properties of the deposited layer [6].

The present study is motivated by the high demand of studying responsive membrane proteins in a biomimetic environment. This intention is of paramount importance as the results of genome mapping showed that approximately one-third of all genes of an organism encode for membrane proteins, which are key factors in cell's metabolism and thus, in health and disease. Moreover, membrane proteins constitute preferred targets for pharmaceuticals (at present more than 60% of all consumed drugs) [1].

In the present study, RyR1 has been chosen to be reconstituted in SsLMs (Figure 1) since RyR1 is related to several severe human diseases, such as malignant hyperthermia, myocardial ischemia and central core disease [7][8]. The typical activator of the receptor is ryanodine, a plant alkaloid isolated from *Ryania speciosa.* It was soon discovered that ryanodine can cause muscles to contract or to reduce contractile force [8]. Experiments revealed that RyR1 activation can be reversed to inhibition of Ca^{2+} release after prolonged incubation with ryanodine in the micro-molar range. In general, RyRs are modulated by endogenous as well as pharmacological effectors. Ca^{2+} represents the most important endogenous factor, whereby its release from the sarcoplasmic reticulum (SR) is thought to be triggered by an action potential. As a result, the intracellular concentration of Ca^{2+} is increasing, which leads to the opening of other ion channels that are regulated by RyR1 and the subsequent release of Ca^{2+} from the SR [7].

To sum up, planar model lipid membranes, in particular SsLMs functionalized with pharmacologically relevant membrane proteins like the RyR1 may receive widespread recognition in drug discovery and protein–ligand screening. In future, the increased knowledge on membrane proteins will allow rebuilding sensory organs, e.g., an artificial nose, and are of high interest for the development of biosensors based on the function of membrane proteins [1]-[5].

In the following, Section II describes the S-layer protein isolation and modification, lipid membrane formation on the S-layer lattice, isolation of RyR1 and QCM-D measurements to provide evidence for the SsLM formation and RyR1 incorporation. Section III A deals with the assembly of the SsLM, whereas Sections III B and III C report on the reconstitution of RyR1 in the SsLM out from proteo-liposomes with and without CHAPS, respectively. Section III D shows that RyR1 cannot be attached to a plain S-layer lattice without any lipid membrane. Finally, Section IV gives a conclusion and outlook on the planned future work.

II. METHODS

Isolation of S-layer proteins The bacterial S-layer protein SbpA was isolated from *Lysinibacillus sphaericus* CCM 2177 as previously described [9]. The protein solution (0.1 mg/mL in recrystallization buffer: 0.5 mM Tris-HCl, 10 mM $CaCl_2$, pH 9) was self-assembled on gold substrates for 3 hours. A subsequent rinsing step with water was applied in order to remove excess protein.

Chemical activation of SbpA The S-layer protein was modified with 1-ethyl-3-(3-dimethylaminopropyl) carbodi-imide hydrochloride (EDC, Sigma-Aldrich; 15 mg/mL, pH 4.5). Subsequently, vesicles containing 1,2-dimyristoyl-*sn*-glycero-3-phospho-ethanolamine (DMPE) were bound via EDC coupling onto the activated SbpA lattice [10].

S-layer supported lipid membrane formation Phosphatidylcholine isolated from egg yolk (Egg PC) and DMPE were purchased from Sigma-Aldrich. The β-diketone ligand has been synthesized as described elsewhere [10]. Phospholipids with 1% β-diketone ligand were dissolved in chloroform and dried under vacuum for at least 3 hours at 45°C. The lipid film was subsequently rehydrated and extruded 21 times through a polycarbonate membrane (Whatman, UK) by using a Mini Extruder (Avanti Polar Lipid Inc, USA) to form a suspension of large unilamellar vesicles (LUVs). Before use, LUVs were diluted in sucrose/ glucose (1/2) to give a final lipid concentration of 1 mg/mL.

Isolation of the ryanodine receptor/Ca^{2+} release channel RyR1 was isolated from heavy SR of rabbit skeletal muscle as described elsewhere [11]. RyR1 was provided in unilamellar proteoliposomes composed of α-phosphatidyl-choline and approx. 0.1% 3-[(3-cholamidopropyl) dimethyl-ammonio]-1-propane sulfonate hydrate (CHAPS). The stock RyR1 concentration was 1.38 mg/mL, which was diluted 1:50, 1:100 and 1:500 as indicated in each experiment.

Quartz crystal microbalance with dissipation monitoring (QCM-D) The QCM-D E4 device (Q-Sense AB, Sweden) was operated with gold-coated quartz crystal sensors (QSX 301, Q-Sense AB) to measure the shift in frequency, Δf, and dissipation, ΔD, as a function of time [6]. QCM-D experiments were measured at 25 ± 0.02°C. All given data were measured at the 5th overtone. The flow rate was 25 µL/min for all fluid injections and rinsing steps.

III. RESULTS AND DISCUSSION

A. Assembly of S-layer supported lipid membranes

QCM-D was not only applied to follow SsLM formation, (i.e., recrystallization of S-layer proteins on gold sensor and successive formation of a lipid bilayer by binding and subsequent fusion of LUVs) but was also used to investigate the incorporation features of RyR1. Representative measurements of Δf and ΔD in the course of the formation of the SsLM and interaction of the latter with RyR1 as a function of time are shown in Figure 2. In a first step, the assembly of S-layer proteins from solution on gold sensors was determined and showed a rapid decrease of Δf to ~-75 Hz and a slight increase of ΔD ($<1\times10^{-6}$) (Figure 2; Table 1). Both values recorded by QCM-D for S-layer proteins recrystallization on the gold sensor are in good agreement with previously published work [2][10][12].

Two obstacles face bilayer formation onto S-layer protein lattices; vesicle attachment and successive spontaneous vesicle fusion. The S-layer lattice has a so-called antifouling characteristic, meaning that nothing sticks to it and hence,

 ISBN: 978-1-61208-380-3

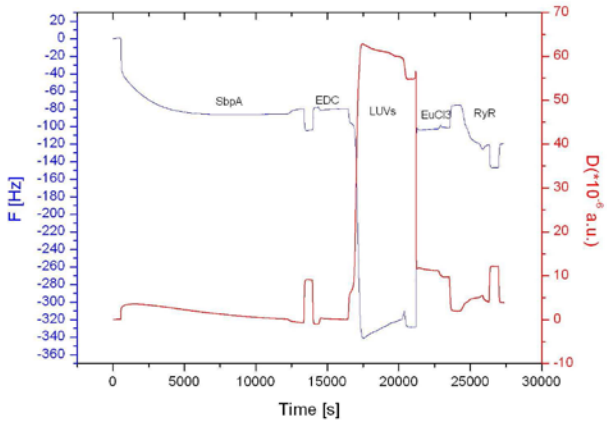

Figure 2. QCM-D measurement showing the SsLM formation process and the subsequent incorporation of RyR1 out from dialyzed proteoliposomes.

vesicles would simply roll over the proteinaceous lattice [3]. This intrinsic feature may be a biological function of the S-layer lattice covering many prokaryotic cells. Therefore, EDC was used to activate the carboxyl groups of the S-layer protein forming highly reactive *O*-acylisourea intermediates. Subsequently a solution of vesicles (LUVs) comprising of Egg PC, DMPE and β-diketone ligand was passed over the S-layer lattice [10]. This composition was chosen for several reasons: The Egg PC is the bulk component forming the spherical vesicle, DMPE as linker molecule is covalently bound with its terminal amino group to the activated S-layer protein, and the amphiphilic β-diketone ligand molecules incorporated in the LUVs master their fusion by the inter-vesicular complex formation of two β-diketone ligands with one Eu^{3+}-ion. The accompanied dramatic structural change of the lipid layer can nicely be investigated by QCM-D. Initially, the layer composed of bound vesicles gave rise to a huge decrease in Δf (~-340 Hz) and increase in ΔD (~65 × 10^{-6}), corresponding to a very soft, highly water–containing vesicular layer. After Eu^{3+}-ion triggered vesicle fusion, Δf increased instantly to ~-100 Hz and ΔD decreased to ~10×10^{-6} (Figure 2). The pronounced shift in Δf and ΔD provide clear evidence for the change of the attached lipid structure. The obtained difference in Δf between the S-layer lattice with and without an attached lipid membrane is approximately 22 Hz (Table 1). This value is in good agreement with the previously reported QCM-D response for bilayer lipid membrane formation [10][13]. In addition, the same ΔD was previously reported for SsLMs [10]. Subsequently the lipid membranes were rinsed with recrystallization buffer to remove unbound excess material.

TABLE 1: QCM-D DATA FOR SSLM FORMATION AND RYR1 RECONSTITUTION USING DIALYZED (A) AND UNDIALYZED (B) PROTEOLIPOSOMES.

	Data calculated from QCM-D measurements; n = 8		
	Frequency [Hz]	***Dissipation×10^{-6}***	***Mass [ng]***
SbpA	74.5 ± 5.4	1.01 ± 0.05	1317.7 ± 95.0
SsLM	21.8 ± 1.3	8.69 ± 0.02	385.4 ± 22.1
RyR1$^{(A)}$	33.0 ± 22.9	0.91 ± 2.71	584.3 ± 386.3
RyR1$^{(B)}$	15.6 ± 4.9	-6.07 ± 0.42	275.2 ± 86.1

B. Reconstitution of RyR1 via undialyzed proteoliposomes

Addition of RyR1 proteoliposomes (1:100 dilution; 13.8 µg/mL RyR1) causes a significant shift in Δf indicating the attachment of RyR1 to the lipid membrane. Due to the moderate shift in Δf and ΔD, an attachment of intact proteoliposomes can be excluded. The incorporation of RyR1 is evidenced by the fact that Δf does not decrease after rinsing. The difference in Δf in respect to the SsLM was determined to be ~33 Hz. This value is corresponding to a mass of 584.3 ng. Mean values of Δf, ΔD, and changes in mass of repeated measurements are summarized in Table 1. Since proteoliposomes hosting RyR1 still contained CHAPS, it is not possible to determine the most probably small influence of the detergent on the bound mass.

To investigate the influence of the RyR1 concentration on its incorporation into the SsLM, the experiment was repeated with a lower (1:500 dilution – 2.76 µg/mL) and a higher concentration (1:50 dilution – 27.6 µg/mL) of RyR1. For the 1:500 dilution Δf was determined to be -19.5 Hz. Hence, the decrease in Δf was slightly more than half of the value observed for the 1:100 dilution. Looking at the mass change, the attached mass was slightly higher (344.6 ng) than half of the mass determined for the 1:100 dilution. In contrast, Δf was -30.1 Hz for the 1:50 dilution. Although the concentration of RyR1 was the double value than for the 1:100 dilution, the decrease in Δf was approximately 3 Hz lower. The calculated mass of incorporated RyR1 was even slightly lower (532.1 ng) despite the higher concentration. However, as RyR1 is very bulky (29 nm × 29 nm per RyR1 complex [14]), there is a limitation in the number of incorporated RyR1 simply by the available membrane area, which is theoretically reached at the 1:100 dilution.

C. Reconstitution of RyR1 via dialyzed proteoliposomes

To investigate the influence of CHAPS on the incorporation of RyR1 into the SsLM, the experiment were repeated with the 1:100 dilution of dialyzed RyR1 proteoliposomes (Figure 2). The shifts in Δf after formation of an S-layer lattice and closed bilayer were equal to those observed in previous experiments. Table 1 shows that Δf as well as the calculated mass for incorporated RyR1 is much lower for dialysis treated proteoliposomes than for the previous set of experiments without dialysis (275 ng vs. 584 ng, respectively). This finding could be explained by the absence of CHAPS, which was still present in the undialyzed proteoliposomes.

Another interesting result is the decrease in dissipation: In the experiment with undialyzed RyR1, ΔD between SsLM and incorporated RyR1 was determined to $+0.91\times10^{-6}$. In contrast to this value, the difference for dialyzed RyR1 has a negative value (-6×10^{-6}; Table1). Hence, it is conceivable that the lipid membrane containing a detergent, which may induce defects in the lipid bilayer structure, behaves more

 ISBN: 978-1-61208-380-3

viscoelastic than the membrane purely comprised of phospholipid molecules.

All experiments both, with dialyzed and undialyzed RyR1 proteoliposomes evidenced the incorporation of RyR1 into solid SsLMs. The use of proteoliposomes lacking CHAPS gave a much lower value for mass change indicating that the presence of CHAPS facilitate the incorporation of RyR1 via proteoliposomes into the SsLM. Another explanation for the different results could be that the protein content was higher in the undialyzed assay, thereby resulting in a higher mass attached to the sensor (Table1). Finally, one cannot exclude that a certain part of the total mass determined by QCM-D has to be referred to the detergent CHAPS.

D. Negative control

All previously performed experiments provide evidence for the incorporation of RyR1 into SsLMs. To confirm that the receptor is not attached due to unspecific adsorption to the naked SbpA lattice, control experiments without previous formation of a lipid membrane were conducted. The attachment of RyR1 (13.8 µg/mL) directly on an S-layer lattice is clearly visible by the decrease in Δf (data not shown). However, flushing of the system causes an increase in Δf until the initial value for the SbpA lattice was reached. Thus, the whole mass assigned to RyR1 attached to the S-layer lattice was washed away. This result proves that RyR1 can successfully be reconstituted into an SsLM but it does not stick to a plain S-layer lattice on a sustained basis.

IV. CONCLUSION AND FUTURE WORK

The preliminary data provide evidence, that the SsLM constitute a promising platform for studying transmembrane proteins in particular as RyR1 is a huge 2.3 MDa homo-tetrameric, membrane-protruding complex [14]. Moreover, SsLMs do not get disintegrated by the presence of detergents like CHAPS. The future work will elucidate the orientation of the reconstituted RyR1 in the SsLM by binding of, e.g., fluorescently labelled ryanodine. Also replacement of the latter by natural ryanodine will give information on the correct folding of RyR1. Electrophysiological studies on the modulation of (single) ryanodine receptor/Ca^{2+} release channel by effectors and drugs are the ultimate goal of this ongoing work. Finally, other receptor proteins, in particular the important class of G-protein coupled receptors will be functionally reconstituted and studied in the multifunctional interface of this robust platform. In this context it is interesting to note that recently a rapid technique for the sampling of membrane-associated proteins from the surface of a living cell and their subsequent deposition into SsLM has been achieved [15]. The future aims are the rebuilding of sensory organs like, e.g., artificial noses or tongues and the design of highly sensitive and specific biosensors based on arrays of responsive membrane proteins [16].

ACKNOWLEDGMENT

Financial support provided from the Austrian Science Fund (FWF), project 20256-B11 is gratefully acknowledged.

REFERENCES

[1] L. Tiefenauer, and S. Demarche, “Challenges in the development of functional assays of membrane proteins” Materials, vol. 5, Nov. 2012, pp. 2205–2242, doi:10.3390/ma5112205.

[2] W. Knoll et al. “Solid supported functional lipid membranes: New concepts for the biomimetic functionalization of solid surfaces” Biointerphases, vol 3, Jun. 2008, pp. FA125-FA135, doi:10.1116/1.2913612.

[3] U.B. Sleytr, B. Schuster, E.M. Egelseer, D. Pum, “S–layers: principles and applications”. FEMS Microbiol. Rev., in press, 2014, doi:10.1111/1574-6976.12063.

[4] B. Schuster, and U.B. Sleytr, “Biomimetic interfaces comprised of S-layer proteins, lipid membranes and membrane proteins” J. R. Soc. Interface, vol 11, May 2014, pp. 20140232, doi:10.1098/rsif.2014.0232.

[5] U.B. Sleytr, D. Pum, E.M. Egelseer, N. Ilk, B. Schuster. “S-Layer Proteins” in W. Knoll, Ed., Handbook of Biofunctional Surfaces, Pan Stanford Publishing, Singapore, chap. 14, pp. 507-568, 2014, ISBN: 978-981-4316-63-7.

[6] M.C. Dixon, “Quartz crystal microbalance with dissipation monitoring: Enabling real-time characterization of biological materials and their interactions” J. Biomolec. Techniques, vol. 19, Jul. 2008, pp. 151-158.

[7] R. Zucchi, and S. Ronca-Testoni, “The sarcoplasmic reticulum Ca^{2+} channel/ryanodine receptor: modulation by endogenous effectors, drugs and disease states” Pharmacol. Rev., vol. 49, Mar. 1997, pp. 1-51.

[8] R. Zalk, S.E. Lehnart, A.R. Marks “Modulation of the Ryanodine Receptor and Intracellular Calcium” Annu. Rev. Biochem., vol. 76, Jul. 2007, pp. 367-385, doi:10.1146/annurev.biochem.76.053105.094237

[9] B. Schuster, and U.B. Sleytr, “Nanotechnology with S-Layer Proteins” in J.A. Gerrard Ed., Protein Nanotechnology: Protocols, Instrumentation and Applications, 2nd Edn., Humana Press, Springer Science+Business Media, New York, vol. 996, chap. 9, pp. 153-175. 2013, doi:10.1007/978-1-62703-354-1, ISSN: 1064-3745, ISBN: 978-1-62703-354-1.

[10] A. Schrems et al. “Liposome Fusion on Proteinaceous S-layer Lattices Triggered via β-diketone ligand – Europium(III) Complex Formation” Soft Matter, vol. 7, May 2011, pp. 5514-5518, doi: 10.1039/c1sm05468f.

[11] M. Hohenegger, J. Suko, R. Gscheidlinger, H. Drobny, A. Zidar, “Nicotinic acid-adenine dinucleotide phosphate activates the skeletal muscle ryanodine receptor” Biochem. J., vol. 367, Okt. 2002, pp. 423-431, doi: 10.1042/BJ20020584.

[12] B. Schuster, and U.B. Sleytr, “Taylor-made crystalline structures of truncated S-layer proteins on heteropoly-saccharides” Soft Matter, vol. 5, Oct. 2009, pp. 334-341, doi:10.1039/b810211b

[13] E. Reimhult, F. Höök, B. Kasemo, “Intact vesicle adsorption and supported biomembrane formation from vesicles in solution: Influence of surface chemistry, vesicle size, temperature, and osmotic pressure” Langmuir, vol. 19, Mar. 2003, pp. 1681-1691, doi:10.1021/la0263920.

[14] M.R. Sharma, and T. Wagenknecht, “Cryo-electron microscopy and 3D reconstructions of ryanodine receptors and their interactions with EC coupling proteins” Basic Appl. Myol., vol. 14, pp. 299-306, 2004.

[15] A. Schrems et al. “The grab-and-drop protocol: a novel strategy for membrane protein isolation and reconstitution from single cells” Analyst, vol. 139, Jun. 2014, pp. 3296-3304, doi:10.1039/c4an00059e.

[16] H. Bayley, and P.S. Cremer, “Stochastic sensors inspired by biology” Nature, vol. 413, Sep. 2001, pp. 426-430.

 ISBN: 978-1-61208-380-3

The Influence of Ions in the Interaction of Methylene Blue with DPPC Membranes

Ronei Miotto, Guilherme G. Trellese, Rodrigo M. Cordeiro, and Elierge Costa

Centro de Ciências Naturais e Humanas
Universidade Federal do ABC
Santo André, SP, Brazil
Email: ronei.miotto@ufabc.edu.br

A. C. Ferraz

Instituto de Física
Universidade de São Paulo
São Paulo, SP, Brazil

Maurício S. Baptista

Instituto de Química
Universidade de São Paulo
São Paulo, SP, Brazil

***Abstract*—Methylene blue (MB) and its derivatives have applications as photosensitizers in photodynamic therapy. However, little is known about their interactions with phospholipid membranes at the molecular level. We employed molecular dynamics simulations to model the binding between MB and a dipalmitoyl phosphatidylcholine (DPPC) bilayer. This was done in the presence of molecular oxygen within the membrane. The abitily of MB to induce photodamage was inferred based on its immersion depth and degree of exposition to a higher oxygen concentration inside the membrane. In addition, the effect of the presence of ions in the solvent was explicitly considered.**

Keywords–methylene blue, lipid bilayer, molecular dynamics simulation

I. INTRODUCTION

Photosensitization is the basis of photodynamic therapy (PDT), a technique that has been used to treat various solid tumors in the skin, breast, lung, bladder, and esophagus [1]. The method relies on the administration of a sensitizer molecule that is able to induce the formation of reactive oxygen species (ROS), for example, singlet oxygen ($^1O_2$), when exposed to light of the appropriate wavelength [2]. ROS-mediated reactions in the cell membrane eventually lead to severe tissue damage since these species can act as powerful oxidizing agents, able to induce irreversible photodamage, necrosis or apoptosis, in tumor tissues [1].

The study of biological membranes involves the understanding of the influence of many different organelles and proteins. Model membranes, such as phospholipid bilayers, are often used in PDT studies. In particular, DPPC is the most abundant phospholipid in lung surfactant, primarily responsible for the reduction of surface tension to near 0 mN/m during expiration [3]. DPPC is zwitteronic having a negative charge on the phosphate group and a positive charge on the amine.

Methylene blue is a phenothiazinium dye with the following properties: strong absorbance in the range of 550–700 nm, significant quantum yield ($\phi_\Delta = 0.52$) [2], triplet with long intrinsic lifetime, low fluorescence quantum yield and lifetime, and low reduction potential [4]. Because of these characteristics, it has been used in a variety of photochemical applications including solar energy conversion [4] and PDT [5].

Localization of the sensitizer is a key issue in the understanding and determination of the PDT efficiency [1]. To facilitate drug development, it is often necessary to identify a target. A systematic study of structure-activity relationships can then aid in improving the therapeutic procedure. Our aim in this work was to explore the interaction between a model membrane (DPPC) and a photosensitizer (MB). In addition, the effect of the presence of ions in the solvent was investigated, since they might play a crucial role in determining the structural and electrostatic properties of model bilayers [6]. This allowed us to access the role of solvent ions in the interaction of MB with DPPC.

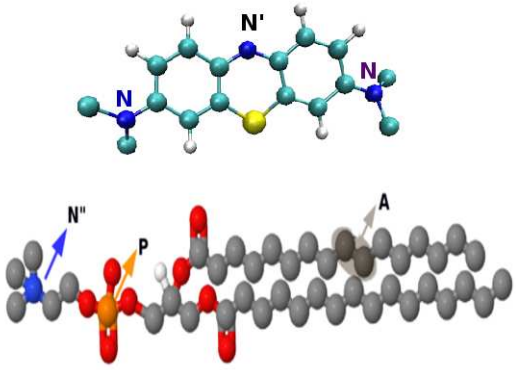

Figure 1. Schematic representation of methylene blue (MB) and DPPC indicating relevant regions and atoms.

This manuscript is organized as follows. In Section II, we briefly describe our theoretical approach. In Section III, our results for the interaction of MB and model DPPC membrane are discussed and compared to other works whenever posssible. Finally, a summary is presented in Section IV.

II. THEORETICAL MODELING

Molecular dynamics simulations were performed using the GROMACS 4.5.1 simulation package [7][8]. Molecular motions were computed by numerical integration of Newton's equations with a time step of 2 fs. Fully hydrated lipid bilayers made of DPPC were represented using the force field developed by Kukol [9]. The interaction parameters were based on the GROMOS53A6 force field [10], in which aliphatic carbon atoms and their adjacent hydrogens are treated as united atoms. Figure 1 shows the structure of methylene blue (MB) and DPPC indicating relevant atoms (N, N', N", and P) and regions (A). To simulate fully hydrated lipid bilayers, the SPC model [11] was used for water. A single oxygen molecule was added to the aqueous phase. The oxygen molecule dissolved

 ISBN: 978-1-61208-380-3

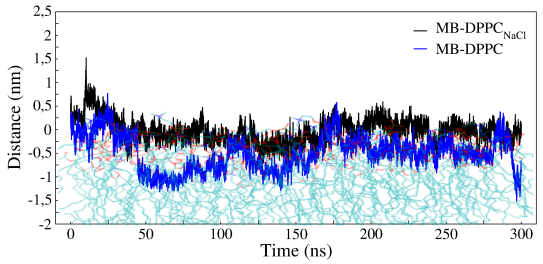

Figure 2. Temporal evolution of the drug-membrane binding process for MB. The top half of the lipid bilayer is also represented in the background.

in the membrane was described with parameters taken from the literature [12]. For compatibility, the methylene blue was assembled using the standard functional groups in the GROMOS53A6 force field [10]. The MB partial charges were taken from the density functional calculations performed using the Gaussian package [13].

Starting configurations for molecular dynamics were obtained from a pre-equilibrated membrane patch with 128 lipid molecules. Methylene blue was initially placed at the aqueous phase at a distance of ca. 3 nm from the bilayer surface. Only one MB molecule was added. A Cl^- ion was added to neutralize the system. In order to simulate systems at polar ionic strength, 27 Na^+ and 27 Cl^- ions are added to the aqueous phase. Overall, each simulated system had lateral dimensions of ca. 6.2 nm parallel to the membrane surface (xy-plane) and ca. 8.5 nm along the bilayer normal (z-axis). Periodic boundary conditions were applied in all Cartesian directions. The simulation protocol started with an equilibration run for 5.5 ns, during which the position of MB was kept restrained. The molecule was then released and molecular trajectories were recorded for 300 ns under controlled temperature (310 K) and pressure (1 atm).

The drug-membrane binding process was followed in time by recording both the position and the orientation of the different photosensitizers with respect to the bilayer. Density distributions of the membrane building blocks and the photosensitizer were calculated along the z axis. The degree of overlap between the distributions of photosensitizers and molecular oxygen was taken as an indicator of the expected $^1O_2$ generation efficiency. Further details of our theoretical modeling can be found in [14].

III. Results and Discussion

In the first step of our study, we have investigated the influence of ions in the MB-membrane binding process. Figure 2 shows the temporal evolution of the MB-membrane binding process. The immersion depth is defined as the distance between the center of mass of the photosensitizer and the water/bilayer interface. The top half of the lipid bilayer is also represented in the background. In both cases, MB started at the aqueous phase and reached the membrane surface within the first 2 or 3 ns, driven by favorable drug-membrane electrostatic interactions. As clearly seen in Figure 2, MB reaches a largest immersion depth, ∼0.5 to 0.8 nm, when ions were not considered, compared to ∼0.2 nm in the case they were included.

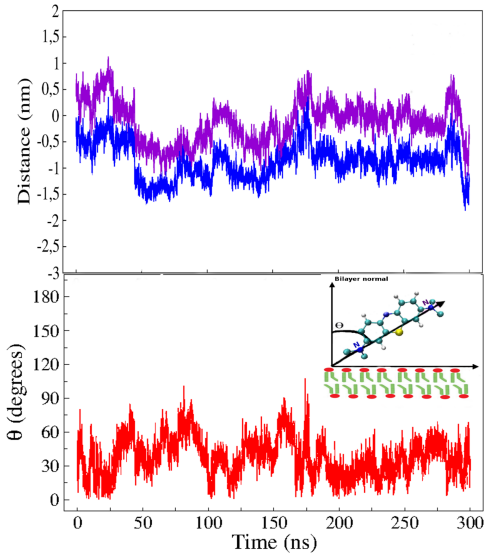

Figure 3. Upper panel: temporal evolution of the positions of the nitrogen atoms with respect to the bilayer/water interface, when ions are not considered. Lower panel: temporal evolution of the angle, θ, between the nitrogen atoms vector with respect to the membrane-water interface.

In order to access the orientation of MB when immersed on the DPPC bilayer, we analyze the relative positions of the the nitrogen atoms, indicated by N in Figure 1. In the upper panel of Figure 3 the temporal evolution of the positions of the nitrogen atoms with respect to the bilayer/water interface (when ions are not considered) is presented. These relative positions allowed us to extract the angle, θ, of the nitrogen atoms vector with respect to the membrane-water interface. The temporal evolution θ is shown in the lower panel of Figure 3. MB immersion occurs with the molecule forming an average angle close to 40° with the membrane-water interface, although a large fluctuation is observed. A similar average angle, ∼35°, is observed when ions are added to the water solution, as shown in Figure 4. However, in this case θ's fluctuation is much smaller. Together, Figures 2, 3, and 4 clearly show that, in the absence of ions, MB presents a higher mobility.

Next, we analyze the density profiles of different atoms or functional groups of MB and DDPC and the oxygen molecule, as shown in Figure 5, when ions are considered, and Figure 6, when ions are not taken into consideration. These density profiles give the spatial probability to find different molecules or functional groups along the bilayer normal. The density profiles for the phosphatidylcholine atoms N" and P and the functional group A are represented by dashed lines. In the insets, the black dashed lines represent the DPPC membranes in both cases.

For both systems, the nitrogen atoms of the AM molecule (N–N_{MB}) present a bimodal distribution (violet solid lines). The membrane surfaces were heuristically defined at the peaks of the phosphate group distribution, since the water density dropped from its bulk value to zero within the region occupied by this group. It is clear from Figure 5 that, in the presence of ions, the methylene blue molecule immersion is in such a way that the one of the symmetric nitrogen atom is in the region

 ISBN: 978-1-61208-380-3

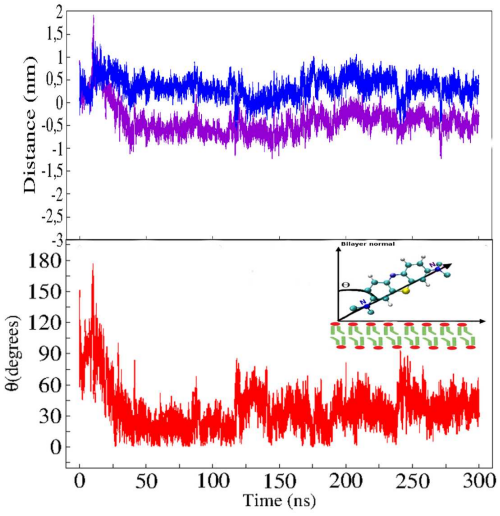

Figure 4. Upper panel: temporal evolution of the positions of the nitrogen atoms with respect to the bilayer/water interface, when ions are considered. Lower panel: temporal evolution of the angle, θ, between the nitrogen atoms vector with respect to the membrane-water interface.

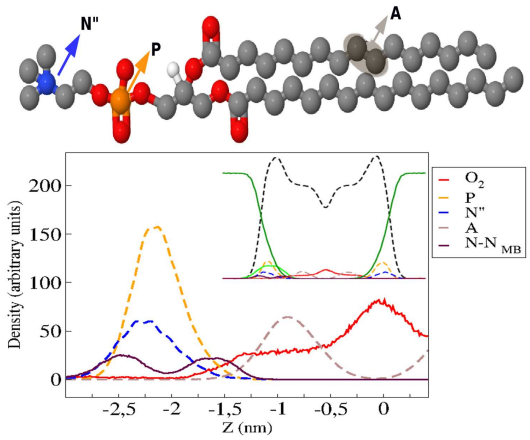

Figure 5. Density profiles, i.e. spatial probability to find different molecules or functional groups along the bilayer normal when ions are considered. Density profiles were arbitrary scaled in order to allow a better visualization.

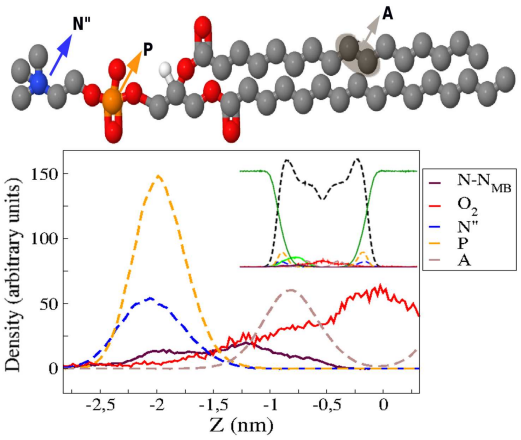

Figure 6. Density profiles, i.e. spatial probability to find different molecules or functional groups along the bilayer normal when ions are not considered. Density profiles were arbitrary scaled in order to allow a better visualization.

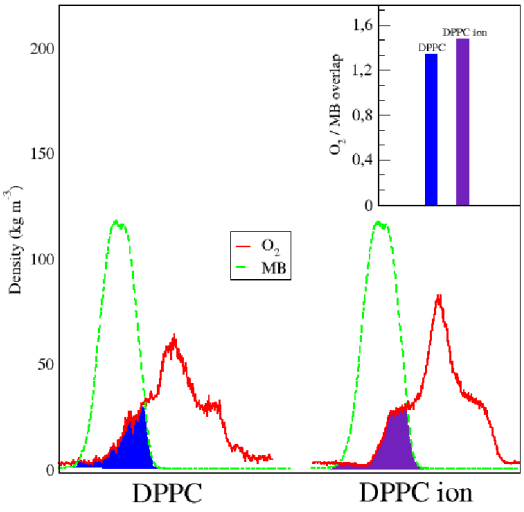

Figure 7. MB and the oxygen molecule distribution along the z axis when ions are explicitly considered in the solvent (left) or not (right). In the inset, the integral overlap between the density profiles of MB (ρ_{MB}) and of molecular oxygen (ρ_{O_2}) along the z axis for both systems are compared.

of the phospholipid head group, indicated by P. When ions are not included, as depicted in Figure 6, the MB molecule immersion is such that the nitrogen atom is closer to the A region, around the region where C=O bonds can be found.

The density profiles in Figures 5 and 6 predict an increased oxygen concentration in the membrane interior as compared with the aqueous phase. Figure 7 shows how MB and the oxygen molecules are distributed along the bilayer normal when ions are present in the solvent (right) or not (left). The probability of electron/energy transfer via type I mechanism can be estimated, in a simple but effective way [14], in terms of the integral overlap between the density profiles of MB (ρ_{MB}) and of molecular oxygen (ρ_{O_2}) along the z axis. This probability can be obtained as

$$P_{O_2/MB} \propto \int dz \rho_{MB}(z) \bullet \rho_{O_2}(z) \qquad (1)$$

where the integral runs over the entire system length along the z axis. A direct correlation can not be assumed between photodynamic efficiency and the probability of ROS generation since the membrane binding might be influenced by the presence of ions in the solvent. The integral overlap O_2/MB is indicated in the inset of Figure 7. Since the calculated values for both cases are very close, we believe that the relative photodynamic efficiency is probably defined by differences in membrane binding.

In Photodynamic Therapy (PDT), an excited photosensitizer can undergo type I (electron transfer) and/or type II (energy transfer) reactions to produce highly reactive oxygen species (ROS), resulting in necrosis and/or apoptosis of exposed cells [1]. Type I reactions generate radical and radical anion species (e.g., O_2^-, HO^-), while type II reactions produce singlet oxygen ($^1O_2$) by energy transfer between a photosensitizer in its excited state and an oxygen molecule.

 ISBN: 978-1-61208-380-3

In this later case, membrane damage results from the tendency of $^1O_2$ to add to hydrocarbon double bonds, forming hydroperoxides. Since DPPC is a saturated lipid, the formation of hydroperoxides via a Type I mechanism is not possible. However, it is already well stablished [15] that eukaryotic cell membranes contain mixtures of glycerolipids (in mammalina cells, all phospholipids except sphingomyelin), sphyngolipids, and sterols. As a consequence, DPPC can be found in cell membranes with different unsaturated lipids. Photodynamic damage is believed to occur in the close vicinity of the sensitizer because teh main cytotoxic product, singlet oxygen, has a short life time. Therefore, it is fair to say that when MB is incorporated in a DPPC domain, the photodamage in vicinal unsaturated lipids might occur. Following this argument, it is possible to infer that the photodamage might occur in the head group region, when ions are included, or close to the hydrophobic region, when ions are not considered.

By unveiling the interaction of DPPC with AM at a molecular level, we are contributing for a better knowledge of structure-activity relationships of such systems. We believe that this will help in improving the the use of AM as a PDT agent.

IV. Conclusions

In this work, molecular dynamics simulations were employed to examine the interactions between MB and DPPC bilayer at a molecular level when ions are present in the solvent or not. We found that the immersion depth of MB is higher in the absence of ions, but the molecule orientation is the same in both cases: MB is slightly tilted. Our data also suggests that MB mobility is also higher when ions are not present. With ions in the solvent, the methylene blue molecule immersion is in such a way that it is placed between the phospholipid head group and the C=O bond region. When ions are not considered, the MB molecule immersion is higher in such way that electron/energy transfer mechanisms might also take place in the hydrophobic region of the DPPC bilayer. In addition, the probability of energy/electron transfer is estimated and found to be very similar whith or without the presence of ions.

Acknowledgements

The authors acknowledge financial support from CNPq and FAPESP (project 2012/50680-5).

References

[1] T. J. Dougherty, C. J. Gomer, B. W. Henderson, G. Jori, D. Kessel, M. Korbelik, J. Moan, and Q. Peng, "Photodynamic Therapy," JNCI Journal of the National Cancer Institute, vol. 90, no. 12, Jun. 1998, pp. 889–905. [Online]. Available: http://jnci.oxfordjournals.org/cgi/doi/10.1093/jnci/90.12.889

[2] M. DeRosa, "Photosensitized singlet oxygen and its applications," Coordination Chemistry Reviews, vol. 233-234, Nov. 2002, pp. 351–371. [Online]. Available: http://linkinghub.elsevier.com/retrieve/pii/S0010854502000346

[3] A. Kaviratna and R. Banerjee, "The effect of acids on dipalmitoyl phosphatidylcholine (DPPC) monolayers and liposomes," Colloids and Surfaces A: Physicochemical and Engineering Aspects, vol. 345, no. 1-3, Aug. 2009, pp. 155–162. [Online]. Available: http://linkinghub.elsevier.com/retrieve/pii/S0927775709002799

[4] D. Severino, H. C. Junqueira, M. Gugliotti, D. S. Gabrielli, and M. S. Baptista, "Influence of negatively charged interfaces on the ground and excited state properties of methylene blue." Photochemistry and photobiology, vol. 77, no. 5, May 2003, pp. 459–68. [Online]. Available: http://www.ncbi.nlm.nih.gov/pubmed/12812286

[5] J. A. P. Tardivo, A. Del Giglio, L. H. Paschoal, and M. S. Baptista, "New photodynamic therapy protocol to treat AIDS-related Kaposi's sarcoma." Photomedicine and laser surgery, vol. 24, no. 4, Aug. 2006, pp. 528–31. [Online]. Available: http://www.ncbi.nlm.nih.gov/pubmed/16942436

[6] S. A. Pandit and M. L. Berkowitz, "Molecular dynamics simulation of dipalmitoylphosphatidylserine bilayer with Na+ counterions." Biophysical journal, vol. 82, no. 4, Apr. 2002, pp. 1818–27. [Online]. Available: http://www.pubmedcentral.nih.gov/articlerender.fcgi?artid=1301979&tool=pmcentrez

[7] B. Hess, C. Kutzner, D. van der Spoel, and E. Lindahl, "GROMACS 4: Algorithms for Highly Efficient, Load-Balanced, and Scalable Molecular Simulation," Journal of Chemical Theory and Computation, vol. 4, no. 3, Mar. 2008, pp. 435–447. [Online]. Available: http://pubs.acs.org/doi/abs/10.1021/ct700301q

[8] D. Van Der Spoel, E. Lindahl, B. Hess, G. Groenhof, A. E. Mark, and H. J. C. Berendsen, "GROMACS: fast, flexible, and free." Journal of computational chemistry, vol. 26, no. 16, Dec. 2005, pp. 1701–18. [Online]. Available: http://www.ncbi.nlm.nih.gov/pubmed/16211538

[9] A. Kukol, "Lipid Models for United-Atom Molecular Dynamics Simulations of Proteins," Journal of Chemical Theory and Computation, vol. 5, no. 3, Mar. 2009, pp. 615–626. [Online]. Available: http://pubs.acs.org/doi/abs/10.1021/ct8003468

[10] C. Oostenbrink, A. Villa, A. E. Mark, and W. F. van Gunsteren, "A biomolecular force field based on the free enthalpy of hydration and solvation: the GROMOS force-field parameter sets 53A5 and 53A6." Journal of computational chemistry, vol. 25, no. 13, Oct. 2004, pp. 1656–76. [Online]. Available: http://www.ncbi.nlm.nih.gov/pubmed/15264259

[11] H. J. C. Berendsen, J. P. M. Postma, W. F. van Gunsteren, and J. Hermans, "Interaction Models for Water in Relation to Protein Hydration," in Intermolecular Forces. Amsterdan: Springer Netherlands, 1981, pp. 331–342. [Online]. Available: http://link.springer.com/chapter/10.1007%2F978-94-015-7658-1_21

[12] J. Fischer and S. Lago, "Thermodynamic perturbation theory for molecular liquid mixtures," The Journal of Chemical Physics, vol. 78, no. 9, 1983, p. 5750. [Online]. Available: http://scitation.aip.org/content/aip/journal/jcp/78/9/10.1063/1.445458

[13] M. J. Frisch, et al., "Gaussian 09, Revision D.01," Wallingford CT, 2009. [Online]. Available: http://www.gaussian.com/

[14] R. M. Cordeiro, R. Miotto, and M. S. Baptista, "Photodynamic efficiency of cationic meso-porphyrins at lipid bilayers: insights from molecular dynamics simulations." The Journal of Physical Chemistry B, vol. 116, no. 50, Dec. 2012, pp. 14 618–27. [Online]. Available: http://www.ncbi.nlm.nih.gov/pubmed/23163841

[15] D. Brown and E. London, "Structure and Origin of Ordered Lipid Domains in Biological Membranes," Journal of Membrane Biology, vol. 164, no. 2, Jul. 1998, pp. 103–114. [Online]. Available: http://link.springer.com/10.1007/s002329900397

 ISBN: 978-1-61208-380-3

Structure of Feed-Forward Realizations with Enzymatic Processes

Evgeny Katz and Vladimir Privman

Department of Chemistry and Biomolecular Science, and
Department of Physics, Clarkson University,
Potsdam, NY 13699, USA
privman@clarkson.edu

Oleksandr Zavalov

Department of Physics, St. Francis Xavier University,
Antigonish, NS, B2G 2W5, Canada

Abstract — **Basic bio-inspired information-processing motifs, such as feed forward can be useful in complex biochemical networks for signal processing and biosensing. We propose an experimental design and a numerical approach to a synthetic enzyme cascade-based biochemical system for feed-forward loop implementation that demonstrates an ability to delay and stabilize the changes in the output signal in response to chaotic fluctuations in the input signal.**

Keywords *— Feed-forward loop; enzymatic processes.*

I. INTRODUCTION

Information processing with networked biomolecular reactions, termed "biocomputing" [1][2], is a type of unconventional computing [3] that offers interesting new applications for multi-input biosensing [4]-[6] and generally complex signal processing [7][8] without involving electronics at each step. Most experimental efforts aimed to implementing biocomputing utilize the analog/digital approach because it is fully understood and has fault-tolerant scalability. This approach has been successfully applied to many enzyme-based systems offering a selection of binary logic gates [9]-[12]. Small biochemical networks have also been explored, utilizing concatenated enzymatic reactions to carry out Boolean functions [1][2][13]-[15].

However, biomolecular processes also offer tools for considering new unconventional network elements and architectures that are bio-inspired but are vastly simpler than those in nature. Indeed, recent research has involved consideration of non-binary network elements for improving noise handling of binary steps, and also utilization of several bio-inspired memory elements (memristors, etc.) for designs of electronic circuitry for specific applications [16][17]. The former development [2][18]-[27] allowed to incorporate biochemical "filtering" in biocatalytic reactions and reaction cascades, leading to a considerable reduction of the noise transmission factor. The resulting output response as a function of the input was transformed to sigmoid shape [2][18][19][21].

Realization of such synthetic biochemical systems in the framework of biocomputing [1][2][28]-[30] has enabled their implementation in practical applications, primarily in biosensing. The availability of biomolecular "building blocks" offers a toolbox of processes to experiment with optimization of networking involved in signal processing with biomolecular reaction cascades [1][21].

Several research groups have studied biocomputing, using synthetic deoxyribonucleic acid (DNA) chains (oligonucleotides) [31][32], various proteins (including enzymes) [12][14][18]-[21][33]-[36], and other bio-objects [10][37][38] (even whole cells). Compatibility of enzymes with physiological processes and electronics has favored their use in biocomputing designs aimed at near-term applications. Enzyme reactions are also particularly suitable for interfacing with electronics [39][40] in electrochemical settings. Therefore, even small networks with several enzymatic steps offer applications [41], e.g., for biosensing [4]-[6][31][32], for the point-of-care [33][34] and security purposes [35][36].

Information processing in nature is another successful approach, quite different from the analog/digital paradigm. Systems biology studies aspects of nature's information processing [8][37]-[39]. Bio-inspired approaches have resulted in interesting research involving memory, learning, etc. Some of the considered "network elements" enable novel electronic circuit designs [16][17] and suggest novel biocomputing approaches [40][41].

Here, we review recent ideas [42] and report new results on enzymatic-process realizations of feed-forward loops which are the most common network motifs in nature's information processing [8][42]-[46]. Specifically, feed-forward loops are abundant as signal processing steps in cellular processes ranging from regulatory mechanisms [47] to cell differentiation [48]. The functionality of feed-forward loops and other complicated network motifs is largely determined by the connectivity of the various network components including biochemical processes [43][49][50]. The study of the feed-forward dynamics usually focuses on

 ISBN: 978-1-61208-380-3

specific network architectures of interest [45][50][51]. Such research is typically devoted to modeling of the temporal or spatial features of constituent processes [43]-[45][50][51], and to their networking [45][52][53].

There are several types of feed-forward loops. The most common examples of the feed-forward loop network motif are the coherent and incoherent feed-forward loops [8], that have been extensively studied theoretically [43][44][54]. More complicated "topologies" have also been considered [49][50], with different types of activation [44][51]. However, only limited experimental realizations are known to date for feed-forward loops as synthetic biochemical processes, specifically, with DNA [55].

Modeling allows exploration of the potential future incorporation of bio-inspired network elements into biochemical circuits [8][42][56][57], for instance, for biocomputing [52][58][59]. Numerical approaches include biochemical systems theory [60], kinetic modeling [42][43], Gaussian models [49], cellular automata simulation [50], etc.

In Section II we discuss possible realizations of feed-forward biochemical system. Section III is devoted to proposed experimental design and numerical approach to the synthetic biochemical system with enzyme-catalyzed biochemical reactions that demonstrate feed-forward response. In Section IV offers a concluding discussion.

II. DISCUSSION OF THE FEED-FORWARD REALIZATION

In this work, we propose a realization of feed-forward systems with few coupled enzymatic reactions [42], which, if realized, will be a much simpler implementation than those in nature. Let us discuss an example of a possible design and offer a general introduction. The details of the actual biochemistry of this and other systems are explained in [42]. Unlike the various earlier-realized biocomputing gates, feed forward in most cases is not functioning as a binary gate [60]-[63]. We expect that the considered designs [42] will initiate research into synthetic information processing setups not aimed at "artificial life" [64]-[66], but rather at a more limited and hopefully more tractable task of mimicking the nature's information processing.

The challenge of attempting enzyme-process realizations of the feed-forward loop is that it has two "signal transduction" steps (see the scheme in Figure 1), each involving the input signal, X, usually not being directly converted into the output Z. Instead, in the primary (direct) step, X acts as the activator (promoter), denoted by →, or repressor (inhibitor), denoted by ⊣, of ongoing processes that generate the output signal, Z. The secondary (indirect) pathway in the loop consists of the input X affecting (activating or repressing) the processes that produce another, intermediate signal, Y. This intermediate signal, Y, in turn activates or represses the ongoing processes of the production of the output, Z. In Figure 1, two enzyme-catalyzed biochemical processes (shown in boxes) constantly produce chemicals that are signals Y and Z.

For biochemical realizations, we will consider the simplest situation when *X or Y*, rather than *X and Y* together activate the output signal, Z, production. The latter is another feed-forward option. In the simplest classification [44][62], there are 8 different loop types:

$$X \rightarrow Z \text{ or } X \dashv Z, \quad X \rightarrow Y \text{ or } X \dashv Y, \quad Y \rightarrow Z \text{ or } Y \dashv Z. \qquad (1)$$

The feed-forward loop is "coherent" or "incoherent" depending on whether the net effect of X on the production of Z in the secondary pathway is the same as in the primary. The most common feed-forward loops in nature involve three activations [44][47][48].

We present a potential realization of such a process [42] with enzymatic reactions in Figure 1. Such systems require at least two biochemical processes that generate signals Y and Z. The chemical reaction rates of these processes are then controlled by the input at time t, $X(t)$. Here chemical input signal X activates (promotes) the production of both Z and Y, whereas Y promotes the production of Z.

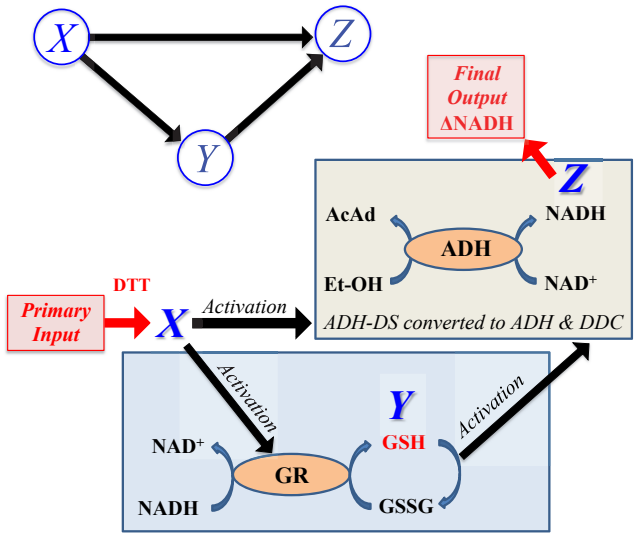

Fig. 1. Feed-forward loop with *activation* in all the signal transduction steps. The top scheme shows the activations involved. The biochemical processes are explained in Section III, with additional details founds in [42].

In some situations, activation can be made rather sharp as a function of parameters, and inhibition can also be made sharp. Then, the feed-forward loop can approximate binary logic gates [67]. However, generally feed forward is not binary. Its primary network function, specifically with three promotions (Figure 1), is to provide a stabilizing role.

Indeed, feed-forward loop as a network element has the capability to delay the changes in the output signal, $Z(t)$, in response to erratic fluctuations and fast variations in the environmental input signal, $X(t)$ [42][45][47][51][52]. This frequently enables threshold behavior [8][44], whereby the response begins and/or stops only when one or several of the chemical concentrations cross (up or down) activation thresholds. Otherwise, the system does not respond to input signal variations. This property avoids waste of resources in

 ISBN: 978-1-61208-380-3

natural-pathway responses. The secondary pathway provides the postponing of the effect of changes in the input signal, X, in its net impact on Z. The system's response can then also have its own response time scale(s) [44][68]-[70].

In an experimental realization, we have to control the availability of the input chemical, $X(t)$, inputting or deactivating this compound by physical or (bio)chemical methods, at the rate, R_{ext}, that can be negative or positive,

$$\frac{dx}{dt} = R_{ext}(t) + \text{reaction terms}, \qquad (2)$$

where the "reaction terms" describe the kinetics of a possible consumption of X by the biochemical processes of the feed-forward loop itself. The quantification of the feed-forward effect will consist of detecting how the response time dependence of $Z(t)$ is affected by the presence of the secondary transduction step, $X \rightarrow Y \rightarrow Z$. This pathway can be enabled at various degrees of activity.

The stabilizing effects expected of feed-forward functions have never been realized in simple "synthetic" enzymatic systems. Here, we highlight the challenges involved in such realizations, see [42]. Ref. [42] also offers an example of an enzymatic system with all the transductions being repression, ⊣, steps.

III. DESIGN AND MODELLING

Let us outline the principles of feed-forward design [42] based on enzymatic cascades. Specifically, consider the system shown in Figure 1. This cascade includes the functioning of two enzymes with activations in all steps: Glutathione reductase (GR), which biocatalytically converts glutathione from its oxidized form, Glutathione disulfide (GSSG), to the reduced form, Glutathione (GSH). Then, GSH, acts as the intermediate signal, Y, in the feed-forward functioning. In parallel, β-nicotinamide adenine dinucleotide is converted from its reduced form, NADH, to the oxidized form, NAD^+. Alcohol dehydrogenase (ADH), biocatalytically oxidizes ethanol (Et-OH) to yield acetaldehyde (AcAd), while β-nicotinamide adenine dinucleotide is converted from its oxidized form, NAD^+, to the reduced state NADH. These processes can yield the increase in the amount of NADH that can be measured optically by changes in absorption. Thus, as expected for feed forward, signals Z and Y are generated continuously once the reactions are started. In fact, the rate of production of NADH must be kept in check, to avoid rapid build-up of signal Z: The excess concentration of NADH,

$$\Delta\text{NADH}(t) = \text{NADH}(t) - \text{NADH}(0), \qquad (3)$$

is the measured output signal, $Z(t)$. The names of the additional chemical compounds in Figure 1, are abbreviated as follows: dithiothreitol (DTT), diethyldithiocarbamate (DDC), disulfiram (DS), and their role is detailed in [42].

The full realization and characterization of the proposed enzymatic cascade will require addressing several challenges, even though some of the processes have already been studied in the literature. Possible experimental realizations and preliminary tests are described in [42].

Generally, the structure of enzymatic feed-forward realizations is shown in Figure 2. We will next discuss a kinetic modelling approach to such systems. In modelling of feed-forward loops, one can set up coupled rate equations [42] describing signal and other compound variations. This approach can yield the expected features, including the delayed response of the output to the input's variations/fluctuations, and other properties. For enzymes, the resulting systems of equations will be more complicated and contain different terms than those considered in purely phenomenological formulations [7][62].

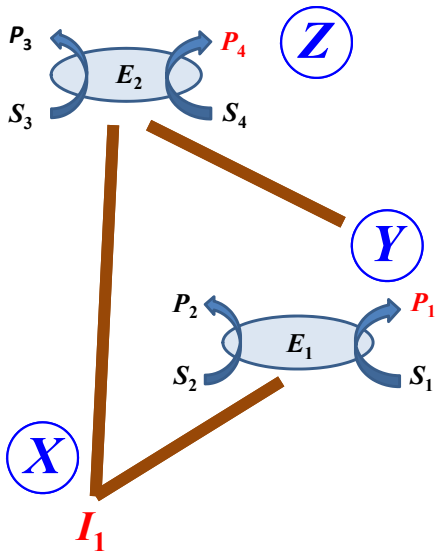

Fig. 2. Principle of an enzymatic-cascade feed-forward design in terms of the constituent enzymatic processes. Activations or repressions (promotions or inhibitions) are shown by brown lines.

We use the standard Michaelis-Menten type model, which focuses on the dominant enzyme bio-catalysis mechanism. The first enzyme, E_1, binds a substrate, S_1, to produce a complex, C. This complex can either on its own or by binding another substrate, S_2, produces the product(s) $P_{1,2}$ (Figure 2), restoring the enzyme to its original form. In the chemical reaction notation, we have,

$$S_1 + E_1 \underset{k_{-1}}{\overset{k_1}{\rightleftarrows}} C, \quad S_2 + C \xrightarrow{k_2} E_1 + P_1 + P_2. \qquad (4)$$

The second step can usually be assumed irreversible, but the first one requires two rate constants. These process parameters, here $k_{\pm 1}$, k_2, are generally not known individually and have to be fitted from experiments.

 ISBN: 978-1-61208-380-3

Activation/repression can involve several mechanisms, one of which can be a complex formation, for example,

$$I_1 + E_1 \underset{r_{-1}}{\overset{r_1}{\rightleftarrows}} \overline{E_1} + W. \quad (5)$$

Here, the "complex" is the modified enzyme $\overline{E_1}$ with a different activity, with larger or smaller rate constants, $\overline{k_{\pm 1}}$, $\overline{k_2}$ in processes similar to those in Equation (4), and it can be restored to the original form, E_1, for example by reacting with some other chemical, here denoted W. If, for instance, I_1 is our input, X, then the added "reaction terms" in Equation (2) enter via such chemical processes,

$$\frac{dI_1}{dt} = R_{ext}(t) - r_1 I_1(t) E_1(t) + r_{-1} W(t)\, \overline{E_1}\,(t), \quad (6)$$

whereas the time-dependence of the quantities entering here is in turn set by their own rate equations, for example,

$$\frac{dE_1}{dt} = -\, r_1 I_1 E_1 + r_{-1} W \overline{E_1} - k_1 S_1 E_1 + k_{-1} C, \quad (7)$$

etc. Note that in the next stage, when writing the rate equation for S_1, for instance, terms resulting from its reaction with both the original and modified enzymes will enter, with their respective rates,

$$\frac{dS_1}{dt} = -\, k_1 S_1 E_1 + k_{-1} C - \overline{k_1} S_1 \overline{E_1} + \overline{k_{-1}} \bar{C}. \quad (8)$$

Even within this relatively simple chemical kinetics description, enzymatic cascades lead to systems of numerous chemical rate equations, with parameters that depend on the physical and chemical conditions of the experiment, and that are documented only to a very limited extent; typically, at most a single parameter, calculated in our notation from the quantities $k_{\pm 1}$ and $S_2(0)k_2$, call the Michaelis-Menten constant, is tabulated.

Attempts can be made to consider much more simple enzymatic feed-forward realizations. Let us consider the cascade sketched in Figure 3, where X is one of the substrates for enzyme E_1, but also for enzyme E_2. The former enzyme outputs Z as one of its products, whereas the latter outputs Y. However, Y is a substrate for enzyme E_3, which also outputs Z. Such systems are easier to design for experimental realizations because they involve process cascades of the type already realized in the binary-biocomputing-gate research [1][2]. The "activation" by X and by Y consists of them simply being the actual inputs enabling the reactions. The availability of the primary input substrate, $X(t)$, was controlled by adjusting $R_{ext}(t)$, to yield the shown time dependence.

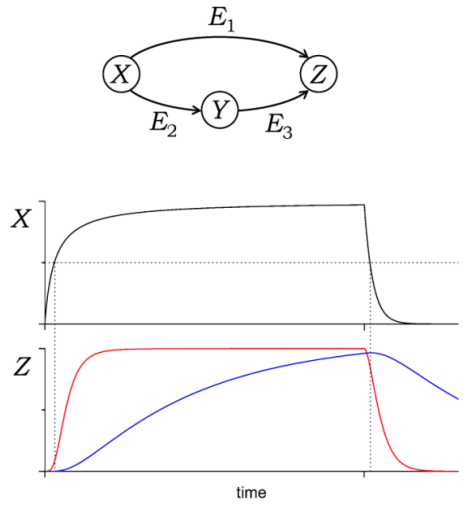

Fig. 3. The top scheme shows a three-enzyme system, which was numerically modelled as a candidate for a simplified all-activations feed forward. Our modelling results indicate that a limited feed-forward-type delayed response is possible, as illustrated by the blue curve.

In this model, adjustable quantities (concentrations of those chemicals that are not designated as input/output signals) can be selected as needed to achieve variants of delayed response, Figure 3, to various protocols, $R_{ext}(t)$, of controlling the input signal availability. However, this simplified approach cannot provide the full-featured feed-forward realization even for the all-activations case. More complicated cascades [42], such as that shown in Figure 1, will have to be explored in future work.

IV. CONCLUSION

We surveyed the conceptual design for cascades of enzyme-catalyzed biochemical reactions that promise realizations of the feed-forward response. This design of synthetic biochemical system with few coupled enzymatic reactions demonstrated the activation in all the signal transduction steps with a capability to delay the changes in the output signal. Such enzymatic-process realization of feed-forward loops is expected to have a stabilizing effect in the response to chaotic fluctuations in the input signals.

ACKNOWLEDGEMENT

Funding by the NSF (grants CBET-1066397 and CBET-1403208) is gratefully acknowledged. We wish to thank K. Clark, J. Halámek, and V. Bocharova for helpful input and discussions.

 ISBN: 978-1-61208-380-3

REFERENCES

[1] V. Privman, O. Zavalov, L. Halámková, F. Moseley, J. Halámek, and E. Katz, "Networked Enzymatic Logic Gates with Filtering: New Theoretical Modeling Expressions and Their Experimental Application," J. Phys. Chem. B 2013, vol. 117, pp. 14928–14939.

[2] V. Privman, B. E. Fratto, O. Zavalov, J. Halámek, and E. Katz, "Enzymatic AND Logic Gate with Sigmoid Response Induced by Photochemically Controlled Oxidation of the Output," J. Phys. Chem. B 2013, vol. 117, pp. 7559–7568.

[3] A. Adamatzky, L. Bull, B. De Lacy Costello, S. Stepney, and C. Teuscher (eds.), Unconventional Computing 2007, Luniver Press, Bristol, UK, 2007.

[4] J. Wang and E. Katz, "Digital Biosensors with Built-in Logic for Biomedical Applications – Biosensors Based on Biocomputing Concept," Anal. Bioanal. Chem. 2010, vol. 398, pp. 1591–1603.

[5] J. Wang and E. Katz, "Digital Biosensors with Built-in Logic for Biomedical Applications," Israel J. Chem. 2011, vol. 51, pp. 141–150.

[6] V. Privman, O. Zavalov, and A. Simonian, "Extended Linear Response for Bioanalytical Applications Using Multiple Enzymes," Anal. Chem. 2013, vol. 85, pp. 2027–2031.

[7] D. D. Seaton and J. Krishnan, "Effects of Multiple Enzyme-Substrate Interactions in Basic Units of Cellular Signal Processing," Phys. Biol. 2012, vol. 9, Article #045009.

[8] U. Alon, An Introduction to Systems Biology. Design Principles of Biological Circuits, Chapman & Hall/CRC Press, 2007.

[9] J. Halámek, et al., "Realization and Properties of Biochemical-Computing Biocatalytic XOR Gate Based on Enzyme Inhibition by a Substrate," J. Phys. Chem. B 2011, vol. 115, pp. 9838–9845.

[10] M. N. Stojanovic, T. E. Mitchell, and D. Stefanovic, "Deoxyribozyme-Based Logic Gates," J. Am. Chem. Soc. 2002, vol. 124, pp. 3555–3561.

[11] E. Gdor, E. Katz, and D. Mandler, "Biomolecular AND Logic Gate Based on Immobilized Enzymes with Precise Spatial Separation Controlled by Electrochemical Scanning Microscopy," J. Phys. Chem. B 2013, vol. 117, pp. 16058–16065.

[12] T. Miyamoto, S. Razavi, R. DeRose, and T. Inoue, "Synthesizing Biomolecule-Based Boolean Logic Gates," ACS Synthetic Biology 2013, vol. 2, pp. 72–82.

[13] M. Kahan, B. Gil, R. Adar, and E. Shapiro, "Towards Molecular Computers that Operate in a Biological Environment," Physica D 2008, vol. 237, pp. 1165–1172.

[14] G. Ashkenasy and M. R. Ghadiri, "Boolean Logic Functions of a Synthetic Peptide Network," J. Am. Chem. Soc. 2004, vol. 126, pp. 11140–11141.

[15] E. Katz, "Biomolecular Information Processing: From Boolean Logic Gates to Complex Networked Systems," Int. J. Unconventional Computing 2012, vol. 8, pp. 339–346.

[16] M. Di Ventra and Y. V. Pershin, "The Parallel Approach," Nature Phys. 2013, vol. 9, pp. 200–202.

[17] Y. V. Pershin and M. Di Ventra, "Solving Mazes with Memristors: A Massively Parallel Approach," Phys. Rev. E 2011, vol. 84, Article #046703.

[18] J. Halámek, O. Zavalov, L. Halámková, S. Korkmaz, V. Privman, and E. Katz, "Enzyme-Based Logic Analysis of Biomarkers at Physiological Concentrations: AND Gate with Double-Sigmoid "Filter" Response," J. Phys. Chem. B 2012, vol. 116, pp. 4457–4464.

[19] O. Zavalov, V. Bocharova, V. Privman, and E. Katz, "Enzyme-Based Logic: OR Gate with Double-Sigmoid Filter Response," J. Phys. Chem. B 2012, vol. 116, pp. 9683–9689.

[20] O. Zavalov, et al., "Two-Input Enzymatic Logic Gates Made Sigmoid by Modifications of the Biocatalytic Reaction Cascades," Int. J. Unconv. Comput. 2012, vol. 8, pp. 347–365.

[21] S. Bakshi, O. Zavalov, J. Halámek, V. Privman, and E. Katz, "Modularity of Biochemical Filtering for Inducing Sigmoid Response in Both Inputs in an Enzymatic AND Gate," J. Phys. Chem. B 2013, vol. 117, pp. 9857−9865.

[22] J. Halámek, et al., "Biomolecular Filters for Improved Separation of Output Signals in Enzyme Logic Systems Applied to Biomedical Analysis," Anal. Chem. 2011, vol. 83, pp. 8383–8386.

[23] M. Pita, et al., "Towards Biochemical Filter with Sigmoidal Response to pH Changes: Buffered Biocatalytic Signal Transduction," Phys. Chem. Chem. Phys. 2011, vol. 13, pp. 4507–4513.

[24] V. Privman, et al., "Biochemical Filter with Sigmoidal Response: Increasing the Complexity of Biomolecular Logic," J. Phys. Chem. B 2010, vol. 114, pp. 14103–14109.

[25] S. P. Rafael, et al., "Employing the Metabolic "Branch Point Effect" to Generate an All-or-None, Digital-Like Response in Enzymatic Outputs and Enzyme-Based Sensors," Anal. Chem. 2012, vol. 84, pp. 1076–1082.

[26] A. Vallée-Bélisle, F. Ricci, and K. W. Plaxco, "Engineering Biosensors with Extended, Narrowed, or Arbitrarily Edited Dynamic Range," J. Am. Chem. Soc. 2012, vol. 134, pp. 2876−2879.

[27] D. Kang, A. Vallée-Bélisle, K. W. Plaxco, and F. Ricci, "Re-engineering Electrochemical Biosensors to Narrow or Extend Their Useful Dynamic Range," Angew. Chem. Int. Ed. 2012, vol. 51, pp. 6717–6721.

[28] E. Katz and V. Privman, "Enzyme-Based Logic Systems for Information Processing," Chem. Soc. Rev. 2010, vol. 39, pp. 1835–1857.

[29] V. Privman, M. A. Arugula, J. Halámek, M. Pita, and E. Katz, "Network Analysis of Biochemical Logic for Noise Reduction and Stability: A system of Three Coupled Enzymatic AND Gates," J. Phys. Chem. B 2009, vol. 113, pp. 5301–5310.

[30] S. Mailloux, O. Zavalov, N. Guz, E. Katz, and V. Bocharova, "Enzymatic Filter for Improved Separation of Output Signals in Enzyme Logic Systems towards 'Sense and Treat' Medicine," Biomaterials Science 2014, vol. 2, 184–191.

[31] R. Pei, E. Matamoros, M. Liu, D. Stefanovic, and M. N. Stojanovic, "Training a Molecular Automaton to Play a Game," Nature Nanotechnol. 2010, vol. 5, pp. 773–777.

[32] M. N. Stojanovic and D. Stefanovic, "Chemistry at a Higher Level of Abstraction," J. Comput. Theor. Nanosci. 2011, vol. 8, pp. 434–440.

[33] V. Privman, "Biomolecular Computing: Learning Through Play," Nature Nanotechnology 2010, vol. 5, pp. 767–768.

[34] Y. Benenson, "Biomolecular Computing Systems: Principles, Progress and Potential," Nature Rev. Genetics 2012, vol. 13, pp. 455–468.

[35] E. Katz (ed.), Biomolecular Information Processing – From Logic Systems to Smart Sensors and Actuators, Willey-VCH, Weinheim, 2012.

[36] R. Unger and J. Moult, "Towards Computing with Proteins," Proteins 2006, vol. 63, pp. 53–64.

[37] Y. Benenson, "RNA-Based Computation in Live Cells," Curr. Opin. Biotechnol. 2009, vol. 20, pp. 471–478.

[38] M. L. Simpson, G. S. Sayler, J. T. Fleming, and B. Applegate, "Whole-Cell Biocomputing," Trends Biotechnol. 2001, vol. 19, pp. 317–323.

[39] E. Katz, V. Bocharova, and M. Privman, "Electronic Interfaces Switchable by Logically Processed Multiple Biochemical and Physiological Signals," (Highlight Article). J. Mater. Chem. 2012, vol. 22, pp. 8171–8178.

[40] A. Poghossian, et al., "Integration of Biomolecular Logic Gates with Field-Effect Transducers," Electrochim. Acta 2011, vol. 56, pp. 9661–9665.

 ISBN: 978-1-61208-380-3

[41] L. Halámková, et al., "Analysis of Biomarkers Characteristic of Porcine Liver Injury – From Biomolecular Logic Gates to Animal Model," Analyst 2012, vol. 137, pp. 1768–1770.

[31] E. Katz, J. Wang, M. Privman, and J. Halámek, "Multi-Analyte Digital Enzyme Biosensors with Built-in Boolean Logic," (Feature Article). Anal. Chem. 2012, vol. 84, pp. 5463–5469.

[32] E. Katz and J. Wang, in: Biomolecular Information Processing – From Logic Systems to Smart Sensors and Actuators, Willey-VCH, Weinheim, 2012, E. Katz (ed.), chap. 5, pp 81–101.

[33] M. Zhou, et al., "A self-powered "Sense-Act-Treat" system that is based on a biofuel cell and controlled by Boolean logic," Angew. Chem. Int. Ed. 2012, vol. 51, pp. 2686–2689.

[34] N. Zhou, et al., "Enzyme-Based NAND Gate for Rapid Electrochemical Screening of Traumatic Brain Injury in Serum," Anal. Chim. Acta 2011, vol. 703, pp. 94–100.

[35] V. Bocharova, et al. "Alert-Type Biological Dosimeter Based on Enzyme Logic System," Talanta 2011, vol. 85, pp. 800–803.

[36] M.-C. Chuang, et al., "High-Fidelity Simultaneous Determination of Explosives and Nerve Agent Threats via a Boolean Biocatalytic Cascade," Chem. Commun. 2011, vol. 47, pp. 3087–3089.

[37] T. Melham, "Modeling, Abstraction, and Computation in Systems Biology: A View from Computer Science," Prog. Biophys. Molec. Biol. 2013, vol. 111, pp. 129–136.

[38] S. Navlakha and Z. Bar-Joseph, "Algorithms in Nature: The Convergence of Systems Biology and Computational Thinking," Molec. Systems Biol. 2011, vol. 7, Article #546.

[39] D. D. Seaton and J. Krishnan, "Multispecific interactions in enzymatic signalling cascades," Information Processing in Cells and Tissues, Publisher: Springer, 2012, pp. 67–73.

[40] K. MacVittie, J. Halámek, V. Privman, and E. Katz, "A Bioinspired Associative Memory System Based on Enzymatic Cascades," Chem. Commun. 2013, vol. 49, pp. 6962–6964.

[41] V. Bocharova, et al., "Realization of Associative Memory in an Enzymatic Process: Toward Biomolecular Networks with Learning and Unlearning Functionalities," J. Phys. Chem. Lett. 2012, vol. 3, pp. 1234–1237.

[42] V. Privman and E. Katz, "Can bio-inspired information processing steps be realized as synthetic biochemical processes?" Physica Status Solidi A, 2014, http://dx.doi.org/10.1002/pssa.201400131.

[43] N. Wagner and G. Ashkenasy, "Systems Chemistry: Logic Gates, Arithmetic Units and Network Motifs in Small Networks," Chemistry Eur. J. 2009, vol. 15, pp. 1765–1775.

[44] S. Mangan and U. Alon, "Structure and Function of the Feed-Forward Loop Network Motif," Proc. Natl. Acad. Sci. USA 2003, vol. 100, pp. 11980–11985.

[45] S. S. Shen-Orr, R. Milo, S. Mangan, and U. Alon, "Network Motifs in the Transcriptional Regulation Network of Escherichia Coli," Nat. Genet. 2002, vol. 31, pp. 64–68.

[46] J. Macía, S. Widder, and R. Solé, "Specialized or flexible feed-forward loop motifs: a question of topology," BMC Systems Biology 2009, vol. 3 pp. 84–102.

[47] N. Kashtan and U. Alon, "Spontaneous evolution of modularity and network motifs," Proc. Natl. Acad. USA 2005, vol. 102, pp. 13773–13778.

[48] J. S. Mattick, "A New Paradigm for Developmental Biology," J. Exp. Biol. 2007, vol. 210, pp. 1526–1547.

[49] W. H. de Ronde, F. Tostevin, and P. R. ten Wolde, "Feed-forward loops and diamond motifs lead to tunable transmission of information in the frequency domain," Phys. Rev. E 2012, vol. 86, Article #021913.

[50] A. A. Apte, J. W. Cain, D. G. Bonchev, and S. S. Fong, "Cellular automata simulation of topological effects on the dynamics of feed-forward motifs." J. Biol. Eng. 2008, vol. 2, pp. 2–14.

[51] E. Dekel, S. Mangan, and U. Alon, "Environmental Selection of the Feed-Forward Loop Circuit in Gene-Regulation Networks," Phys. Biol. 2005, vol. 2, pp. 81–88.

[52] F. Tostevin and P. R. ten Wolde, "Mutual Information between Input and Output Trajectories of Biochemical Networks," Phys. Rev. Lett. 2009, vol. 102, Article #218101.

[53] A. U. Igamberdiev and M. R. Roussel, "Feedforward non-Michaelis-Menten mechanism for CO2 uptake by Rubisco: Contribution of carbonic anhydrases and photorespiration to optimization of photosynthetic carbon assimilation," BioSystems, 2012, vol. 107, pp. 158–166.

[54] S. Huang, "Back to the biology in systems biology: what can we learn from biomolecular networks," Brief Funct Genomics Proteomics 2004, vol. 2, pp. 279–297.

[55] D. Y. Zhang, A. J. Turberfield, B. Yurke, and E. Winfree, "Engineering Entropy-Driven Reactions and Networks Catalyzed by DNA," Science 2007, vol. 318, pp. 1121–1125.

[56] E. Katz, V. Privman, and J. Wang, "Towards Biosensing Strategies Based on Biochemical Logic Systems," Proc. Quantum, Nano and Micro Technol. 2010. ICQNM '10. Fourth Int. Conf. 2010, pp.1-9.

[57] V. Privman, G. Strack, D. Solenov, M. Pita, and E. Katz, "Optimization of Enzymatic Biochemical Logic for Noise Reduction and Scalability: How Many Biocomputing Gates Can Be Interconnected in a Circuit?" J. Phys. Chem. B 2008, vol. 112, pp. 11777–11784.

[58] U. Pischel and B. Heller, "Molecular logic devices (half-subtractor, comparator, complemementary output circuit) by controlling photoinduced charge transfer processes," New J. Chem. 2008, vol. 32, pp. 395–400.

[59] M. Amelia, M. Baroncini, and A. Credi, "A Simple Unimolecular Multiplexer/Demultiplexer," Angew. Chem. Int. Ed. 2008, vol. 47, pp. 6240–6243.

[60] M. Georgiopoulos, C. Li, and T. Kocak, "Learning in the Feed-Forward Random Neural Network: A Critical Review," Performance Eval. 2011, vol. 68, pp. 361–384.

[61] A.-J. Annema, Feed-Forward Neural Networks: Vector Decomposition Analysis, Modelling and Analog Implementation, Springer Science, 1996, New York.

[62] U. Alon, "Network Motifs: Theory and Experimental Approaches," Nature Rev. 2007, vol. 8, pp. 450–461.

[63] A. Arkin and J. Ross, "Computational functions in biochemical reaction networks," Biophysical Journal 1994, vol. 67, pp. 560–578.

[64] D. Wolf and A. Arkin, "Motifs, modules and games in bacteria," Curr. Opin. Microbiol. 2003, vol. 6, pp. 125–134.

[65] J. J. Collins, et al., "Synthetic biology: How best to build a cell" Nature 2014, vol. 509, pp. 155–157.

[66] M. Shein-Idelson, E. Ben-Jacob, and Y. Hanein, "Engineered Neuronal Circuits: A New Platform for Studying the Role of Modular Topology," Frontiers in Neuroengineering 2011, vol. 4, pp. 10–21.

[67] L. Qian and E. Winfree, "A Simple DNA Gate Motif for Synthesizing Large-Scale Circuits," J. R. Soc. Interface 2011, vol. 8, pp. 1281–1297.

[68] M. A. Savageau, Biochemical Systems Analysis: A Study of Function and Design in Molecular Biology, Addison–Wesley, Reading, MA, 1976.

[69] N. Rosenfeld and U. Alon, "Response delays and the structure of transcription networks," J. Mol. Biol. 2003, vol. 329, pp. 645–654.

[70] N. Rosenfeld, M. B. Elowitz, and U. Alon, "Negative Autoregulation Speeds the Response Times of Transcription Networks," J. Mol. Biol. 2002, vol. 323, pp. 785–793.

 ISBN: 978-1-61208-380-3

Structural and Energetic Properties of Au@Ag and Ag@Au Core-Shell Nanoparticles

Ronei Miotto

Centro de Ciências Naturais e Humanas
Universidade Federal do ABC
Santo André, SP, Brazil
Email: ronei.miotto@ufabc.edu.br

L. H. Santos, F. D. Kiss, and A. C. Ferraz

Instituto de Física
Universidade de São Paulo
São Paulo, SP, Brazil

***Abstract*—Using first principles density functional calculations, the stability and structural properties Au@Ag and Ag@Au core shell nanoparticles is explored. Our data shows that the growth of Au shell layers on an Ag core nanoparticle is more likely to happen than the growth of Ag shell layers on an Au core nanoparticle. Our structural analysis indicates that lower coordinated sites experience a bigger contraction when compared to the metallic 12 coordinated sites. In addition, our structural and energetic data for homonuclear Au and Ag nanoparticles indicate that dispersion forces do not decisively influence these properties.**

Keywords–nanoparticle; core-shell; dispersion forces

I. INTRODUCTION

Metal nanoparticles (Nps) show size and shape-dependent optical and electronic properties that are appreciable different from those observed for bulk metals. These has lead to extensive investigations involving metallic nanoparticles as building blocks for nanoscale materials and devices. In particular, gold and silver nanoparticles have been extensively explored in a variety of fields, including catalysis, food industry, environmental conservation, fluorescence biosensors, glucose biosensors, nucleic acids-based biosensors, protein-based biosensors, drug delivery vehicles and cancer therapeutic agents [1].

Since gold presents high biocompatibility, chemical stability, and easy surface modification, it is often considered to be more suitable for biomedical applications [1]. Silver, on the other hand, presents higher plasmonic efficiency and superior magnetic enhancement in the visible range and it is more attractive for optoelectronics, photovoltaics, and sensing [1]. In order to combine these properties, a great deal of attention has been devoted to the synthesis of core shell and alloy bimetallic NPs. The main idea is to tune the NPs optical catalytic properties and making them useful in other fields, such as taggants for security applications [2].

The AuAg system is of particular interest since the Surface Plasmon Resonance (SPR) band might be tunable between $\sim$520 nm for Au and $\sim$410 nm for Ag [2]. These interesting physical and chemical properties appear because of the combination of two kinds of metals and their fine structures, evolving new surface characteristics. With a view to contribute to a better understanding of the surface properties of these complex systems, in this work we explore the stability and structural properties Au@Ag and Ag@Au core shell NPs. In addition, the influence of dispersion (van der Waals) interactions in the core shell properties is also discussed.

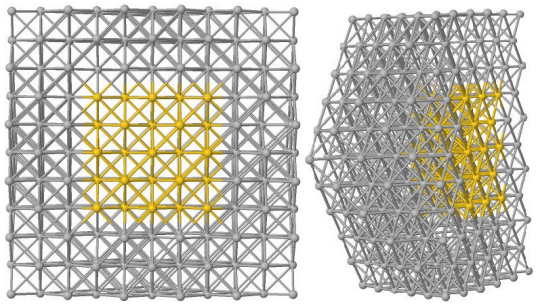

Figure 1. Schematic representation of a 561 atoms nanoparticle, with 2 gold core layers (gold atoms) and 3 silver shell layers (gray atoms), refered as 3Ag@2Au for simplicity.

The paper is structured as follows. In Section II, we briefly describe our theoretical approach. In Section III, our results for Au@Ag and Ag@Au core shell NPs are discussed and compared to available theoretical and experimental works. Finally, a summary is presented in Section IV.

II. THEORETICAL MODELING

Cube-octahedral nanoparticles with 147, 309, 561 and 923 atoms are modeled considering an extended bulk with a face centered cubic (FCC) crystalline packing properly cut to give the desired geometry, following the procedure described in [3]. These nanoparticle's sizes where chosen in order to guarantee that the studied systems can properly represent the nanoparticle's properties [3]. By construction, our nanoparticles are similar to onions, i.e., the growth of a nanoparticle is done by layers. This is consistent with the experimental findings by Maenosono and co-workers [4] suggesting that the shell layers thickness can be closely controlled. The 561 atoms nanoparticle, for example, has 5 layers. Core shell nanoparticles are then constructed by the exchange of a complete layer of atoms. Following this picture, for a 561 atoms nanoparticle, for example, 3Ag@2Au indicates a nanoparticle with 2 gold core layers and 3 silver shell layers. The 3Ag@2Au nanoparticle is schematically represented in Figure 1.

Our simulations are performed considering the supercell scheme and a vacuum region greater than 10 Å between the images. The ionic potentials are described by ultra-soft pseudopotential [5][6][7] and the electron-electron exchange-correlation interactions are described within density functional theory (DFT) considering the generalized gradient approximation as proposed by Perdew and Wang (PW91) [8]. Spin

 ISBN: 978-1-61208-380-3

polarization effects, as considered in the Vienna Ab-initio Simulation Package (VASP) [9][10], are explicitly treated. The single-particle orbitals are expressed in a plane waves base with energy up to 290 eV, considering only the Γ point inside the Brillouin zone. Increasing the number of **k**-points or the basis set results in changes in total energies, atomic distances and vibrational modes smaller than 0.05%, 0.1% and 0.8%, respectively. The atoms are assumed to be on their low energy position when the forces are smaller than 10 meV/Å. Dispersion forces, indicated by vdW for short, are taken into account by a simple pair-wise force field, as proposed by Grimme [11]. The C6 and R0 vdW parameters for gold (silver) are 40.62 (24.67) and 1.772 (1.639), respectively. Formation energy per atom is obtained using

$$E_f = \frac{E_{system} - (N_{Ag} \times \mu_{Ag} + N_{Au} \times \mu_{Au})}{N_{tot}}, \qquad (1)$$

where E_{system} is the total energy of a given configuration, N_{Au} and N_{Ag} are the total number of Au and Ag atoms, respectively, μ_X is the chemical potential of atom X and $N_{tot} = N_{Au} + N_{Ag}$, i.e., the total number of atoms in the system.

III. Results and Discussion

In the first step of our study, we investigate the influence of the inclusion of dispersion forces (vdW) on the energetic and structural properties of different sized homonuclear nanoparticles. Figure 2 presents the energy per atom for different gold and silver nanoparticles, bare surfaces and metallic bulk against their mean coordination number. Nanoparticles with 147, 309, 561 and 923 atoms have coordinations numbers 8.98, 9.63, 10.05, and 10.35, respectively. The bare 001 and 111 coordination numbers are 10.67 and 11.00, while the bulk coordination number is 12. It is clear from this figure that both gold and silver have similar linear regression coefficients: 0.23 and 0.21, respectively, when vdW is included and 0.13 in both cases when dispersion forces are not included. In other words, the effect of vdW is different for different sized nanoparticles. When vdW is included, the overall change in energy per atom is smaller for smaller nanoparticles. This is probably related to the fact that smaller nanoparticles also have smaller coordination numbers. In other words, since smaller nanoparticles have a smaller percentile number of ideal 12-coordinated sites, vdW interactions are more relevant in the description of the lower coordinated sites. This is consistent with previous observations of smaller energy differences for atomic adsorption, e.g., noble gases [12], on metallic surface sites with different coordinations when vdW interactions are considered.

In Table I, we compare the average bond contraction for homonuclear Ag nanoparticles as a function of its coordination sites considering (vdW) or not (no vdW) dispersion forces. The average bond contraction, in %, was found comparing the average bond distance between a given atom site and its first neighboring atoms for the ideal bulk NP and the relaxed one. The mean value is obtained considering all studied nanoparticles. It is clear from this table that lower coordinated sites experiences a bigger contraction when compared to the metallic 12 coordinated sites. Similar contraction patterns are observed for Au nanoparticles. The inclusion of dispersion forces only slightly decreases the observed contractions. Our

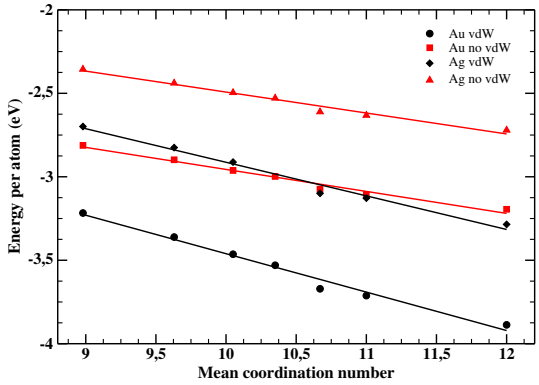

Figure 2. Energy per atom, in eV, for different gold and silver nanoparticles, bare surfaces and metallic bulk against their mean coordination number. The solid lines are linear regression fits.

TABLE I. Average bond contraction, in %, of silver NPs for different coordination sites considering (vdW) or not (no vdW) dispersion forces.

site	average contraction (%)	
	vdW	no vdW
c5	3.5	4.3
c7	2.1	2.6
c8	1.1	1.5
c9	0.9	1.0
c12	1.1	1.2

structural and energetic data for homonuclear Au and Ag nanoparticles indicate that dispersion forces do not decisively influence these properties. Therefore, in the following discussion, we will present only the results obtained for one set of calculations and comment on the other.

In Figure 3, we present the difference in formation energies, or energy gain in eV, (no vdW) when a new shell is adsorbed on the top of a 147 nanoparticle (corresponding to 3 atomic layers). We consider both Ag and Au cores covered by additional Au or Ag shell layers. Our calculations indicate that starting from an Au core, it is always less favorable to encapsulate it with one or more Ag shell layers rather than adding an additional Au shell layer. For an Ag core nanoparticle, on the other hand, the addition of Au shell layers is always more favorable than the growth of a bigger homonuclear Ag nanoparticle. In other words, our data indicates that the growth of an Au shell layer on an Ag core nanoparticle is more likely to happen than the growth of Ag shell layers on an Au core nanoparticle. Similar results were obtained for larger (306 and 561) nanoparticles. This is consistent with the experimental findings indicating that growth of Ag shells on Au cores requires a reducing agent for reducing Ag(I) to Ag(0). In contrast, growth of Au shells on Ag can often be accomplished by galvanic exchange or transmetalation reactions that oxidize Ag(0) to Ag(I) dissolved in solution while reducing Au(III) or Au(I) to Au(0) [2]. As a consequence, Ag@Au nanoparticles are characterized by a smooth Ag shell layer, observed by Güzel *et al* [13] using Ultraviolet visible (UVVis), Reflection Absorption Infra-Red (RAIRS) and X-ray photoelectron (XPS) spectroscopy. Our findings are also consistent with other synthetic routes, such as the use of Neem (Azadirachta indica) leaf broth, proposed

 ISBN: 978-1-61208-380-3

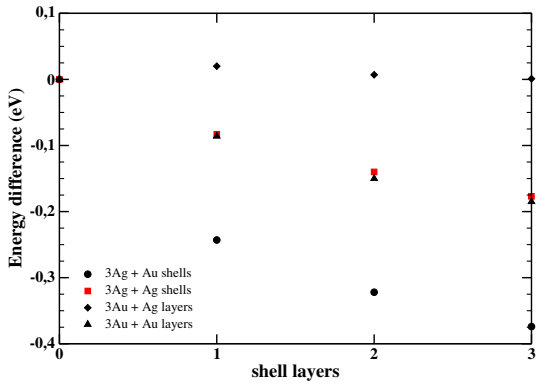

Figure 3. Formation energy difference (no vdW), in eV, when a new shell is adsorbed on the top of a 147 nanoparticle (corresponding to 3 atomic layers).

by Shankar et al. [14]. Using this approach, Shankar et al. have found that in a competitive process involving both silver and gold ions, the reduction of gold ions is accelerated. As a consequence, silver do not form a uniform layer around core gold nanoparticles, but rather form small nanoparticles that decorate them. Although small energy differences are observed when dispersion forces (vdW) are considered, the same energy pattern was found. It is important to mention that our simulations do not consider possible exchange or diffusion mechanisms, although they might play an important role in the growth process, as suggested by Shibata et al. [15].

Next, we analyze the shape of the studied nanoparticles. By construction, all unrelaxed nanoparticles considered present a cube-octahedral structure. The largest distance inside a nanoparticle is from the central atom to the c5 site. Upon relaxation, for Ag using vdW, this distance experiences a contraction ranging from 0.13 Å, or 1.5%, to 0.31 Å, or 1.8%, when the size of the nanoparticle increases from 147 to 923 atoms. A larger contraction is observed for gold nanoparticles and vdW: 0.10 Å (1.1%) and 0.43 Å (2.5%), respectively. In a similar manner, the bond angles between the c5 site and its 4 first neighbors is 300° for the unrelaxed nanoparticle. Upon relaxation, increasing the size of the nanoparticles from 147 to 923, the angles increase to 305° and 309° for silver and to 310° and 313° for gold, respectively. Therefore, our data indicates that, for pure cube-octahedral samples, gold nanoparticles are more likely to have a spherical shape when compared to silver nanoparticles. This is in agreement with TEM images obtained by Shankar et al. [14] indicating that gold and silver nanoparticles formed were predominantly spherical, although thin planar structures were also observed for the former, when Neem leaf broth was used in the nanoparticles synthesis process.

We next analyze the 3Ag@3Au, 3Au@3Ag, 2Ag@4Au and 2Au@4Ag 923 atom core-shell nanoparticles. The same contraction pattern of pure nanoparticles is observed, i.e., we observe a larger contraction for Au@Ag when compared to Ag@Au nanoparticles. Interestingly, with only 2 Au shell layers (2Au@4Ag) and vdW the distance between the c5 and the central atom (0.43 Å) is already of the same magnitude observed for the pure gold 923 atoms nanoparticle. The bond angles between the c5 site and its 4 neighboring atoms for Au@Ag nanoparticles (313°) are similar to the ones observed for pure Au nanoparticles. In a similar manner, the bond angles for Ag@Au (309°) are close to the values observed for pure Ag nanoparticles. In other words, our data indicates that Au@Ag nanoparticles are more rounded when compared to Ag@Au nanoparticles, in a clear indication that the structural behavior of core-shell nanoparticles are dominated by the shell layers, with small influence of the core. This is consistent with the TEM images obtained by Shankar and co-workers [14] suggesting that the Ag@Au nanoparticles are predominantly spherical in morphology. In a similar manner, Güzel *et al* [13] TEM images of Au and Au@Ag NPs showed that most of these nanoparticles present a spherical shape. In addition, Shankar et al., based on a comparison of the TEM images of silver, gold, and bimetallic Ag@Au nanoparticles, suggested that the cores in the bimetallic Ag@Au nanoparticles resemble that of pure gold nanoparticles and the particles constituting the shell resemble pure silver nanoparticles in terms of both their size and shape.

IV. Conclusions

Using first principles density functional calculations, the stability and structural properties Au@Ag and Ag@Au core shell nanoparticles are explored. Our data shows that the growth of an Au shell layers on an Ag core nanoparticle is more likely to happen than the growth of an Ag shell layers on an Au core nanoparticle. Our structural analysis indicates that lower coordinated sites experience a bigger contraction when compared to the metallic 12 coordinated sites. Our structural and energetic data for homonuclear Au and Ag nanoparticles indicate that dispersion forces do not decisively influence these properties. Our data indicates that the effect of vdW is different for different sized nanoparticles. When vdW is included, the overall change in energy per atom is smaller for smaller nanoparticles. In addition, our results indicate that Au@Ag nanoparticles are more rounded when compared to Ag@Au nanoparticles, in a clear indication that the structural behavior of core-shell nanoparticles are dominated by the shell layers, with small influence of the core. In the next step of our work, the adsorption of functional groups and species on different nanoparticle's surfaces are going to be investigated.

Acknowledgements

The authors acknowledge financial support from CNPq and FAPESP (project 2012/50680-5). This work was partially developed at the USP-Rice Bluegene computational facilities.

References

[1] A. Majdalawieh, M. C. Kanan, O. El-Kadri, and S. M. Kanan, "Recent Advances in Gold and Silver Nanoparticles: Synthesis and Applications," Journal of Nanoscience and Nanotechnology, vol. 14, no. 7, Jul. 2014, pp. 4757–4780. [Online]. Available: http://openurl.ingenta.com/content/xref?genre=article&issn=1533-4880&volume=14&issue=7&spage=4757

[2] M. S. Shore, J. Wang, A. C. Johnston-Peck, A. L. Oldenburg, and J. B. Tracy, "Synthesis of Au(Core)/Ag(Shell) nanoparticles and their conversion to AuAg alloy nanoparticles." Small (Weinheim an der Bergstrasse, Germany), vol. 7, no. 2, Jan. 2011, pp. 230–4. [Online]. Available: http://www.ncbi.nlm.nih.gov/pubmed/21213387

[3] F. D. Kiss, R. Miotto, and A. C. Ferraz, "Size effects on silver nanoparticles' properties." Nanotechnology, vol. 22, no. 27, Jul. 2011, p. 275708. [Online]. Available: http://www.ncbi.nlm.nih.gov/pubmed/21597143

 ISBN: 978-1-61208-380-3

[4] S. Maenosono, J. Lee, A. T. N. Dao, and D. Mott, "Peak shape analysis of Ag 3d core-level X-ray photoelectron spectra of Au@Ag core-shell nanoparticles using an asymmetric Gaussian-Lorentzian mixed function," Surface and Interface Analysis, vol. 44, no. 13, Dec. 2012, pp. 1611–1614. [Online]. Available: http://doi.wiley.com/10.1002/sia.5078

[5] D. Vanderbilt, "Optimally smooth norm-conserving pseudopotentials," Physical Review B, vol. 32, no. 12, Dec. 1985, pp. 8412–8415. [Online]. Available: http://link.aps.org/doi/10.1103/PhysRevB.32.8412

[6] ——, "Soft self-consistent pseudopotentials in a generalized eigenvalue formalism," Physical Review B, vol. 41, no. 11, Apr. 1990, pp. 7892–7895. [Online]. Available: http://link.aps.org/doi/10.1103/PhysRevB.41.7892

[7] G. Kresse, "From ultrasoft pseudopotentials to the projector augmented-wave method," Physical Review B, vol. 59, no. 3, Jan. 1999, pp. 1758–1775. [Online]. Available: http://link.aps.org/doi/10.1103/PhysRevB.59.1758

[8] J. P. Perdew, K. A. Jackson, M. R. Pederson, D. J. Singh, and C. Fiolhais, "Atoms, molecules, solids, and surfaces: Applications of the generalized gradient approximation for exchange and correlation," Physical Review B, vol. 46, no. 11, Sep. 1992, pp. 6671–6687. [Online]. Available: http://link.aps.org/doi/10.1103/PhysRevB.46.6671

[9] G. Kresse, "Efficient iterative schemes for ab initio total-energy calculations using a plane-wave basis set," Physical Review B, vol. 54, no. 16, Oct. 1996, pp. 11 169–11 186. [Online]. Available: http://link.aps.org/doi/10.1103/PhysRevB.54.11169

[10] G. Kresse and J. Furthmüller, "Efficiency of ab-initio total energy calculations for metals and semiconductors using a plane-wave basis set," Computational Materials Science, vol. 6, no. 1, Jul. 1996, pp. 15–50. [Online]. Available: http://linkinghub.elsevier.com/retrieve/pii/0927025696000080

[11] S. Grimme, "Semiempirical GGA-type density functional constructed with a long-range dispersion correction." Journal of computational chemistry, vol. 27, no. 15, Nov. 2006, pp. 1787–99. [Online]. Available: http://www.ncbi.nlm.nih.gov/pubmed/16955487

[12] Q.-S. Chen, F. J. Vidal-Iglesias, J. Solla-Gullon, S.-G. Sun, and J. M. Feliu, "Role of surface defect sites: from Pt model surfaces to shape-controlled nanoparticles," Chemical Science, vol. 3, 2012, pp. 136–147.

[13] R. Güzel, Z. Ustünda, H. Eki, S. Keskin, B. Taner, Z. G. Durgun, A. A. I. Turan, and A. O. Solak, "Effect of Au and Au@Ag core-shell nanoparticles on the SERS of bridging organic molecules." Journal of colloid and interface science, vol. 351, no. 1, Nov. 2010, pp. 35–42. [Online]. Available: http://www.ncbi.nlm.nih.gov/pubmed/20701922

[14] S. S. Shankar, A. Rai, A. Ahmad, and M. Sastry, "Rapid synthesis of Au, Ag, and bimetallic Au core-Ag shell nanoparticles using Neem (Azadirachta indica) leaf broth." Journal of colloid and interface science, vol. 275, no. 2, Jul. 2004, pp. 496–502. [Online]. Available: http://www.ncbi.nlm.nih.gov/pubmed/15178278

[15] T. Shibata, B. A. Bunker, Z. Zhang, D. Meisel, C. F. Vardeman, and J. D. Gezelter, "Size-Dependent Spontaneous Alloying of AuAg Nanoparticles," Journal of the American Chemical Society, vol. 124, no. 40, Oct. 2002, pp. 11 989–11 996. [Online]. Available: http://pubs.acs.org/doi/abs/10.1021/ja026764r

 ISBN: 978-1-61208-380-3

Analysis of Furnace Operational Parameters for Controllable Annealing of Thin Films

Victor Ovchinnikov
Department of Aalto Nanofab
School of Electrical Engineering, Aalto University
Espoo, Finland
e-mail: Victor.Ovchinnikov@aalto.fi

***Abstract*—Annealing of thin silver films in different furnaces is studied. It is shown that identical parameters of thermal treatment do not guarantee reproducibility and annealing provides different results, e.g., shape and size of nanostructures, in different furnaces. To clarify the source of variation, morphology and reflectance spectra of the samples are analyzed. Additionally, numerical simulation of heating process in a diffusion furnace has been performed. It is demonstrated that uncontrollable heating and cooling of silver film itself leads to variation of annealing results.**

Keywords-self-assembling; silver thin film; diffusion furnace; annealing

I. INTRODUCTION

Annealing is well known and broadly used in microfabrication heat treatment of inorganic materials. In case of polymer, heat treatment is called baking, curing or drying. From the beginning of semiconductor technology, annealing is used to modify properties of thin films, substrates and interfaces. Annealing is not the crucial microfabrication method like lithography or etching, but it is utilized in every process flow for doping of semiconductors, silicide formation, densification of deposited films and sample surface conditioning [1]. Annealing is done in furnaces, which can have different design: convection and diffusion furnaces, hot plates and rapid thermal processing tools, infrared (IR) and curing ovens. Usual description of annealing in publications includes only temperature and duration of the process [1, 2]. Sometimes information about gas flow is added [3, 4] and it is very seldom written about furnace design and sample position in the furnace [5]. However, different annealing tools deliver heat energy to a sample in different ways what directly affects on obtained results.

During annealing, the heat exchange between sample and furnace is performed by thermal conductivity, convection and thermal radiation. Depending on furnace design, one or other heat transfer mode can be done dominant. For example, a hot plate mainly heats a sample by thermal conductivity, a diffusion furnace - by thermal radiation and convection, an IR oven - by thermal radiation. In all furnaces heat is not only generated, but is also dissipated. As a result, the sample temperature is controlled by thermal balance between heating and cooling processes.

Additionally, the sample thermal parameters (emissivity, thermal conductivity and heat capacitance) and sample arrangement in a furnace (position, holder design and shields) affect on the heating process dynamics and the sample temperature. The most complicate situation happens in case of phase transition of the heated thin film, e.g., melting or recrystallization. As a consequence, the sample emissivity is changed and the new thermal balance is installed.

In this paper, we demonstrate that identical heating ramp, temperature and time of the annealing are not sufficient conditions for reproducing of nanostructures fabricated by annealing of thin silver films. We compare design of three annealing tools and analyze relative strength of different heating modes in all tools. On the base of optical properties and crystalline structure of the annealed and as-deposited samples we make conclusions about melting and crystallization of silver nanostructures. To find temperature field of the furnace and the real sample temperature we simulate the heating processes in the diffusion furnace for different gas flows and sample emissivities. The obtained results are used to find correlation between annealing conditions and morphology of silver nanostructures.

The paper is organized as follows. In the subsequent Section II, details of sample preparation and measurement procedures are presented. In Section III, the results of work are demonstrated by scanning electron microscope (SEM) images and reflectance spectra of the silver films and also by heat transfer simulations. The effect of furnace design on silver film annealing is discussed in Section IV. In Section V, the conclusions are drawn.

II. EXPERIMENTS

Four identical samples were prepared to compare annealing in different furnaces. For this purpose, a 12 nm thick silver film was deposited by electron beam evaporation at rate 0.2 nm/s. As a substrate was used 4” silicon wafer with 21 nm layer of thermal oxide. After deposition the whole wafer was cut on four quotes, which were further processed separately. Annealing was done at 400 ºC during 5 minutes with heating ramp 21 ºC/min, and cooling ramp 3.6 ºC/min. However, all samples were processed in various furnaces (Fig. 1).

 ISBN: 978-1-61208-380-3

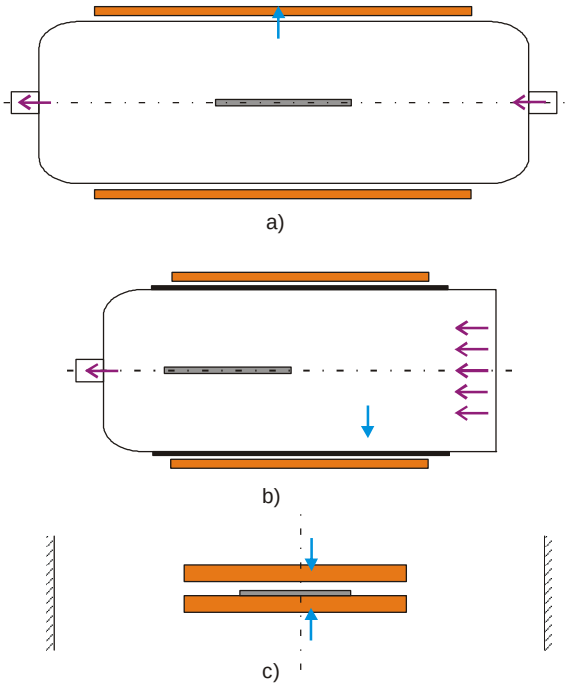

Figure 1. Design of the diffusion furnace (a), the fast ramping furnace (b) and the hot plate (c). Thermocouple positions and gas flows are denoted by blue and vilolet arrows, respectively. Heating surfaces are orange.

The sample #1 was annealed in the diffusion furnace (Fig. 1a). As a sample holder was used a 4" silicon wafer on a quartz boat, which was located in the centre of the furnace during experiment. It was supposed that heat exchange through the quartz boat was negligible. The quartz furnace

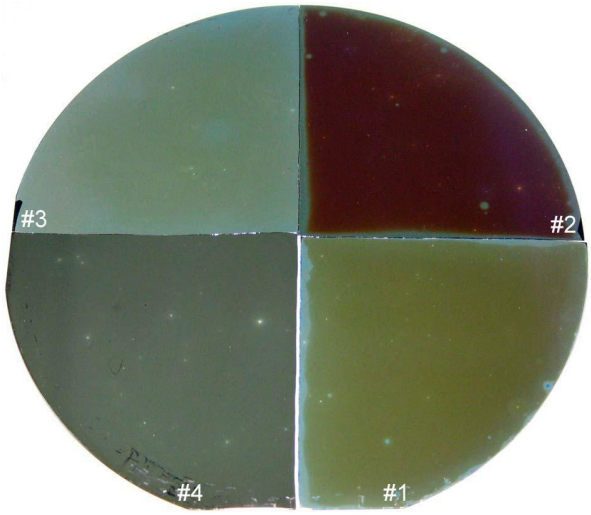

Figure 2. Optical images of the annealed (#1 - #3) and as-deposited (#4) samples.

tube had 4½ inch diameter, 96 cm length and 3 mm thick walls. The resistive heater (orange strips in Fig. 1a) was situated around the tube with the gap 1 cm. The furnace temperature was controlled according to thermocouple measurements on the tube surface. Room temperature nitrogen with flow 8.3×10^{-5} standard m^3/s was introduced in the furnace along its axis.

The sample #2 was annealed in a fast ramping furnace (Fig. 1b). Temperature, gas flow and process duration were similar for both furnaces (Fig. 1a and 1b). However, in the

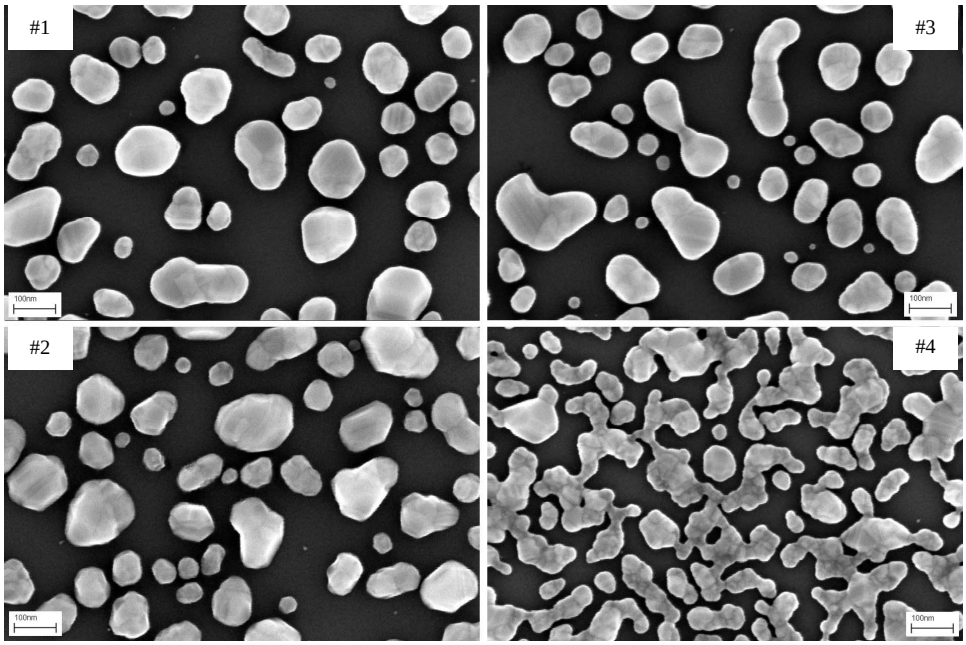

Figure 3. Plan SEM images of the annealed (#1 - #3) and as-deposited (#4) samples.

 ISBN: 978-1-61208-380-3

fast ramping furnace the quartz tube length was 35 cm and the sample position was close to the exhaust of furnace. As a heater were used tungsten lamps. The quartz tube was covered by the heat absorbing shield (black lines in Fig. 1b). The gas temperature in the tube was measured by thermocouple and was used for process control. Nitrogen was introduced through array of holes in the right part of the furnaces. The sample #3 was annealed between two hot plates in vacuum (Fig. 1c). Both hot plates had 4 inch in diameter and were separated by 2.5 mm gap. The chamber wall temperature was close to room temperature.

The silver films were deposited in the e-beam evaporation system IM-9912 (Instrumentti Mattila Oy) at base pressure of 2.7×10^{-5} Pa and at room temperature of the substrate. Annealing of the sample #1 was done in the diffusion furnace THERMCO Mini Brute MB-71. Annealing of the sample #2 was done in the fast ramping furnace PEO-601 from ATV Technology GmBH. Annealing of the sample #3 was done in the wafer bonder AML AWB-04 from Microengineering Ltd.

Plan view SEM images of the samples were observed with the Zeiss Supra 40 field emission scanning electron microscope. Reflectance measurements were carried out using the FilmTek 4000 reflectometer in the spectral range from 400 to 1700 nm. Crystalline structure of the silver films was estimated by reflection high-energy electron diffraction (RHEED) observations with the help of the diffractometer embedded in a molecular beam epitaxy tool.

III. RESULTS

Fig. 2 shows the optical image of three annealed samples (#1-#3) and as-deposited silver film (#4). The picture was taken by the digital camera with flash. Despite of identical temperature and time of annealing all samples have different colours of surface. The sample #1 is yellow-green, the sample #2 is brown-red, the sample #3 is yellow-blue and the as-deposited sample is grey. Bulk silver is a perfect reflector, however, nanostructured silver possesses plasmon resonances, which modify reflection spectra of the samples [5-7]. Therefore, the obtained colour variation could be explained by silver nanostructures formed on the sample surface instead of the continuous silver film. To clarify the suggestion we have observed all samples in SEM (Fig. 3). The as-deposited silver film (#4) is already discontinuous, has lace like structure and silver covers relatively large part of surface in comparison with annealed films. The annealed samples have close values of silver areal density and nanostructure sizes, but shape of nanoislands depends on annealing conditions. The sample #2 demonstrates most irregular islands with straight flats on some of them. The sample #3 has roundish nanostructures with large shape deviation and the sample #1 shows intermediate picture between two previous cases. The height of all annealed nanostructures is around 30 nm.

It was mentioned above that colour variation of the samples could be explained by their reflection spectra, which are connected with plasmonic properties of nanostructures. Fig. 4a demonstrates reflection spectra of the annealed and

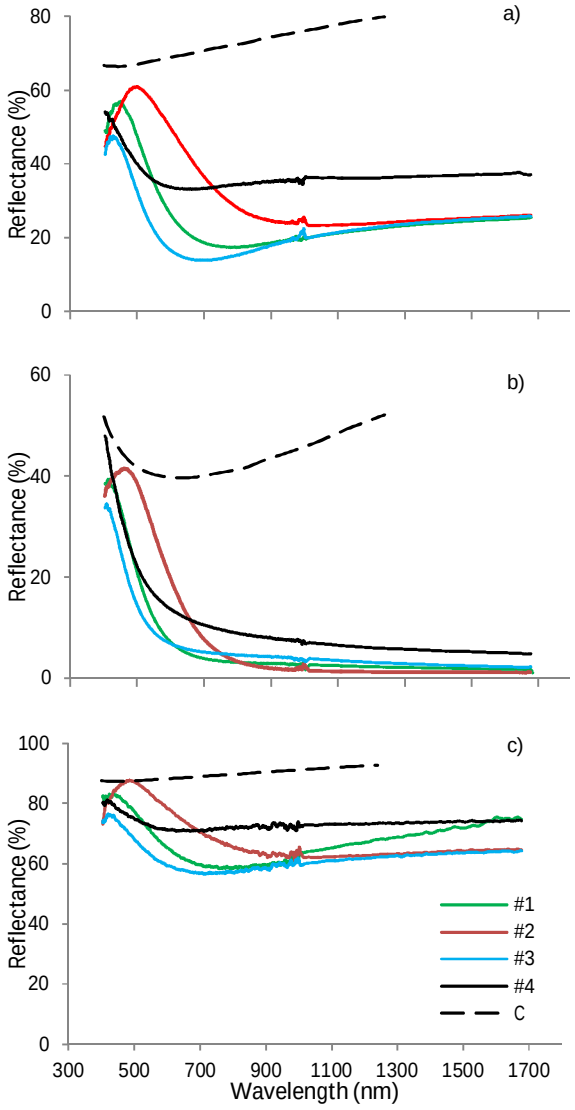

Figure 4. Reflection spectra for normal (a) and inclined (70º) light incident for *p*-(b) and *s*- polarization (c). Dashed lines show calculated spectra.

as-deposited samples at normal light incidence. In the Fig. 4b and 4c the same spectra are shown for inclined light incident (70º) and for *p*- and *s*- polarization, respectively. According to surface colour, the sample #2 has main peak at the longest wavelength 498 nm, the sample #3 at the shortest wavelength 411 nm and the sample #1 at the intermediate wavelength 449 nm for *s*-polarized light (Fig. 4c). The as-deposited sample (#4) has no reflection peaks in the range of measurements, but it has trough at the wavelength 658 nm.

On the other hand, the sample #2 has no troughs at all and the samples #3 and #1 have troughs at 694 nm and 806 nm, respectively. For *p*-polarized light strong reflection is observed only in visible range (below 800 nm). In IR

 ISBN: 978-1-61208-380-3

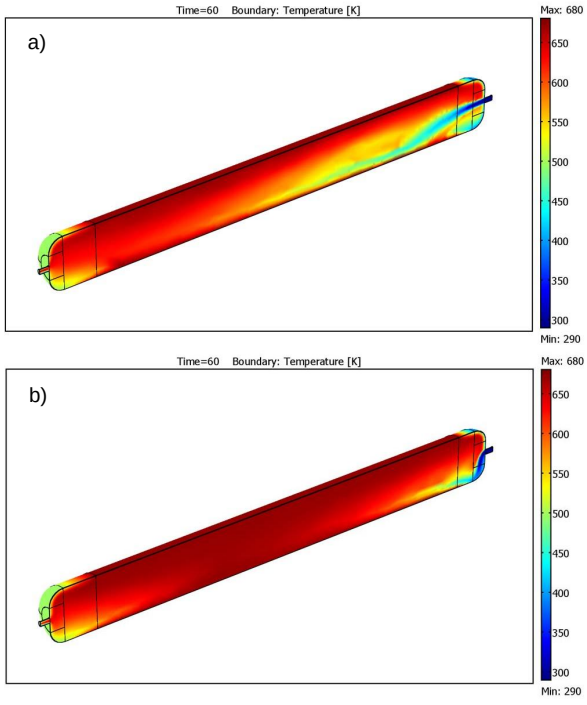

Figure 5. Temperature fields of the diffusion furnace for high (a) and low (b) nitrogen flows. The gas inlet is on the right.

p-polarized reflectance falls down to 1-2% for all annealed samples and to 5% for the as-deposited sample. In IR range (above 1200 nm), spectra of the annealed samples coincide with each other what justifies suggestion about identical silver areal density. Dashed lines show theoretical spectra of the samples, calculated with the help of bulk silver optical parameters.

The RHEED showed relatively sharp, continuous Laue circles in addition to amorphous background pattern for the sample #3. Therefore, this sample contains separate crystalline particles, but their orientation varies from island to island [8]. For other samples, intensity and sharpness of the diffraction patterns were weaker and decreased in the following order: sample #1, as-deposited sample, sample #2. In other words, sample #2 includes nanoislands with the most disordered crystalline structure.

3D simulations of annealing process were done for the diffusion furnace (Fig. 1a) with the help of software COMSOL Multiphysics 3.5a. Due to high computational load the simulations were done in two phases. Firstly, temperature and velocity fields inside of the empty furnace were found. For this purpose two models were used in coupled mode: general heat transfer model (calculates thermal conduction and convection) and Navier –Stokes model for non-isothermal flow. Gravitational force arisen due to gas density variation was taken into account in the Navier –Stokes model. At the second phase, the obtained temperature and velocity of gas were used as boundary conditions for simulation of silicon wafer heating in the hot cylindrical tube. At this stage all heat transfer modes, including sample, tube and gas thermal conduction, convection in nitrogen and surface-to-surface radiation were taken into account.

Fig. 5 demonstrates the simulation results obtained at the first phase. Temperature distributions in the diffusion furnace (Fig. 1a) were calculated for quartz tube temperature 400 ºC and for gas flows 8.3×10^{-5} standard m^3/s (Fig. 5a) and 1.0×10^{-5} standard m^3/s (Fig. 5b). Large flow of cold gas creates non-uniform temperature distribution inside of the tube and the gas temperature in the middle of the furnace (below sample holder) can be 150 ºC lower than the tube temperature (Fig. 5a). At the same place gas velocity reaches maximum value 0.18 m/s. At small flow of nitrogen (Fig. 5b), temperature variation and gas velocity in the middle of furnace do not exceed 15 ºC and 0.03 m/s, respectively.

Temperature and velocity fields near the wafer are illustrated in Fig. 6a and Fig. 6b, respectively. They are obtained at the second phase of simulations (temperature and velocity of gas at the entrance are taken from Fig. 5a) for nitrogen flow 8.3×10^{-5} standard m^3/s and sample emissivity ε=1. The internal furnace volume is divided by the wafer-holder in two parts – the upper one with high temperature and low velocity and the lower one with low temperature and high velocity. In the upper volume gas has temperature 398 ºC and slowly moves with velocity 0.02 m/s. In the lower volume high temperature and velocity gradients exist. However, the wafer temperature variation does not exceed 1ºC due to high thermal conductivity of silicon. In the present experiment, the wafer temperature depends on tube

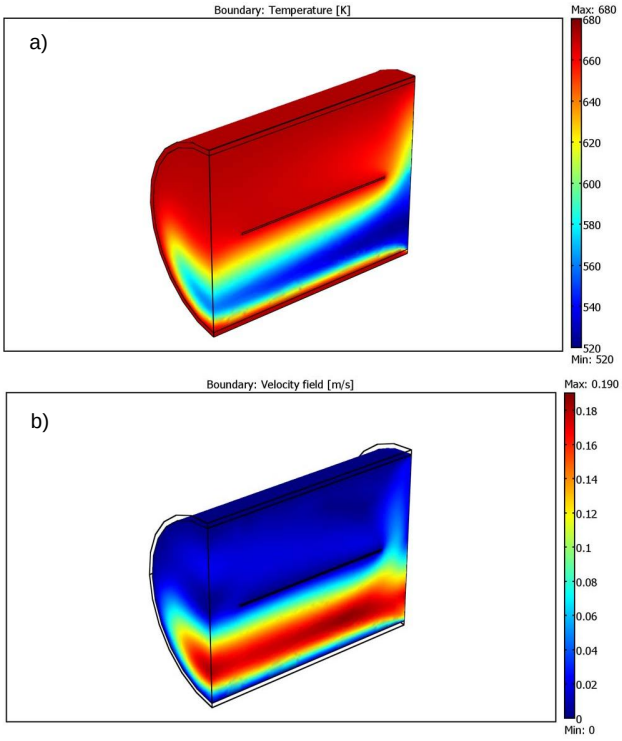

Figure 6. Temperature (a) and velocity (b) fields near the wafer for high nitrogen flow and ε=1. Gas moves from right to left.

 ISBN: 978-1-61208-380-3

temperature, nitrogen flow and wafer emissivity ε. Cross sections of the temperature fields in the centre of the furnace for ε=1 and ε=0 are given in Fig. 7a and Fig. 7b, respectively. Temperature of the heat absorbing sample (ε=1) is 35 ºC higher than temperature of the reflective sample (ε=0). As a consequence, the temperature distribution in the upper volume is more uniform for ε=1.

IV. DISCUSSION

Annealing of thin silver films is complicated by three circumstances. Firstly, silver films and nanostructures are melted at low temperature [3, 9, 10]. In our previous study [5], it was shown that this melting point is close to 250 ºC. However, this transformation happens only once and the second heating of the sample does not change morphology of silver nanostructures. Secondly, liquid silver tends to spherical shape of nanoislands due to low cohesive forces to SiO_2 surface. Thirdly, silver is the best plasmonic material [6] and silver nanostructures appeared after breaking apart continuous film modify optical properties of the sample surface [7].

The first sign of not identical annealing conditions in the studied furnaces is different sample colours (Fig. 2) and

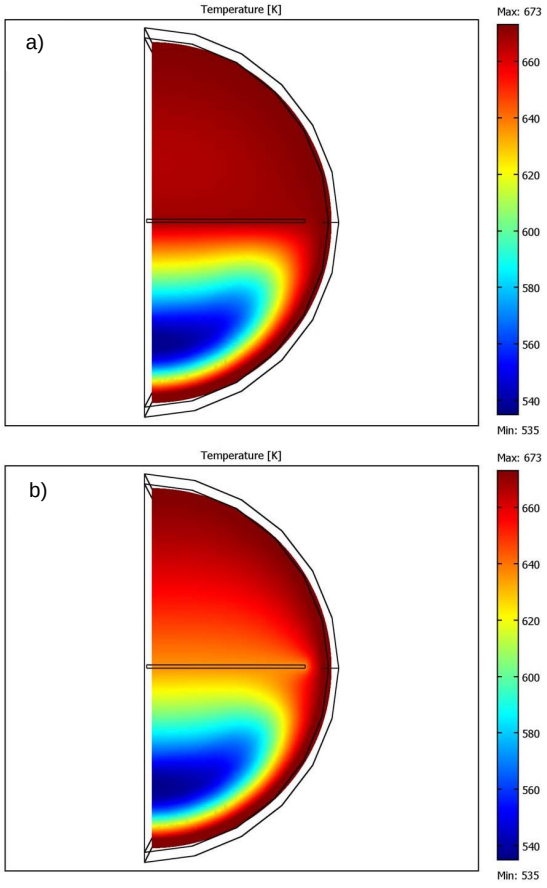

Figure 7. Vertical cross sections of the temperature fields at high nitroghen flow in the centre of the furnace for ε=1 (a)and ε=0 (b).

corresponding changing of reflection spectra after annealing (Fig. 4). Reflection spectra demonstrate strong plasmon properties of silver nanostructures formed after silver film annealing. The troughs in the range 690 – 810 nm correspond to dipole plasmon resonance and peaks at 410 – 500 nm correspond to quadrupole resonance [7]. The non-annealed sample possesses only very weak dipolar plasmon resonance (see spectrum of as-deposited sample). Till some extent plasmon properties can be estimated by the difference between calculated and measured spectra – the larger difference, the stronger plasmon resonances. Based on this criterion, the strongest plasmon resonances are observed in the sample #3. Plasmon properties are very sensitive to asymmetry of dielectric environment. In the studied samples, refractive index of silicon (n=3.5) is much higher than refractive index of SiO_2 (n=1.5). Due to this local electric field is concentrated in silicon and optical properties of silver are modified. It is illustrated by reflection of *p*-polarized light (Fig. 4b), which mainly excites electric field at silver/substrate interface. For *p*-polarization deviations of real spectra from calculated ones are much larger than for *s*-polarized light.

In Section III, we have shown that that all annealed samples have close values of silver areal density and nanostructure sizes. Therefore, relatively large redshift of peaks and troughs in Fig. 4 cannot be only explained by changing of island geometry. Due to identity of the studied samples, the spectrum variations can be only connected with material modification, e.g., changing of silver dielectric function. Moreover, from spectral peak and trough broadening (the broadest peak has sample #2) follows that imaginary part of silver dielectric function increased [6].

Usually, annealing is used to improve and restore crystalline structure. However, there are reports about increased defect concentration in melted silver samples [11]. Our RHEED observations also showed that crystalline structure of the annealed sample #2 is worse than structure of the as-deposited one. Taking into account the broadest reflection peak and absence of dipolar trough for sample #2 we can conclude that this sample has highest disorder of crystalline structure among the studied samples.

In the diffusion furnace (Fig. 1a) the target temperature 400 ºC was supported on the external side of the quartz tube. In the fast ramping furnace (Fig. 1b) the target temperature 400 ºC was supported inside of furnace, 1 cm above bottom of the quartz tube. According to Fig. 6a the measured temperature in this point can be 150 ºC lower than the tube temperature, i.e., in our experiment the tube temperature of the fast ramping furnace could be close to 550 ºC. Nitrogen flow 8.3×10^{-5} standard m^3/s is very low for the fast ramping furnace (Fig. 1b) and provides laminar gas flow inside tube. In case of diffusion furnace (Fig. 1a), the same nitrogen flow is too high and provides turbulent gas flow in the lower part of the tube (Fig. 5a). Higher temperature of the absorber shield (ε~1) around the quartz tube makes thermal radiation in the fast ramping furnace much higher than in the diffusion one.

In case of thin silver layer on silicon, most of radiation energy is absorbed in silver and during heating up in laminar

 ISBN: 978-1-61208-380-3

gas flow (the fast ramping furnace) the silver temperature is higher than the temperature of the substrate. In turbulent gas flow, intensive heat exchange between silver and nitrogen prevents overheating of silver nanostructures (the diffusion furnace).

After melting silver starts to form droplets due to surface tension forces and decreases silver areal density. However, absorbed thermal radiation is proportional to silver areal density or absorbing cross-section. Thus, geometry change decreases radiative heat transfer to silver. The cold substrate cools down silver nanostructures and causes their rapid solidification. The quenching happens without proper crystallization and silver solidifies in amorphous phase (sample #2).

In case of low radiative heat transfer (samples #1, #3), melting happens at higher substrate temperature and without silver overheating. Depending on conductive and radiative heat fluxes the melted silver is cooled with much lower rate and solidifies in polycrystalline phase. In our study, sample #3 has the best crystalline structure due to lower cooling rate between two hot plates in vacuum. One of the reasons for quenching in this case is reduction of the surface energy [12]. Another reason is heating of silver nanostructures by conductive flux through interfacial thermal resistance. Silver melting acquires additional heat flux from the substrate to the nanostructure. This heat flux increases temperature drop on the interfacial thermal resistance between the substrate and the silver droplet, what in turn leads to decreasing of silver temperature and quenching.

V. CONCLUSIONS

We have demonstrated that annealing of identical samples in identical conditions, but in different furnaces leads to different results. The effect of furnace operational parameters (gas flow, sample and thermocouple position, sample emissivity) on annealing of thin silver films has been analyzed. Radiation heating of silver films can be very strong and provides overheating of the silver relatively substrate. However, silver areal density is shrunk after melting and droplet formation what causes decrease of radiation heating. As a result, melted structures are quenched to solid state with irregular shape and high crystalline disorder. The effect depends on rate of solidification and explains variation of annealing results from furnace to furnace.

ACKNOWLEDGMENT

This research was undertaken at the Micronova Nanofabrication Centre of Aalto University.

REFERENCES

[1] S. Franssila, “Introduction to Microfabrication”, 2nd edition, Wiley, 2010, 534p.

[2] V. Ovchinnikov, A. Malinin, S. Novikov, and C. Tuovinen, ” Silicon Nanopillars Formed by Reactive Ion Etching Using a Self-Organized Gold Mask”, Physica Scripta, vol.T79, 1999, pp.263-265.

[3] S. R. Bhattacharyya et al., “Growth and Melting of Silicon Supported Silver Nanocluster Films”, J. Phys. D: Appl. Phys., vol. 42, 2009, pp. 035306-1 - 035306-9.

[4] D. Adams, T. L. Alford, and J. W. Mayer, “Silver Metallization: Stability and Reliability”, Springer, 2008, 123p.

[5] V. Ovchinnikov, “Effect of Thermal Radiation during Annealing on Self-organization of Thin Silver Films”, Proceedings of ICQNM 2013, ThinkMind Digital Library (ISBN: 978-1-61208-303-2), pp. 1-6.

[6] M. A. Garcia, “Surface Plasmons in Metallic Nanoparticles: Fundamentals and Applications”, J. Phys. D: Appl. Phys., vol. 44, 2011, pp. 283001-1 - 283001-20.

[7] V. Ovchinnikov and A. Shevchenko, “Self-Organization-Based Fabrication of Stable Noble-Metal Nanostructures on Large-Area Dielectric Substrates”, Journal of Chemistry, vol. 2013, 2013, Article ID 158431, pp. 1 - 10., http://dx.doi.org/10.1155/2013/158431.

[8] A. Ichimiya and P. I. Cohen, “Reflection High-Energy Electron Diffraction”, Cambridge University Press, 2004, 353p.

[9] O. A. Yeshchenko, I. M. Dmitruk, A. A. Alexeenko, and A. V. Kotko, “Surface Plasmon as a Probe for Melting of Silver Nanoparticles”, Nanotechnology, vol. 21, 2010, pp. 045203-1 - 045203-6.

[10] M. Khan, S. Kumar, M. Ahamed, S. Alrokayan, and M. Salhi, “Structural and Thermal Studies of Silver Nanoparticles and Electrical Transport Study of Their Thin Films”, Nanoscale Research Letters, vol. 6, 2011, pp. 434-1 - 434-8.

[11] S. A. Little, T. Begou, R. E. Collins, and S. Marsillac, “Optical Detection of Melting Point Depression for Silver Nanoparticles via in situ Real Time Spectroscopic Ellipsometry”, Appl. Phys. Lett., vol. 100, 2012, pp. 051107-1 -1 051107-4.

[12] E. P. Kitsyuk, D. G. Gromov, E. N. Redichev, and I. V. Sagunova, “Specifics of LowTemperature Melting and Disintegration into Drops of Silver Thin Films”, Protection of Metals and Physical Chemistry of Surfaces, vol. 48, 2012, pp. 304–309.

 ISBN: 978-1-61208-380-3

Arc Discharge Synthesis and Properties of Magnetic Nanoparticles

Sergey A. Novopasin, Marina A. Serebrjakova, Alexey V. Zaikovskii
Lab. of Rarefied Gases
Kutateladze Institute of Thermophysics
Novosibirsk, Russia
e-mail: sanov@itp.nsc.ru

Lubov G. Smolyaninova,
Sobolev Institute of Geology and Mineralogy
Novosibirsk, Russia
Tatiana U. Kardash
Boreskov Institute of Catalysis
Novosibirsk, Russia

***Abstract*—The composite Fe-C anode sputtering in a low pressure arc discharge has been used to produce Fe containing nanoparticles on a carbon matrix. The manufactured material was calcined stepwise in air from 300 to 1100 K. This procedure resulted in the formation of Fe oxides and oxidation of carbon and converting it into gas phase. The results show the change in morphology, chemical composition, crystalline phases and magnetic susceptibility properties with annealing temperature. This research is directed to elaborate on new technologies for producing magnetic nanoparticles and ferrofluids from their basis.**

Keywords – magnetic nanoparticles; arc dicharge; ferrofluids.

I. INTRODUCTION

The magnetic iron oxide nanoparticles are mainly used in ferrofluid technologies. Many chemical techniques are used to synthesize iron oxide nanoparticles for ferrofluids, including coprecipitation, hydrothermal reactions [1], sol–gel method [2], micro emulsions techniques [3], flow injection synthesis [4], aerosol/vapor methods, sonochemical reactions [5], electro spray synthesis [6], and electrochemical synthesis [7]. Nevertheless, the method mainly used for the generation of magnetite nanoparticles is chemical coprecipitation technique of iron salts [8] - [10]. Magnetic nanoparticles could not be kept as a powder because of their small size and strong interaction. Therefore, all the above mentioned technologies use surfactants to prevent agglomeration of magnetic nanoparticles directly in base fluids. In this paper, we present a new technology for manufacturing magnetic nanoparticles inside the carbon matrix, which allows the transportation of magnetic nanoparticles as a powder.

The details of experimental setup and used probing techniques are presented in section "Experimental Development". Section "Experimental Results" is devoted to the results obtained by Transmission Electron Microscopy (TEM), X-ray Diffraction (XRD), Thermo gravimetric analysis (TGA), Raman scattering (RS) and magnetic susceptibility measurements. It is underlined in conclusion section that the arc discharge technology is perspective for ferrofluid applications.

II. EXPERIMENTAL DEVELOPMENT

The experiments were carried out in a direct current electric arc, which had a current of 120 A, in the buffer gas (helium) at 25 Torr. The spray electrode (anode) was a graphite rod 70 mm in length and 7 mm in diameter. A hole (with the diameter of 4 mm) was drilled in the center of the electrode to be filled with graphite – carbonyl iron mixture powder. Fe/C weight ratio was 2/1. Monatomic spray products were diffused in the buffer gas from the hot zone of the arc, which resulted in cooling and heterogeneous condensation of the spray products. The composite material was precipitated on a cooled shield located at 5 cm from the arc discharge area. The synthesized material consist of iron containing nanoparticles on a carbon matrix. For the second step, the synthesized Fe-C composite was calcined for two hours in air at 200, 300, 400, 450, 500, 550, 600, 700 and 800 °C. This procedure resulted in the formation of Fe oxides and oxidation of carbon and removing it into the gas phase. TEM, XRD, TGA, RS and magnetic susceptibility measurements were used to test material properties at every step.

High-resolution TEM images were obtained using the JEM-2010 electron microscope (JEOL, Japan) with lattice-fringe resolution of 0.14 nm and accelerating voltage of 200 kV. The high-resolution images of periodic structures were analyzed by the Fourier method. Local energy-dispersive X-ray analysis (EDXA) was carried out using the EDX spectrometer (EDAX Co.), which was fitted with a Si (Li) detector, at (!!!) resolution of 130 eV. The samples for the HRTEM study were prepared on a perforated carbon film mounted on a copper grid.

XRD analysis was carried out using the Bruker D8Advance diffractometer, which was equipped with the Lynxeye (1D) linear detector, over the angular range of 10–75◦ at 2Θ = 0.05◦ with the storage time of 1 s for each point. Monochromatic CuK-radiation (1.5418˚A) was applied in these experiments.

TGA experiments were performed by the DTG60 H instrument (Shimadzu Scientific Instruments).

The Raman spectra were taken on the Spex Triplemate instrument (Princeton Instruments, USA) at the wavelength of 488 nm.

Magnetic susceptibility was measured by MS2 susceptibility/temperature system (Bartington, Great Britain).

III. EXPERIMENTAL RESULTS

A. Morphology of material

Electron microscopy of the synthesized material indicated that it consist of amorphous carbon particles with inclusions of crystal nanoparticles of 2–10 nm (see Figure 1). Calcinations in air resulted in carbon removal g, oxidation of

 ISBN: 978-1-61208-380-3

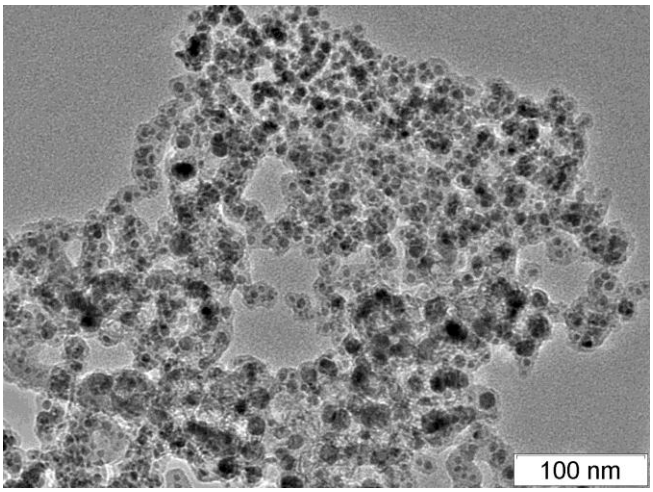

Figure 1. The morphology of synthesized material.

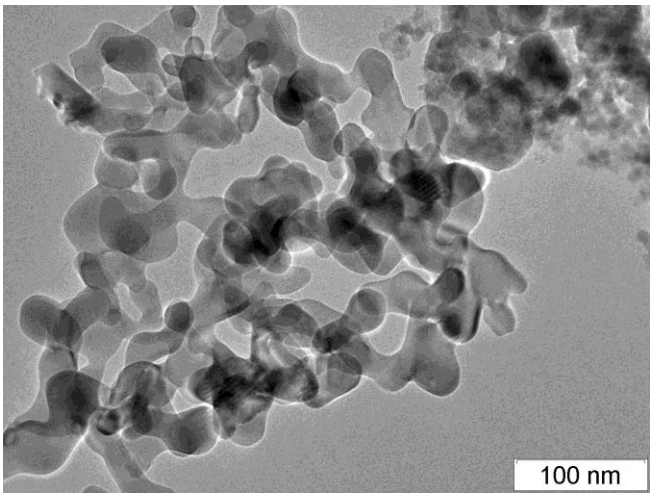

Figure 2. The morphology of the material calcined at 400 °C.

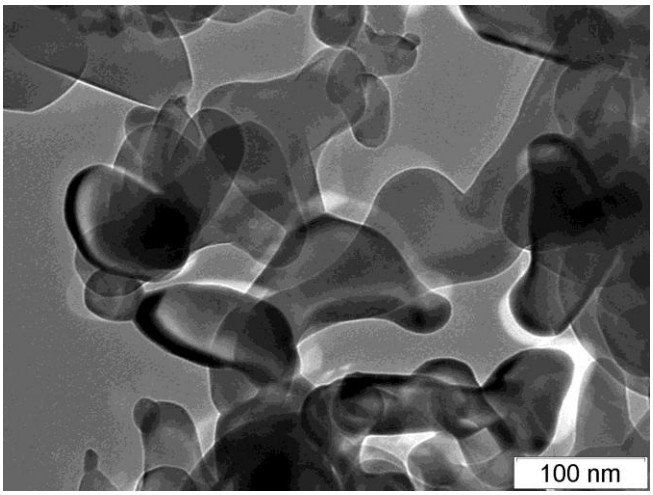

Figure 3. The morphology of the material calcined at 800 °C.

iron and junction of nanoparticles (see Figures 2, 3). The morphology was transformed from separate nanoparticles into the 3-D random connected structures with expending size and the temperature of calcinations increasing.

B. Thermogravimetric analysis

Thermogravimetric analysis of synthesized materials has been carried out in two ways. Firstly, is the use of DTG60 device, and secondly, is the step-wise calcinating at definite temperature for two hours and measuring the weight loss. Data are presented in Figure 4.

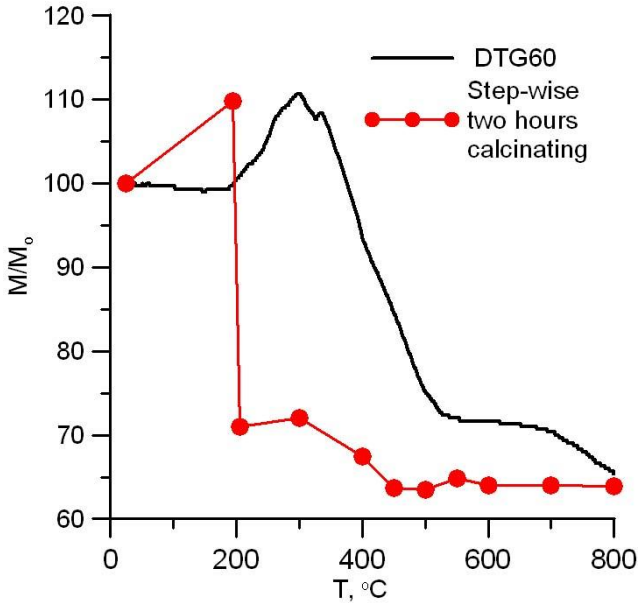

Figure 4. Thermogravimetric analysis.

Both curves show the weight increase at the initial stage. Obviously, it is due to oxidation of iron containing particles. The step-wise analysis demonstrates that at 200 °C, most part of carbon reacts with oxygen (Fe nanoparticles probably served as catalyst) and it is removes from the sample. The reason for the observed difference is the fact that the reaction times in both cases differed considerably.

C. Phase composition

X-ray diffraction spectroscopy shows that the synthesized material consists of graphite, iron and iron carbide (see Figure 5). Calcination of this material results in a change in composition. Even when calcinating at 300 °C, both α-Fe_2O_3 and γ-Fe_2O_3 crystalline forms of iron oxide appeared, but iron and iron carbide lines disappeared in the spectrum (see Figure 6).

X-ray diffraction spectroscopy shows that the synthesized material consists of graphite, iron and iron carbide (see Figure 5). Calcination of this material results in

 ISBN: 978-1-61208-380-3

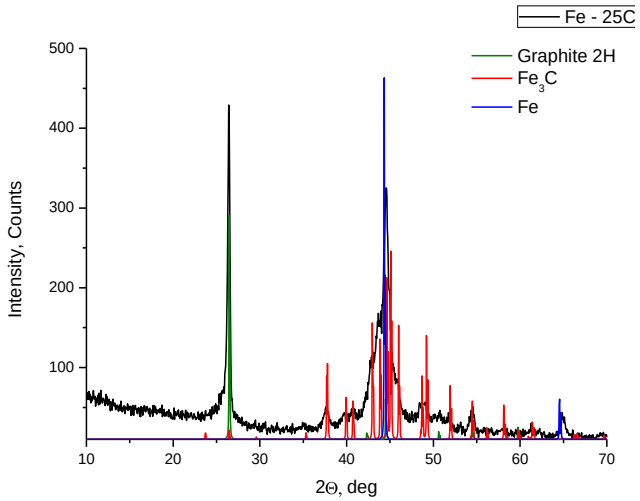

Figure 5. XRD spectrum of synthesized material.

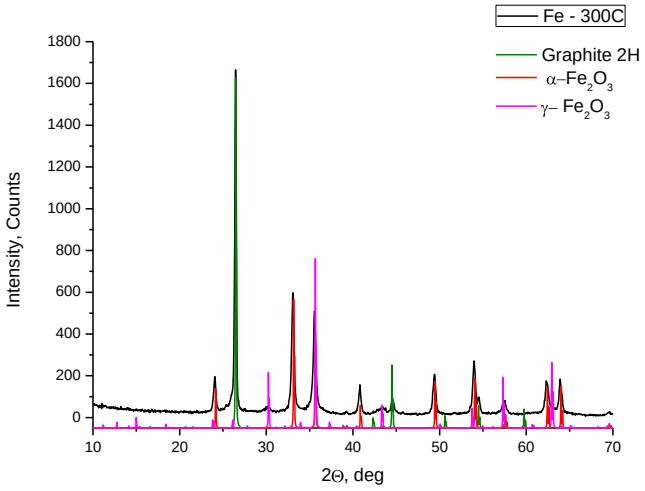

Figure 6. The XRD spectrum of material calcinated at 300 °C.

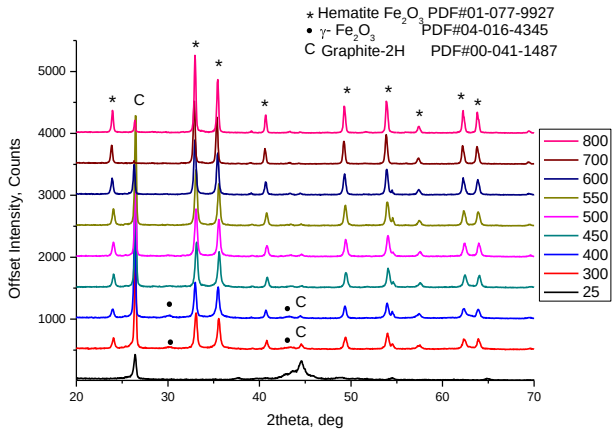

Figure 7. The XRD spectra of material calcinated at different temperatures..

change in composition. Even when calcinating at 300 °C, both α-Fe_2O_3 and γ-Fe_2O_3 crystalline forms of iron oxide appeared, but iron and iron carbide lines disappeared in the spectrum (see Figure 6).

Further calcinations resulted in γ-Fe_2O_3 disappearing and growing intensity of α-Fe_2O_3 (non-magnetic) as shown in Figure 7. It is interesting to note that graphite line does not disappear even at 800 °C.

D. Raman spectroscopy

Raman spectra of materials calcinated at different temperatures are shown in Figure 8. Practically, no signals of iron oxides are seen up to the calcination temperature of 300 °C. The main lines are: 225, 299, 400, 500, and 613 cm^{-1}. Most lines identify α-Fe_2O_3, but line 500 cm^{-1} is the sum of γ-Fe_2O_3 (strong intensity) and α-Fe_2O_3 (week intensity) [11]. Data obtained by RS confirm XRD data, but we suppose that for our materials, XRD analysis is preferable for identification of phase composition with respect to Raman scattering.

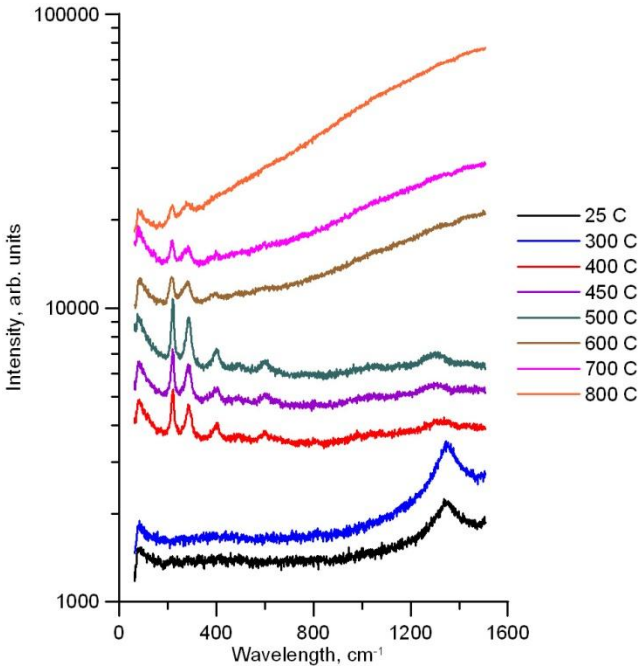

Figure 8. Raman spectrum of material calcinated at different temperatures.

E. Magnetic susceptibility

To measure magnetic susceptibility, about 200 mg of synthesized material was loaded into the measuring dish. The temperature dependency was measured by heating the sample and then cooling it in air. Results are shown in Figure 9. Heating in air resulted in chemical reaction with oxygen and phase transition as it was noted before. So, the final weight of the sample was about 135 mg in accordance with TGA measurements (see Figure 4). The same reason is that magnetic susceptibility was close to zero, while cooling.

 ISBN: 978-1-61208-380-3

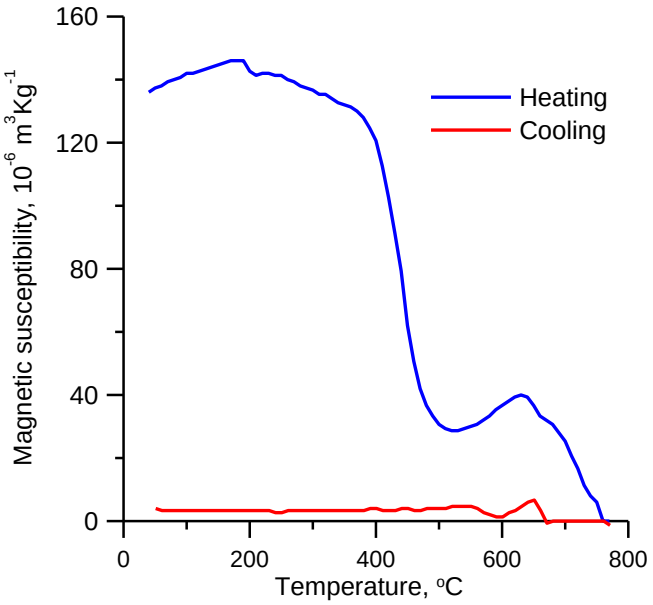

Figure 9. Magnetic susceptibility vs. temperature.

IV. CONCLUSIONS

The arc discharge technology of manufacturing magnetic nanoparticles has been suggested and realized. The morphology, phase composition and magnetic susceptibility have been measured at calcination in air of up to 800 °C. We consider the synthesized material perspective for ferrofluid applications.

The future research of this work is directed to optimization of the arc discharge parameters to reach the maximal value of magnetic susceptibility.

ACKNOWLEDGMENT

This research was funded by Russian Ministry of Education and Science. Project Identifier: RFMEFI60414X0004.

REFERENCES

[1] J. Wan, et al., "A soft-template-assisted hydrothermal approach to single crystal Fe3O4 nanorods", J. Cryst. Growth, vol. 276, no. 3, 2005, pp. 571–576.

[2] C. Albornoz and S. E. Jacobo, "Preparation of a biocompatible magnetic film from an aqueous ferrofluid", J.Magn.Magn.Mater. vol. 305, no.1, 2006, pp. 12–15.

[3] A. B. Chin and I. I. Yaacob, "Synthesis and characterization of magnetic iron oxide nanoparticles via w/o microemulsion and Massart's procedure", J.Mater. Process.Technol., vol. 191, no. 1, 2007, pp. 235–237.

[4] G. Salazar-Alvarez, M.Muhammed, and A. A. Zagorodni, "Novel flow injection synthesis of iron oxide nanoparticles with narrow size distribution", Chem. Eng. Sci., vol. 61, no. 14, 2006, pp. 4625–4633.

[5] E. H. Kim, Y. Ahn, and H. S. Lee, "Biomedical applications of super paramagnetic iron oxide nanoparticles encapsulated within chitosan", J. Alloys Compd., vol. 434, 2007, pp. 633–636.

[6] S. Basak, D.-R. Chen, and P. Biswas, "Electro spray of ionic precursor solutions to synthesize iron oxide nanoparticles: modified scaling law", Chem. Eng. Sci., vol. 62, no. 4, 2007, pp. 1263–1268.

[7] D. Ramimoghadam, S. Bagheri, and S. Bee Abd Hamid, "Progress in electrochemical synthesis of magnetic iron oxide nanoparticles", Journal of Magnetism and Magnetic Materials, vol. 368, 2014, pp. 207–229.

[8] S. A. Morrison, et al., "Magnetic and structural properties of nickel zinc ferrite nanoparticles synthesized at room temperature", J.Appl.Phys., vol. 95, no. 11, 2004, pp. 6392–6395.

[9] J. Qiu, et al., "Preparation and characterization of porous ultrafine Fe_2O_3 particles", Mater.Res.Bull., vol. 40, no. 11, 2005, pp. 1968–1975.

[10] S.-J. Lee, et al., "Magnetic enhancement of iron oxide nanoparticles encapsulated with poly(D,L-latide-co-glycolide)", Colloids Surf.,A, vol. 255, no. 1, 2005, pp. 19–25.

[11] D. L. A. de Faria, S. Venancio Silva, and M. T. de Oliveira, "Raman microspectroscopy of some iron oxides and oxyhydroxides", J. Raman Spectrosc. vol. 28, 1997, pp. 873–878.

 ISBN: 978-1-61208-380-3